

L.H. van Utenhove

Characterisation of a functionally
graded duplex stainless steel
fabricated by Gas Tungsten Arc Welding

Characterisation of a functionally graded
duplex stainless steel
fabricated by Gas Tungsten Arc welding

By

L.H. van Utenhove

in partial fulfilment of the requirements for the degree of

Master of Science

in Material Science and Engineering

at the Delft University of Technology,
to be defended publicly on Thursday August 30, 2019 at 09:30 AM.

| | | |
|-------------------|-------------------------|----------|
| Supervisor: | Dr. ir. M.J.M. Hermans, | TU Delft |
| Thesis committee: | Dr. C. Goulas, | TU Delft |
| | Dr. C. Ayas, | TU Delft |

An electronic version of this thesis is available at <http://repository.tudelft.nl/>.

Acknowledgements

I want to acknowledge the kindness and guidance of some of the people around me. This thesis would not be what it is, without your support.

Marcel, thank you for the topic, your quick way of acting, your guidance and patience.
Thank you Constantinos for bringing new ways to look at the subject.

I would like to thank Juriaan and Frans for the support in all welding quests. Thank you Remko, for all the hours spend in the lab with me. Thank you Hans for the performing of the heat treatments. Richard and Ruud from XRD and XRF. Thank you Aravind for the implemented heat model

My general support system (Friends): Geerte, Sven, Malwine, Maxine, Vivi, Ursa and Mirte. You made my day, repeatedly.

Thank you to my mother, father and sister, for believing in me.

And lastly, thank you Hubert, for always being at my side.

*L.H. van Utenhove
Delft, August 2019*

Contents

| | | |
|--------|--|----|
| 1. | Introduction | 11 |
| 1.1. | Motivation..... | 11 |
| 1.2. | Research Question..... | 11 |
| 1.3. | Report Structure..... | 11 |
| 2. | Theoretical Background and Literature Review | 13 |
| 2.1. | Introduction | 13 |
| 2.2. | Additive Manufacturing..... | 13 |
| 2.3. | Microstructure Evolution | 15 |
| 2.3.1. | Principles of Solidification | 15 |
| 2.3.2. | Solidification in Single Pass Welds | 15 |
| 2.3.3. | Constitutional Supercooling | 17 |
| 2.3.4. | Formation of secondary phases in stainless steel | 18 |
| 2.3.5. | Phase formation in single pass stainless steel welds | 20 |
| 2.4. | Solidification mechanisms in duplex steel welds..... | 22 |
| 2.5. | Phase fractions in duplex steel welds | 23 |
| 2.6. | Microstructure morphology in Additive Manufacturing..... | 26 |
| 2.7. | Functionally Graded Materials | 26 |
| 2.7.1. | Phase graded materials | 27 |
| 2.7.2. | Chemically graded materials..... | 28 |
| 2.7.3. | Production techniques of chemically graded materials..... | 28 |
| 2.7.4. | Functionally graded stainless steels..... | 29 |
| 2.7.5. | Formation of secondary phases in Functionally Graded Materials | 30 |
| 3. | Materials and Methods | 31 |
| 3.1. | Introduction | 31 |
| 3.2. | Materials..... | 31 |
| 3.3. | Welding arrangements | 31 |
| 3.4. | Welding specifications | 33 |
| 3.5. | Temperature measurements | 34 |
| 3.6. | Preliminary welding experiments | 35 |
| 3.7. | Parameter per experiment..... | 35 |
| 3.7.1. | Experiment A: 316L stainless steel | 35 |
| 3.7.2. | Experiment B: 316L & AISI 430L in equal portion | 35 |
| 3.7.3. | Experiment C: 316L & AISI 430L functionally graded..... | 35 |
| 3.7.4. | Heat treatment..... | 36 |
| 3.8. | Characterisation of the microstructure | 36 |
| 3.8.1. | Sample preparation..... | 36 |
| 3.8.2. | Optical Microscopy..... | 37 |
| 3.8.3. | Scanning electron microscopy | 37 |
| 3.8.4. | X-ray Fluorescence..... | 38 |
| 3.8.5. | X-ray diffraction..... | 38 |
| 3.8.6. | COMSOL heat modelling for estimation of cooling rates | 39 |
| 4. | Results | 41 |
| 4.1. | Introduction | 41 |

| | | |
|--------|--|----|
| 4.2. | Preliminary Results | 41 |
| 4.2.1. | Single Bead deposits | 41 |
| 4.2.2. | Multi-pass welds | 43 |
| 4.2.3. | Warping of the plates | 44 |
| 4.3. | Experiment A..... | 44 |
| 4.3.1. | Appearance and dimension | 45 |
| 4.3.2. | Temperature | 45 |
| 4.3.3. | Chemical composition and Phases | 46 |
| 4.3.4. | Macrostructure and Microstructure..... | 46 |
| 4.4. | Experiment B..... | 48 |
| 4.4.1. | Appearance and dimension | 48 |
| 4.4.2. | Chemical composition and Phases | 48 |
| 4.4.3. | Macrostructure and Microstructure..... | 50 |
| 4.5. | Experiment C | 52 |
| 4.5.1. | Appearance and dimension | 52 |
| 4.5.2. | Temperature | 52 |
| 4.5.3. | Chemical composition and Phases | 54 |
| 4.5.4. | Macrostructure and Microstructure..... | 55 |
| 4.6. | Heat treatments..... | 57 |
| 5. | Discussion..... | 59 |
| 5.1. | Introduction | 59 |
| 5.2. | Experimental Setup and Welding Parameters | 59 |
| 5.2.1. | Effect of the wire feeder calibration error..... | 59 |
| 5.2.2. | Homogeneity of the layer height..... | 59 |
| 5.2.3. | Inaccuracies of the wire feed holders | 60 |
| 5.2.4. | Decreasing building time..... | 61 |
| 5.2.5. | Summary: Experimental Arrangements and Welding Parameters..... | 61 |
| 5.3. | Thermal cycling | 61 |
| 5.3.1. | COMSOL heat model..... | 61 |
| 5.3.2. | Cooling rate | 62 |
| 5.3.3. | Summary: thermal cycling..... | 63 |
| 5.4. | Phase morphology | 64 |
| 5.4.1. | Experiment A | 64 |
| 5.4.2. | Experiment B | 65 |
| 5.4.3. | Experiment C..... | 66 |
| 5.5. | Reducing the interpass time – COMSOL simulation | 70 |
| 5.6. | Formation of brittle phases in the as-welded material | 71 |
| 5.6.1. | Microstructure | 71 |
| 5.7. | Summary: Heat treatments | 71 |
| 6. | Conclusion | 73 |
| 7. | Recommendations | 73 |
| | Bibliography | 75 |

Abstract

Functionally graded materials (FGM) are a class of materials in which the chemical composition or microstructure varies as a function of position, offering unique material properties. In this study, a functionally graded structure was manufactured using Gas Tungsten Arc Welding and a double wire feed device. The wire feed rate was changed step by step of the austenitic AISI 316L and ferritic AISI 430L stainless steel wire, creating a chemically graded duplex stainless steel structure. The structure, approximately 30 mm in height, was investigated using Optical Microscopy, X-Ray Diffraction, X-Ray Fluorescence and Energy Dispersive X-Ray Spectroscopy. The transverse section is composed of large elongated grains. The chemical analysis revealed a relatively smooth change in Nickel and Molybdenum composition over the section, due to remelting of previously deposited layers. The graded material showed a gradual transition in phase fractions from mainly austenite and some ferrite to mainly ferrite and some austenite, to fully ferric structure. There were no brittle phases detected in the structure.

1. Introduction

1.1. Motivation

It has been increasingly popular to provide commercially tailored product solutions. To answer this demand, different layer-by-layer deposition methods are developed. Additive manufacturing or '3D printing' of metals allows for local control of the product properties such as mechanical and corrosion performance of the material. Similarly, additive manufacturing is used to print chemically graded structures, or structures that change their chemical composition across the bulk volume of the material. This allows for the development of materials with unique combinations of mechanical, thermal or chemical properties. In this study, such a Functionally Graded Material (FGM) is fabricated using Gas Tungsten Arc Welding (GTAW).

Gas Tungsten Arc welding is an arc welding method in which a tungsten electrode near a base material forms an electric circuit, heating the base metal locally. The electric arc generates enough heat to melt the base metal and to deposit metal wire on the base metal, however it does not melt the tungsten electrode. In this study, two dissimilar metals were molten simultaneously, creating a (liquid) mixture of both materials. When the heat source moves away, the mixture solidifies. Repeating this process layer by layer, eventually forms a solid structure, with a chemical composition which is a mixture of wire 1 and 2 and the base material.

In this study, two common grades of stainless steel were used, an austenitic and a ferritic stainless steel. Austenite and ferrite are two phases that occur in the Fe-C phase diagram. When mixing these grades, a duplex morphology of both phases is formed. This study investigates the change in chemical composition and phase morphology for a ferritic-austenitic stainless steel FGM. Functionally Graded Materials using stainless steel were previously investigated by Hofmann *et al.* [1]. They investigated multiple graded structures one of which was an AISI 316L to Invar 316 chemically graded structure. Zhang *et al.* [2] created a duplex stainless steel chemically graded structure. Both papers used lasers as an heat source to fabricate the graded structures, and both papers report changes in phase composition/morphology and smooth chemical gradients.

1.2. Research Question

This study is centred around the following question:

- What are the phases, phase morphology and chemical developments in a functionally graded stainless steels using Gas Tungsten Arc Welding?

1.3. Report Structure

The investigation and fabrication of a functionally graded duplex steel is documented in this report.

The second chapter is a combination of background knowledge and a literature review. The first part explored the solidification behaviour in welded structures as well as the different phases and phase morphologies and room- and solidification temperature for stainless steels. The chapter further investigates the change in the observed microstructure due to remelting and the formation of secondary phases. At the beginning and end of the chapter, a literature review on additive manufacturing and FGM's is provided.

Chapter three is a description of the experimental methods and the materials used in this study. To fabricate the graded structure, a parametrical analysis was performed and an experimental setup had to be devised in which two wires were fed at the same rate in the weld pool. These preliminary experiments, which are introduced in this chapter, were used to validate a system in which a graded structure could be fabricated. In this study, three different structures are investigated: a structure using only austenitic stainless steel (Experiment A), a second structure in which both wires are mixed in equal ratio (Experiment B) and the Functionally Graded Structure (Experiment C). In Chapter 4 an overview of the results of Experiment A-C is given. The first section of the chapter briefly discusses the parametrical analysis or 'preliminary experiments'. The results from this section was used to set up Experiment A-C. The chapter then continues to the analysis of the overall structure, microstructure, (local) chemical composition, phase composition of Experiments A-C. Chapter five discusses the experiments, building time and temperature measurements. A COMSOL heat model is used to estimate cooling rate, peak temperatures and change in interpass temperature when changing interpass time. The discussion then turns to the solidification microstructure of the different builds and the formation of secondary phases. The conclusion and recommendations follow in chapter 6 and 7.

2. Theoretical Background and Literature Review

2.1. Introduction

This chapter starts with an overview of additive manufacturing techniques, with a focus on methods for large scale printing of 3D metallic components, in particular Gas Tungsten Arc Welding with additional wire feeding. After this general introduction of the technique, detailed information on the theoretical background on solidification of melt pools and the microstructural evolution upon further cooling is provided. The formation of intermetallic compounds and carbides will be addressed. In wire arc additive manufacturing the same metallurgical principles as in welding can be applied, although boundary conditions may change when creating a 3D product instead of a single weld deposit. Finally, the topic of functionally and compositionally graded materials is introduced with specific emphasis on stainless steels.

2.2. Additive Manufacturing

Additive Manufacturing (AM) is the collective name for layer-by-layer building processes. This production method allows for complex, customized parts to be built [3]. Figure 1 gives a schematic overview of additive manufacturing techniques. The various additive manufacturing processes for metallic components make use of different heat sources and feedstock resulting in specific processing times and deposition rates. The figure makes a distinction between three types of direct energy deposition (DED) making use of a laser (a), an electron beam (b) or an electric arc (c) as a heat source. For some deposition techniques powders are used (a) and (d), while in binder jet a combination of powder and binder fluid is applied. Other techniques use wire (c) or metal tape [e]. In this study, the adopted production technique is wire and arc additive manufacturing (WAAM) with a gas tungsten arc (GTA) as a heat source.

Metal additive manufacturing opens new possibilities for new products and the controlled production of new alloys. As an example, Shen i.e. [4] investigated the fabrication of vertical aluminium-steel structures, using WAAM. He reported that the structure mainly consisted of the intermetallic Fe_3Al and that its overall morphology was made of large columnar grains. Szost i.e. [5] investigated the mechanical properties and deformation of the building process by laser cladding process (CLAD) and wire arc additive manufacturing (WAAM). Microstructure and residual stress evolution of both additive manufacturing processes were investigated. They concluded that significant grain coarsening and a larger HAZ are observed in the WAAM structure and that the CLAD sample is composed of narrow wavy columnar grains. The residual stresses in the base plate were larger for WAAM. Both techniques created specimens that were fully dense with very few pores.

As this investigation explores the possibilities offered by Wire Arc Additive Manufacturing, the remainder of this section is focussing on the WAAM technique. In Wire Arc Additive Manufacturing the heat source is an electric arc and the solid wire is used as consumable. An electric arc is created between a workpiece and an electrode will locally melt the workpiece and the metal wire fed. The welding process used can either be Gas Metal Arc Welding (GMAW) or Gas Tungsten Arc Welding (GTAW). In GMAW a continuous fed consumable electrode wire is used, whereas in GTAW a non-consumable tungsten electrode is applied, and a consumable wire is fed separately. Both processes have a relatively high deposition rate, compared to powder-based methods. The deposition rate is

one of the advantages compared to powder methods [3], and allows to produce large scale structures.

In this investigation GTAW is selected as deposition technique. A schematic of the process is depicted in Figure 1c. As mentioned, an arc is struck between the tungsten electrode and the workpiece. The generated heat locally melts the workpiece. A consumable wire is melted when it enters the arc region. In the melt pool mixing of the materials supplied will occur by weld pool flow. The molten region and the tungsten electrode are protected from oxidation by an inert shielding gas. Typical values for arc voltage are in the range of 10-15 V and the welding current ranges from 50-200 A depending on selected arc length and electrode diameter. The power generated is the product of arc voltage (U) and welding current (I). The heat introduced in the workpiece per unit length can be defined by

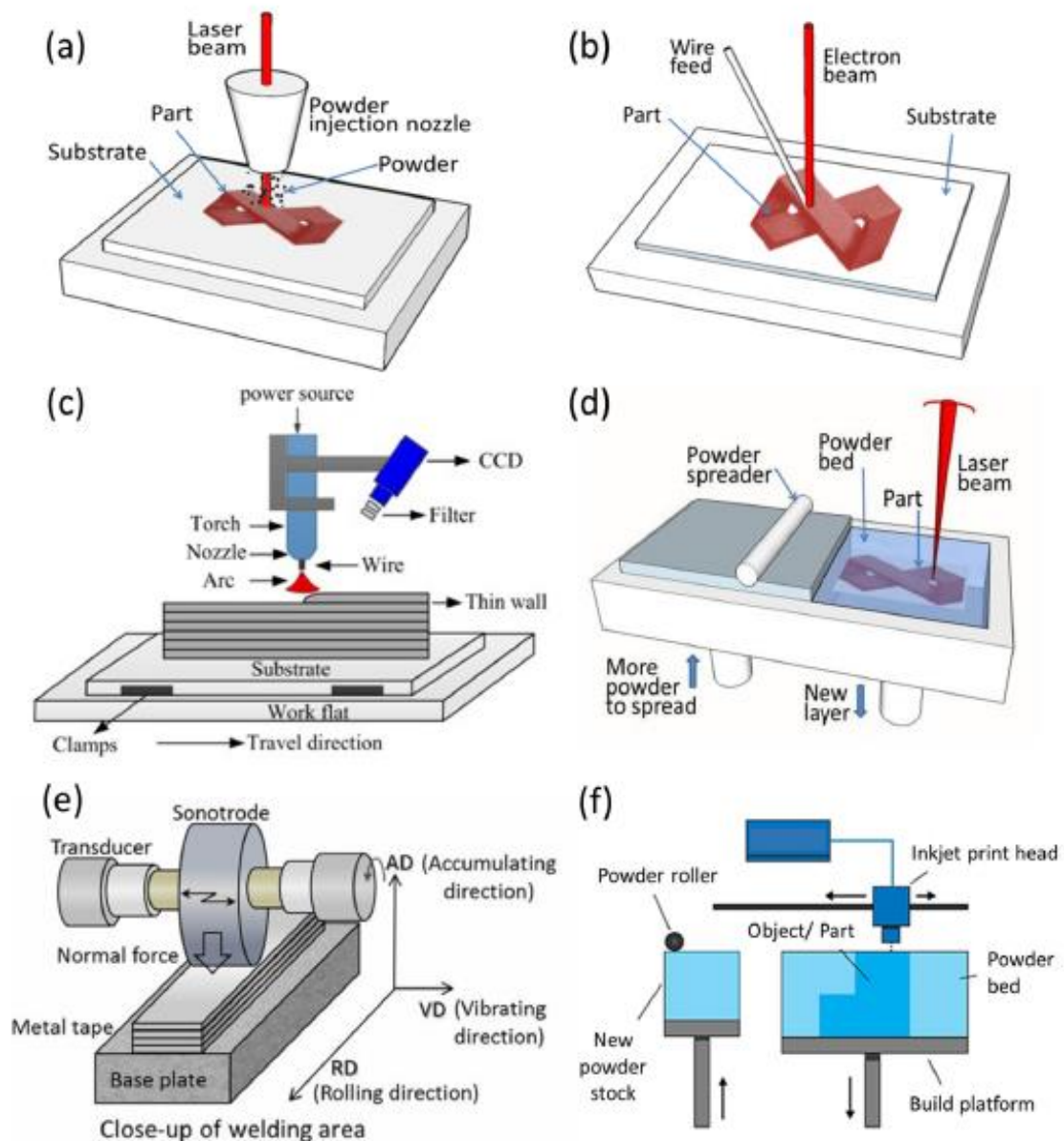


Figure 1: Schematic diagram overview of additive manufacturing methods (a) DED-L (b) DED-EB (c) DED-A (d) PBF-L (e) ultrasonic additive manufacturing (UAM) process and (f) binder jet [3]

$$HI = \eta \frac{UI}{v} \quad (2.1)$$

With η the process efficiency (0.6-0.9) [6] and v the travel speed.

The introduction of the heat causes melting and superheating of the liquid metal. When the heat source has passed the liquid will cool and solidify. When the peak temperature is reached then the cooling rate depend on the material properties of the material to be welded/deposited (specific heat, density, heat conductivity) and the boundary conditions (dimensions of the work piece, heat transfer coefficients). Apart from the molten region, the adjacent material will also be affected by the heat introduced, i.e. the heat affected zone (HAZ). The entire thermal cycle determines the microstructural evolution of the material considered. This will be discussed in the next section in detail.

2.3. Microstructure Evolution

In this section the microstructure evolution for welds and welded 3D structures will be discussed. First the principles of solidification for welds in general are discussed. Then, the solidification in a single pass weld will be discussed. For alloyed metals, constitutional supercooling and the formation of secondary phases dictates the microstructure, they are discussed next. Finally, the topic of solidification in stainless steel is discussed.

2.3.1. Principles of Solidification

The observed microstructure of a weld at room temperature is the product of the chemical composition of the metal and the thermal cycle imposed to the material. In the following description the solidification of steel weldments is considered, however the principles are also applicable for other metals/alloys. In additive manufacturing the building process requires the deposition of multiple layers resembling multi-pass welding. The thermal cycling involved will obviously affect the development of the microstructure. This will be discussed later.

2.3.2. Solidification in Single Pass Welds

The heat source creates a liquid pool. The dimensions depend on the welding parameters and the thermal properties of the material. When the heat source has passed a certain location, cooling will take place. At the fusion boundary heterogeneous nucleation will occur, the grains at the fusion line act as nuclei and grow in the direction of the maximum temperature gradient (perpendicular to the fusion line). In addition, certain crystallographic orientations are easy growth directions (*i.e.* the $\{100\}$ directions for cubic structures such as fcc/bcc metals) [7]. The shape of the weld pool (elliptical or teardrop shape) dictates whether during the solidification process competitive growth takes place, see Figure 4. Preferable grains (easy grow direction parallel to the maximum temperature gradient) will outgrow less favourable oriented grains, see Figure 3. Furthermore, the solidification front velocity varies with the location and is minimal when solidification just starts and reaches a maximum value equal to the travel speed of the welding process at the centreline as indicated in Figure 2 (right).

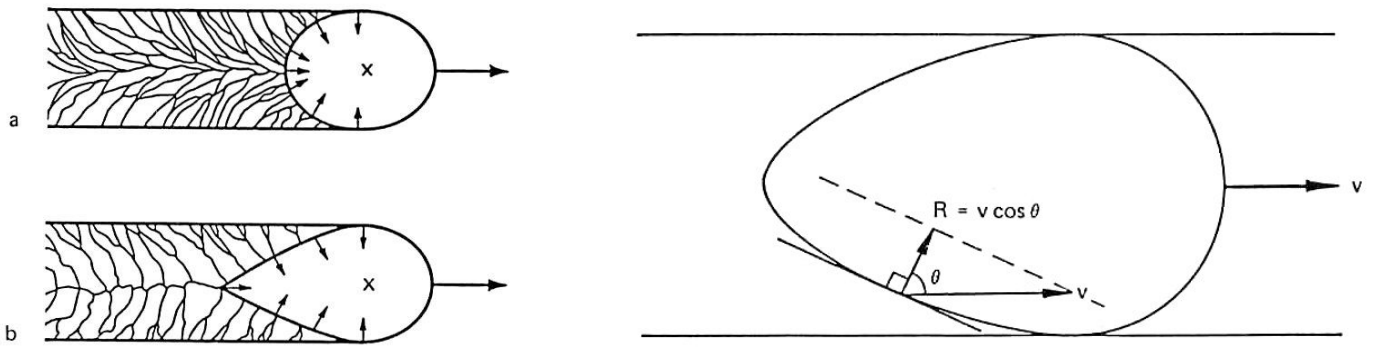


Figure 4: (left) Macrostructure of solidification related to weld pool shape (top view) [35] (right) Macrostructure of solidification related to weld pool shape [6]

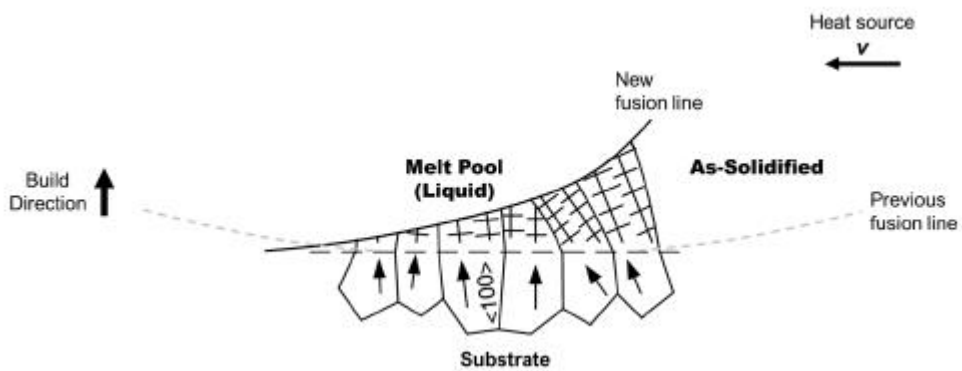


Figure 3: Schematic illustration of competitive epitaxial grain growth in the melt pool during solidification as the heat source moves away. The arrows in the grains of the substrate indicate the easy growth direction (*i.e.*, $\langle 100 \rangle$ in fcc and bcc metals [7])

2.3.3. Constitutional Supercooling

During solidification segregation may occur. The extend of segregation is dependent on the solubility of alloying elements in the solidifying material. This results in a compositional gradient ahead of the solidification front if the weld pool flow is not too severe. Due to this gradient the liquidus temperature will vary in this region. If the actual temperature at the fusion line is higher than the liquidus temperature the solidification front is planar. A solid protrusion will remelt, see Figure 5a. When the actual temperature is lower than the liquidus temperature an area of constitutional supercooling can be defined, see Figure 5b. Any protrusion at the solidus/liquidus interface will grow. Depending on the severeness of supercooling multiple substructures can be observed ranging from cellular dendritic to equiaxed dendritic as shown in Figure 7.

The resulting of solidification front morphology, as shown in Figure 7, can also be described in terms of temperature gradient G and interface growth rate R . Here the temperature gradient G is defined as

$$(2.2) \quad G = |\nabla T|$$

and the interface growth rate or solidification rate velocity is can be expressed as [7]

$$(2.3) \quad R = (1/G)(\partial T/\partial t)$$

Thus the G/R determines the solidification mode [6], while the product GR determines the size of the solidification structure.

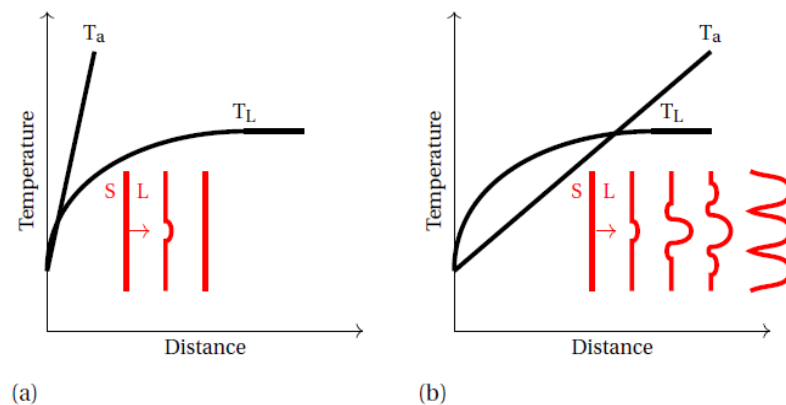


Figure 5: Schematic illustration showing (a) stability of planar interface and (b) breakdown of the planar interface; Here $T(a)$ is the actual temperature and $T(L)$ is the liquidus temperature gradient. When the liquidus temperature is lower than the actual temperature, the planar solidification front breaks up in the protrusion [35].

As mentioned before, the substructure development in welds is also dependent on the solubility of alloying elements. In Figure 6, the substructure development in welding for low alloyed steel and high alloyed steel is depicted. For high alloyed steel, the segregation of alloying elements is more severe due to the higher concentration of alloying elements in the steel, thus increasing formation of dendrites.

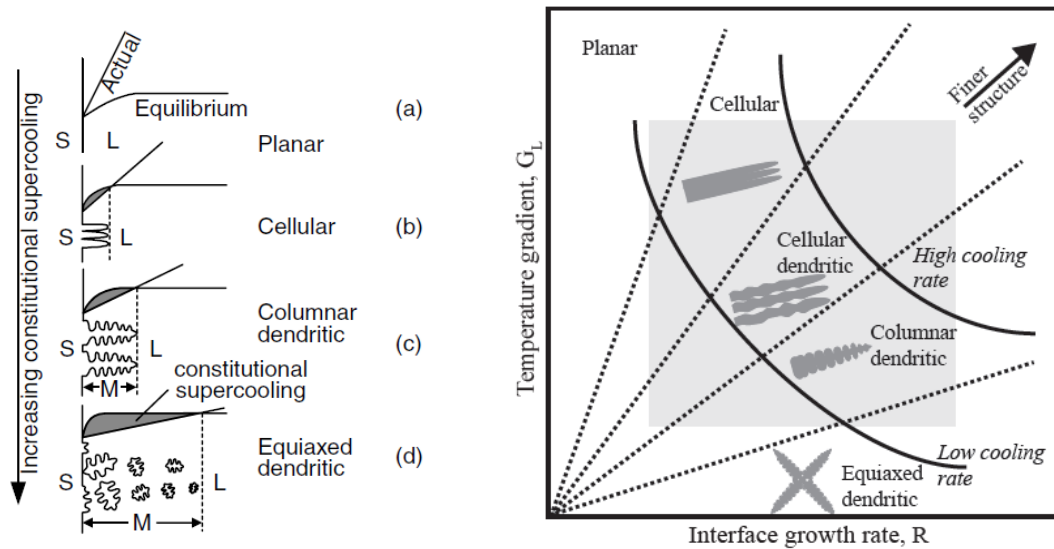


Figure 7: When the constitutional supercooling (M) is increased, cellular protrusions will develop to dendritic structures [6]; (right) Schematic showing the interface morphology changes with temperature gradient and interface growth rate. The shaded region shows typical weld microstructural morphology [36].

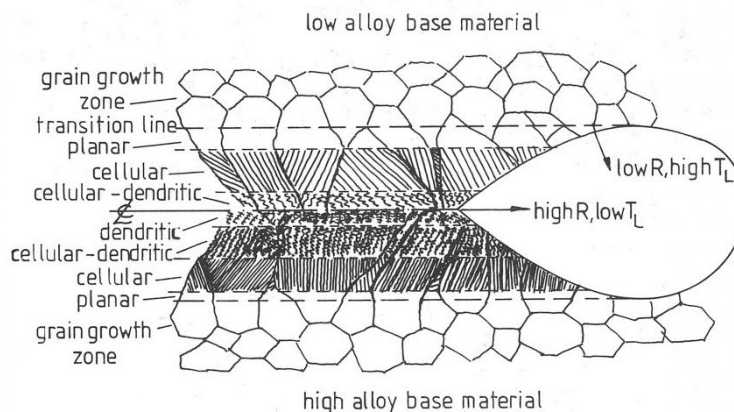


Figure 6: Substructure development in welding for low alloyed steel (top) and high alloyed steel (bottom) [36].

2.3.4. Formation of secondary phases in stainless steel

In Figure 8 the phase diagram for a commercially available stainless steel is given. From the diagram, it can be taken that under equilibrium conditions and at lower temperatures carbides and secondary phases form. Investigations in the formation secondary phases have been made, as these are often brittle and may lead to crack formation [8].

Allahyari *et al.* [9] investigated the formation of these low temperature equilibrium phases. They heat treated welded AISI 316L stainless steel for 1-100 hours at 500-700°C. In this temperature range, they reported the formation of $M_{23}C_6$ carbides. Furthermore, the authors reported small variations of the ductility due to the formation of the carbides. However, when aging at temperature between 750 and 850°C the tensile ductility and impact toughness were strongly affected. The authors investigated the brittle samples and found spheroid particles formed from the delta-ferrite, which they found to be enriched in Fe, Cr and Mo. From this, the authors conclude these particles to be the brittle intermetallic sigma phase.

The formation of sigma phase in AISI316 is a frequently mentioned topic of concern, as mentioned in by the authors, the presence of sigma phase, decreased the impact thoroughness and the ductility of the material. Therefore, the formation mechanisms, critical temperature and crystal structure of sigma phase is discussed in the next section.

Sigma phase

The sigma phase is an intermetallic phase with a tetragonal crystal structure (Figure 11). The sigma phase is indicated in the iron-chromium phase diagram in the composition range of 43 to 59 wt. % Cr, see Figure 8. It is also found in AISI 316L stainless steel pseudo-binary phase diagram in the composition range of 3 to 40 wt. % Ni. Sigma phase formation is often observed in (duplex) stainless steels, with a high chromium content.

Cristini i.e. [10] used electrochemical methods to detect sigma phase in 22% Cr duplex stainless steel. Their samples were solution annealed and water quenched prior to aging. Heat treatments were performed between 600-1000°C and water quenched. Using microscopy and image analysing software, they found that in the temperature range of 750-950°C precipitation of secondary phases occurs. The authors emphasise that the brittle phase was mainly found at ferrite grain boundaries and that its morphology change as a function of temperature. They report that sigma phase was formed first inside the ferrite phase and ferrite/ferrite or ferrite/austenite phase boundaries. Or, in other words, they found the sigma phase formed everywhere except in the austenite grain. They further report that by using XRD, distinctive peaks of sigma phase (950°C, 850°C, 750°C) and carbides (only 850°C and 750°C) were found. Furthermore, it was found that at 850°C a relatively high precipitation of sigma phase was found, compared to the 750°C and 950°C heat treatments.

The formation of sigma phase in the ferrite and at the ferrite/austenite phase boundary is also mentioned by Hsieh and Wu [11] and the evolution formation of the phase is depicted in Figure 10. Ferrite in austenite, as i.e. in duplex steel, is a nucleation site for sigma phase. The sigma phase can also precipitate from γ -austenite when there is no δ -ferrite in the stainless steels, however this as unlikely to occur.

Hsieh and Wu [11] summarised the main findings on the brittle intermetallic sigma phase. They compared different compositions in which this phase may occur: Fe-Cr, Fe-Mo, and

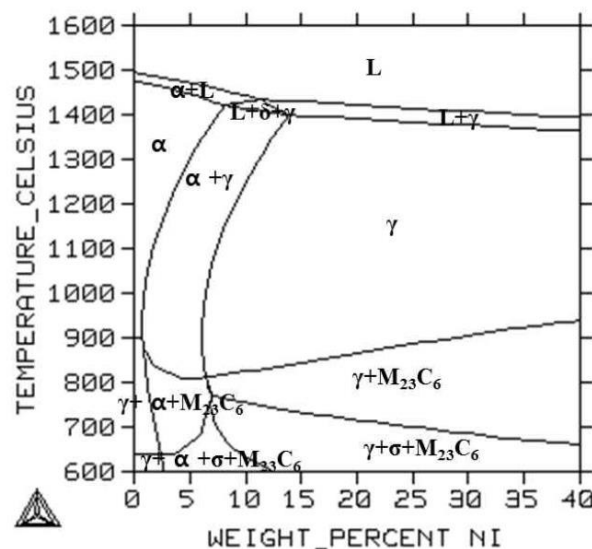


Figure 8: Phase diagram of commercial 316L stainless steel, plotted by using ThermoCalc, at lower temperatures carbides and intermetallic phases may form [37]

(FeNi)_x(CrMo)_y and reported precipitation rates and fractions at different temperatures for different steel compositions. They mention that sigma phase, which is observed in various series of stainless steels, has detrimental effects on the properties of the steel, for example on the mechanical properties (lower ductility), corrosion resistance and weldability. They emphasise that when Cr content of the stainless steel is higher than a certain level (above 20 wt.%) the precipitation of sigma phase is difficult to prevent. And the addition of strong ferrite stabilisers (Cr, Si, or Mo) further increase the risk for sigma phase formation.

2.3.5. Phase formation in single pass stainless steel welds

In this study, the material used was two types of stainless steel: a ferritic AISI 430 and an austenitic AISI 316 stainless steel. When mixing these grades, a duplex morphology of both phases is received. In order to later identify the morphology, the following sections will describe the observed solidification microstructures and phase transformations for the stainless steel alloys.

Stainless steels are Fe-C-M_x alloys with a relatively high percentage of chromium and containing other alloying elements such as nickel, molybdenum and silicon [12]. Stainless steel is relatively resistant to corrosion based on the formation of a chromium-oxide layer. Alloying elements affects the crystal structure. Some elements are associated with the stabilisation of ferrite (bcc lattice), while others form more readily austenite (fcc lattice). Silicon, chromium, molybdenum and vanadium are ferrite stabilisers, while austenite stabilising elements are nickel, carbon and manganese [13]. In Table 1 the chemical composition of the most common ferritic and austenitic stainless steel is listed.

Table 1: The chemical composition in wt.% of the most common ferritic and austenitic stainless steel

| Elements | C | Si | Mn | P | S | Cr | Mo | Ni | Fe |
|-----------------|------|------|------|-------|------|-------|-----|-------|---------|
| AISI 316 | 0.08 | 0.75 | 2.00 | 0.045 | 0.03 | 16-18 | 2-3 | 10-14 | balance |
| AISI 430 | 0.12 | 1.00 | 1.00 | 0.04 | 0.03 | 16-18 | - | - | balance |

Phase diagrams

Based on the composition equilibrium phase diagrams can be obtained. These diagrams indicate the solidification behaviour of alloys, which is different for the ferritic and austenitic stainless steels. It should be mentioned that alloying elements affect the position of the phase fields shown in the following binary diagrams.

Ferritic stainless steel

The binary Fe-Cr phase diagram, Figure 11, shows that when the liquidus is passed a bcc ferrite phase will form. For chromium contents below approximately 13 wt.%, the ferrite will transform to austenite and a reversed solid state transformation will occur at temperatures between 800 and 900°C. Above 13 wt.% Cr added to iron austenite will not be formed and the ferrite is stabilised. At temperature below 830°C sigma phase may form, which was discussed in the previous section.

Austenitic stainless steel

If iron is alloyed with nickel the material will solidify as austenitic (fcc), except for Ni contents below approximately 8 wt.%, see Figure 9. In that case in first instance δ ferrite (bcc) is formed. The austenite remains stable up to low temperatures. The kinetics of the solid state transformations at these low temperatures is low.

Martensitic stainless steel

Some stainless steels can be hardened, which involves a non-equilibrium phase transformation from austenite to martensite (bct). This may occur for instance in Fe-Cr alloys

with chromium contents below 13 wt.%. For this transformation the factor time (*i.e.* cooling rate) plays an important role and Time Temperature Transformation (TTT) and Continuous Cooling Transformation (CCT) diagrams are more appropriate.

Duplex stainless steel

Duplex stainless steels are austenitic-ferritic stainless steels with roughly equal phase fractions.

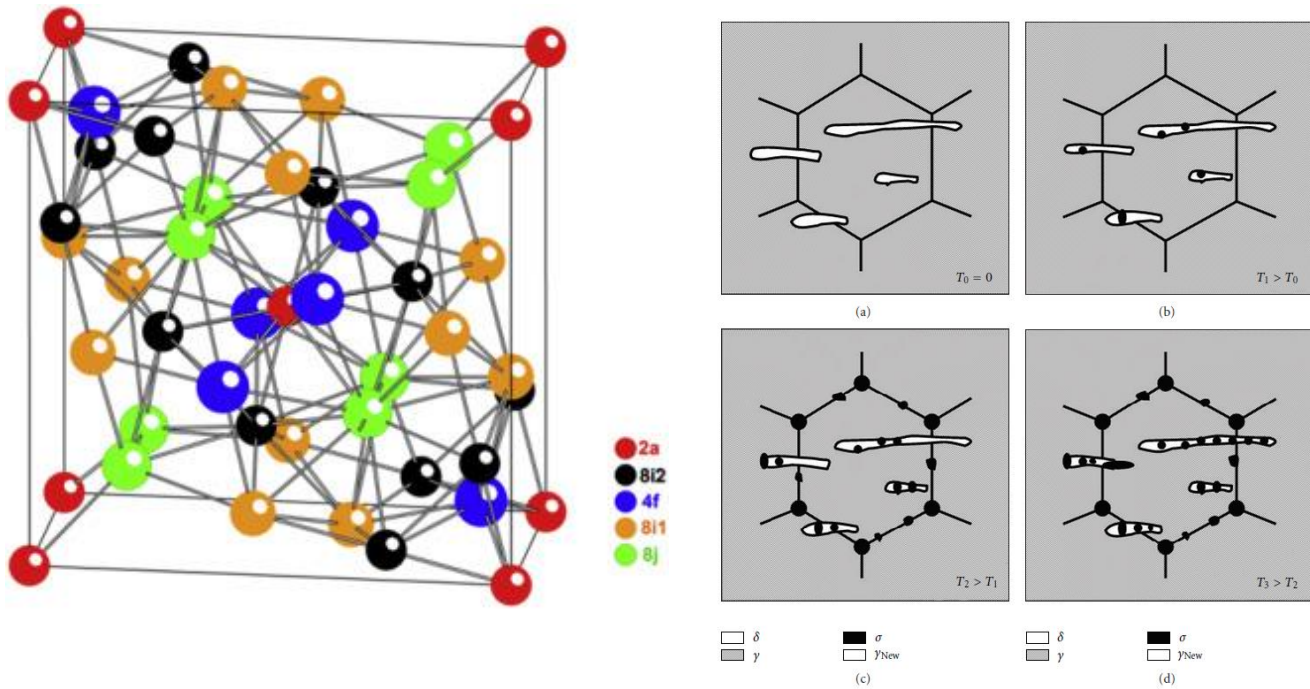


Figure 10: (left) the tetragonal crystal structure of the sigma phase [38] (right) Precipitation mechanism of sigma in AISI 316L stainless steel [11]

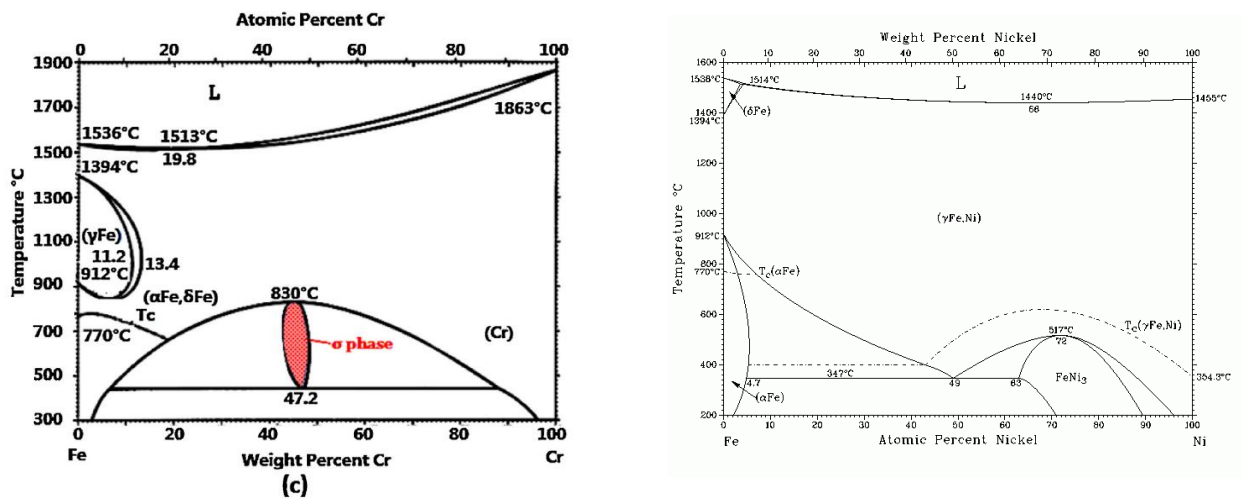


Figure 11: (left) Fe-Cr binary phase diagram with the sigma phase [12] (right) Fe-Ni phase diagram [39]

2.4. Solidification mechanisms in duplex steel welds

In Figure 12 the elevated temperature region of the pseudo-binary phase diagram is depicted. From the phase diagram it can be taken that when the composition of the duplex is changed from an austenitic stainless steel to a ferritic stainless steel, the stable phase at high temperature also changes from an austenite to ferrite, with high temperature phase transformation occurring from the primary phase. The primary formed phase is also called the leading phase [12]. The region where austenite and ferrite are formed shortly after each other, form distinct morphologies in duplex welds, which have been theorised by Suutala i.e. [14], [15]. This theory was later generalised to four solidification modes. Type A, AF, FA, F.

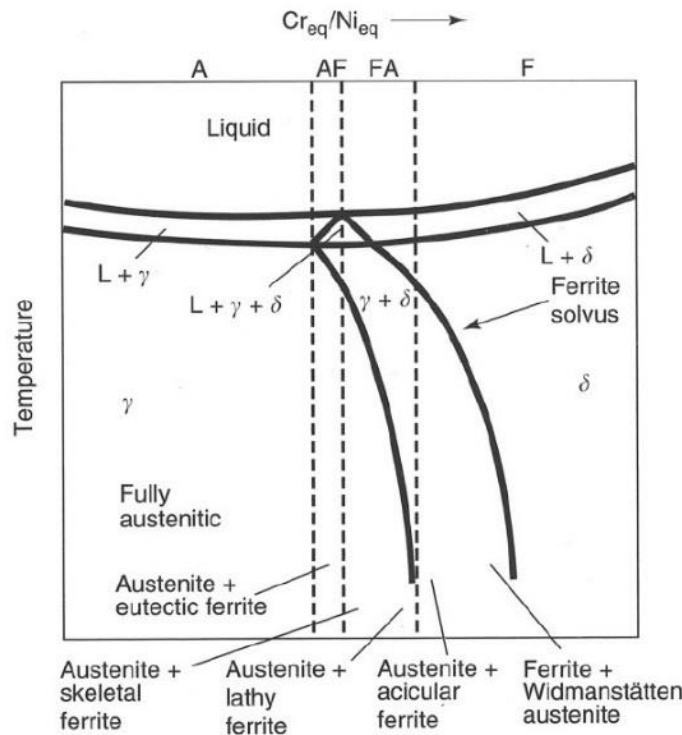


Figure 12: Elevated temperature region of a pseudo-binary phase diagram for duplex stainless steel compositions [12].

Table 2: Solidification Types, Reactions, and Resultant Microstructures [12]

| Solidification Type | Reaction | Microstructure |
|---------------------|---|--|
| A | $L \rightarrow L + A \rightarrow A$ | Fully austenitic, well-defined solidification structure |
| AF | $L \rightarrow L + A \rightarrow L + A + (A + F)_{eut} \rightarrow A + F_{eut}$ | Ferrite at cell and dendrite boundaries |
| FA | $L \rightarrow L + F \rightarrow L + F + (F + A)_{per/eut} \rightarrow F + A$ | Skeletal and/or lathy ferrite resulting from ferrite-to-austenite transformation |
| F | $L \rightarrow L + F \rightarrow F \rightarrow F + A$ | Acicular ferrite or ferrite matrix with grain boundary austenite and Widmanstätten side plates |

Type A: austenite forms at high temperature and no further high temperature phase transformation takes place. Type AF: austenite is the leading phase and delta ferrite solidifies from the rest of the melt. Type FA: delta ferrite is the leading phase, austenite solidifies from the rest of the melt and a quick ferrite to austenite phase transformation takes

place, but a higher volume fraction of ferrite at room temperature is present and Type F: the weld metal solidifies completely to delta ferrite and austenite forms through a solid state transformation. These types are also identified in the phase diagram (Figure 12).

These different solidification and transformation modes for austenite and ferrite are visible in the received microstructure of the weld at room temperature. A lathy structure of the ferrite points towards a ferrite to austenite phase transformation, while e.g. vermicular ferrite implies austenite to have been the leading phase in the cellular/dendritic solidification and ferrite to be the rejected solute. An overview of the resultant microstructures and the solidification type can be found in Table 2.

2.5. Phase fractions in duplex steel welds

In the previous century, computational models have been constructed and experimental studies were carried out to determine the resulting phase-composition at room temperature. These models can be applied for different production processes, such as casting and welding. Figure 13 presents a schematic TTT diagram of steel and the effect of alloying elements on the phase fields. Some elements promote solid state phase transformations, whereas others are delaying the transformation. CCT diagrams look similar, but a cooling rate is induced, whereas for the TTT diagrams the temperature is instantaneously lowered to the temperature of interest and then maintained. The difference between the two concepts is the rate of undercooling and the driving force for transformation, i.e. the change in Gibbs free energy. The start and finish time of a certain transformation can then be obtained [16].

To be able to predict the phase present at room temperature for a wide range of chemical compositions in steel under cooling conditions prevailing during welding, diagrams were constructed that indicate the presence of certain phases based on the amount of ferrite stabilising elements (represented by a Cr-equivalent) and the amount of austenite forming elements (represented by a Ni-equivalent). Schaeffler, De Long and diagram [17] and Welding Research Council (WRC) diagrams [18] were constructed (Figure 15, Figure 14). In each of these approaches the weighing factor of the elements and the elements considered in the calculation of the Ni and Cr-equivalent are different. In the de Long and WRC diagrams focus on the austenite-ferrite region, i.e. higher chromium and nickel equivalents [12]. The diagrams deliver the austenite, ferrite and martensite fractions in the material.

$$Ni(eq) = Ni + 30 \times C + 0.5 \times Mn \quad (2.4)$$

$$Cr(eq) = Cr + Mo + 1.5 \times Si + 0.5 \times Nb \quad (2.5)$$

The phase ratio based on the Ni and Cr-equivalents for the steels considered in this study, see Table 1 and Table 3, can be found using the Schaeffler diagram. In these cases, the predicted phase for AISI 316 stainless steel is austenite and for AISI 430 is a mixture of ferrite and martensite.

Table 3: Schaeffler (1949) Nickel and Chromium equivalents of AISI 316 and 430 stainless steel

| Schaeffler | Nickel equivalent | Chromium equivalent |
|-----------------|-------------------|---------------------|
| AISI 316 | 13.15 | 19.83 |
| AISI 430 | 4.10 | 18.5 |

However, it should be considered that these diagrams only provide an indication what major phases can be expected when welding a material. Morphology of the phase or the presence of precipitates and intermetallic compounds are not specifically mentioned.

More recent studies were performed on AISI 430 and AISI 316 address the complex morphologies of the primary phases predicted by the Schaeffler diagram. Ramkumar *i.e.* [19] show that using autogenous TIG welding on AISI 430 ferritic steel, a primary ferritic-martensitic microstructure is received. Closer microstructure studies depicted the presence of two-phase structure containing ferrite-intergranular martensite and a precipitate-free zone surrounding the grain boundary martensite at the fusion zone of all the weldments.

In some cases, unfavourable phases were also found in the weld metal. Weiss and Stickler [20] performed a study on AISI 316 stainless steel being exposed to high temperature (heat-treatments). They found nucleation and growth of carbides ($M_{23}C_6$, M_6C) and intermetallic phases (sigma, chi, eta). These phases are in general brittle and are problematic for the use of this alloy in steam generating power plants and nuclear reactors. Therefore, a close study of the microstructure is needed, to evaluate the phases formed due to the weld thermal cycle and the service temperature. In the case of additive manufacturing when chemically grading the material, certain compositions might become more sensitive to form those phases especially due to the multiple thermal cycling during production.

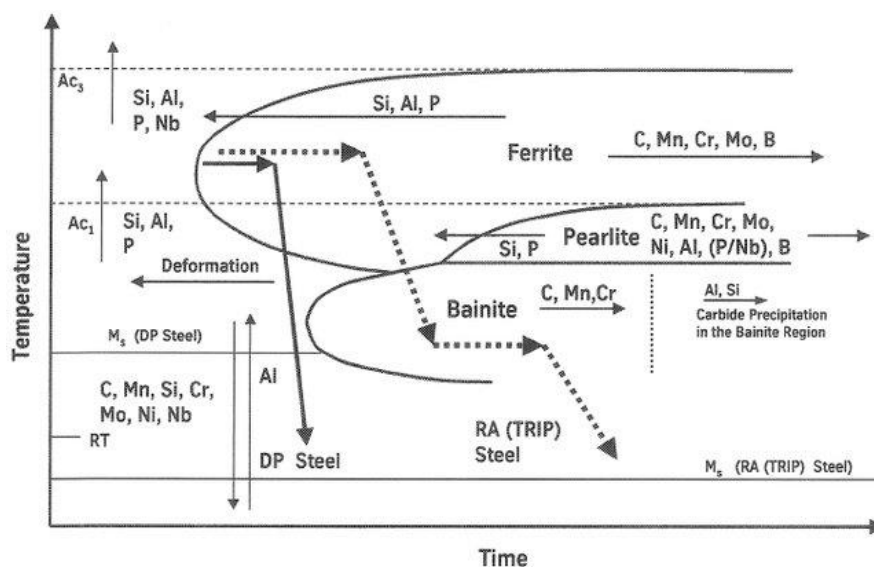


Figure 13: Time Temperature Transformation diagram for multi-phase steel, showing the influence of different alloying elements and the influence of the cooling rate [40].

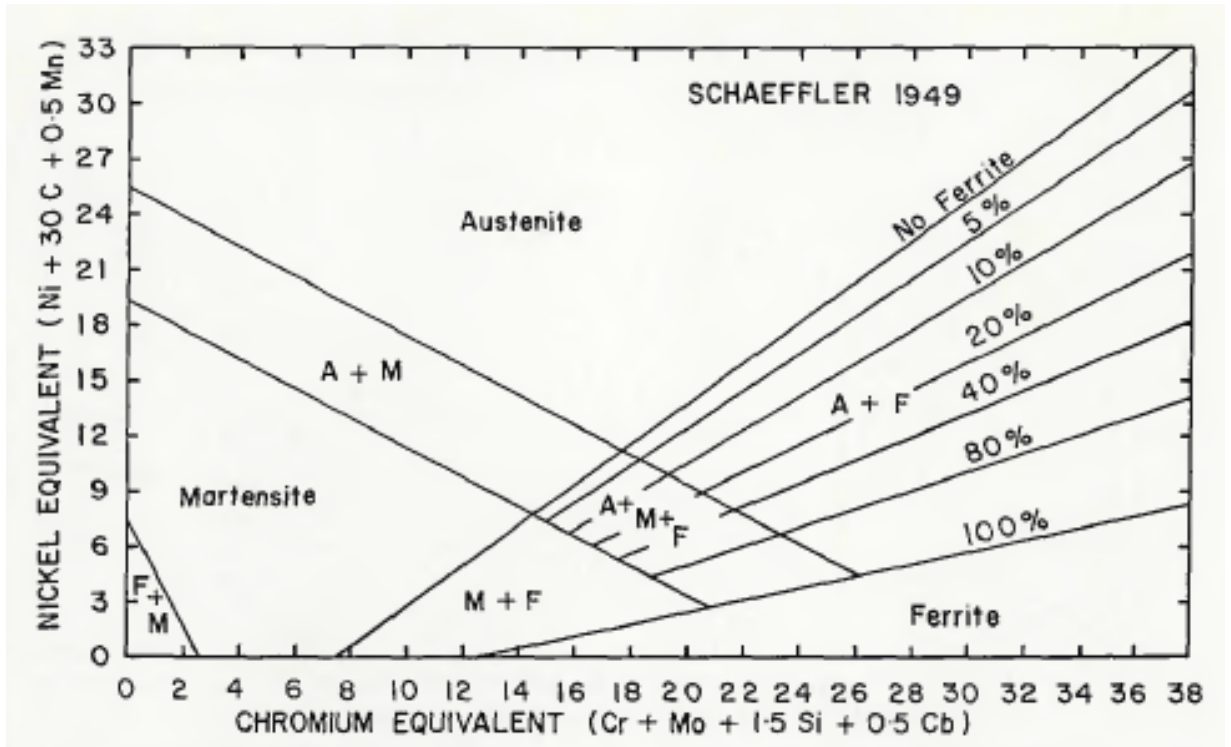


Figure 15: The Schaeffler diagram of 1949, used to predict austenite and ferrite ratio in welded steel by using the chromium and nickel equivalent expression, shown on the axis of the diagram [17]

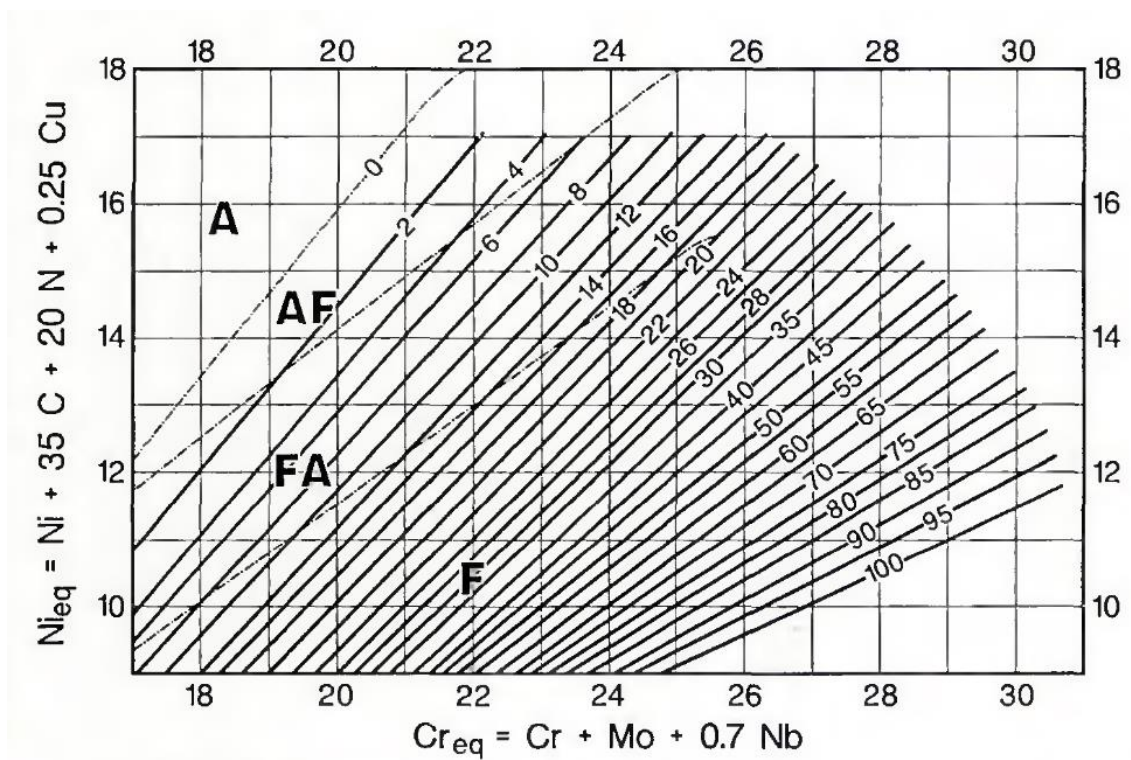


Figure 14: WRC 1992 diagram to predict more precisely ferrite/austenite ratio after welding [18]

2.6. Microstructure morphology in Additive Manufacturing

For multipass welds and wire arc additive manufacturing the observed solidification structures become more complicated as remelting of the previously deposited layers take place and the re-heating of the metal induces grain growth, recrystallisation or precipitation of secondary phases, such as carbides and brittle intermetallic. Yan i.e. [7] investigate grain growth in metal additive manufacturing. They point out the complex microstructures that forms due to the building process of additive manufacturing as additive manufacturing is a layer-to-layer building process in which newly deposited material and a small volume of underlying pre-deposited materials melts and solidifies into one piece as the heat source moves away. They point out that this results in macro-microstructural features such as highly textured columnar grains, complex phases and compositional variations. The understanding of these microstructural properties is the first step to produce desirable structures to achieve parts with desirable or even superior mechanical properties.

In additive manufacturing, the grain growth morphology compares to the process described in the section on solidification mechanisms and solidification structures in welds. The local thermal gradient G and the interface velocity determine the morphology of the solidification structure. As in conventional welding, constitutional supercooling occurs with solute redistribution which causes the liquid at the solidification front to be cooler than the liquidus temperature. Furthermore, the authors mention that generally the G/R near the bottom of the melt pool fall in the region for columnar-dendritic solidification, whereas the equiaxed solidification condition may be satisfied near the melt pool surface where the thermal gradient is lower than that at the bottom of the pool, these are often finer grains compared to the rest of the structure.

Due to the re-melting of previously deposited layers, highly textured large columnar grains are found, that span over multiple layers along the building direction of the AM structure [7].

A specific example for solidification structures in wire arc additive manufactured structures is given by Wang i.e. [21]. They investigated the microstructure and grain growth of a WAAM AISI 316L stainless steel wall. Using the optical microscopy. They observed austenite dendrites with interdendritic ferrite, which aligned nearly vertical along the transverse cross section (dendrites were oriented parallel to the building direction). They stated that grain growth took place parallel to the building direction. EBSD results proofed that most grains in the building direction were oriented along the $\langle 001 \rangle$ direction. Furthermore, they found cellular structures adjacent to the fusion line, which then developed into a fine columnar structure away from the fusion line, which finally, developed into a coarser structure and secondary dendrites. This morphology development was observed and repeated for each layer.

Functionally Graded Materials

In this study, two stainless steels were step wise chemically graded to form a Functionally Graded Material. Functionally graded materials (FGM) are a class of materials in which the chemical composition or microstructure varies as a function of position [3], [22]. FGMs can either be single phase with varying composition or they can be composed of a multiphase microstructure, which is more common [3]. The chemical composition and phase changes in multi-phase FGMs are designed to vary across the bulk volume of the material. The different phases form due to a combination of chemical composition and the thermal cycle experienced.

The first FGMs were designed for the aerospace industry [22] for space plane bodies. The use and application of FGMs has increased and change over the years and now FGMs can also be found in rocket engine components, the spacecraft truss structure, heat exchange panels, reflectors, solar panels, turbine wheels, turbine blade coatings and space shuttles. Their use in aerospace became more common due to the incorporation of completely different physical, mechanical or functional properties into one single part [2]. Additionally, FGMs are used in corrosion-resistant, wear-resistant layers, electronic devices production, as coatings and thermal barrier. FGMs are not only used in the aerospace industry, but also in the automotive, energy and defence industries [22]. In the latter, FGMs can be made to offer penetration-resistant properties by inhibiting crack propagation. They are used for as

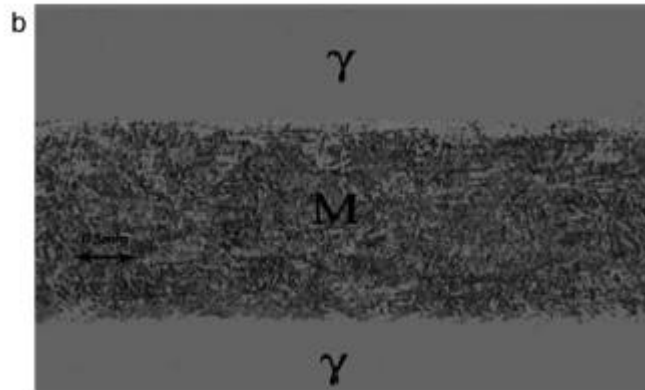


Figure 16: Microstructure of a martensite layer formed between two layers of austenitic region in an austenite-martensite-austenite composition [23].

bullet-proof vests, the traditional Japanese sword, and in armour plates. Another key area of application of functionally graded materials is in the body of bullet-proof vehicles. For the energy industry, FGMs are used for the inner wall of nuclear reactors, thermo-electric converters for energy conversion, solar panels and solar cells, tubes and pressure vessels, graded electrodes for the production of solid oxide fuel, the piezo-electric functionally graded materials for the ultrasonic transducer, the dielectric, the fuel cell and for the turbine blade coatings [22]. From this it can be taken that FGM's are a unique class of materials, which will become increasingly more important for applications that demand extraordinary or unique mechanical, thermal or chemical properties and potential future application areas include applications, where the structural and the engineering uses require a combination of incompatible functions, such as hardness and toughness or for parts that require two completely different material properties on either side of the part.

2.6.1. Phase graded materials

There are different categories of functionally graded materials. There are chemically graded materials, phase graded materials and/or a combination of both to receive unique properties. Nazari and Milan made a phases graded structure [23]. They fabricated an overall austenitic/ferritic microstructure with a layer of either martensite or bainite implemented in the sample, see Figure 16. From this material, Charpy specimen were produced and the ductile to brittle transition temperature of the samples were tested for different location of the changed microstructure relative to the notch. The authors report that the impact energy of the studied FGMs depended on the relative notch tip position to the alpha or gamma regions in addition to its distance from the bainite or martensite layers. Thus, strategically changing properties of the part to receive non uniform material properties over the different axis of the part.

2.6.2. Chemically graded materials

The second and third category of FGMs are chemically graded materials, which change phases as a result of the chemical change. In this study, a dissimilar metal functionally graded material is investigated, however it is worth mentioning that also metal-ceramic graded materials have been investigated in the past. Shabana i.e. [24] investigated stresses due to differential thermal expansion coefficients in a metal-ceramic FGM, made by pressure less powder sintering. A 15 mm high nickel-alumina sintered cylinder was successfully sintered. Put at al. [25] investigated two different types of gradients: a metal-ceramic and a symmetric sintered $\text{Al}_2\text{O}_3/\text{ZrO}_2/\text{Al}_2\text{O}_3$ FGM. Using the transitional change in chemical composition, changing hardness profiles due to the chemical composition were observed. Additional to bonding strength and hardness values, the use of FGM's may also lead to the reduction of overall (material) costs, as stated by Abe and Sasahara [26], who reported that by using a Ni-based alloy on the outer surface on a stainless steel, the overall costs of the product could be minimised, while maintaining the high corrosion resistance and high heat resistance of the Ni-based alloy.

Chemical gradients from dissimilar metals, such as iron and aluminium have also been investigated. Shen i.e. [27], have produced an iron aluminide, fabricated a Fe-FeAl Functionally Graded Material. The process they used was wire arc additive manufacturing. In their paper they describe the process of using low-carbon steel and grading the component up to 55 at. % aluminium. Figure 17 shows a gradual increase of aluminium over the structure. The actual composition indicates a smooth chemical composition, which indicates that diffusion/homogenisation takes place during fabrication as the design is based on a step wise change in composition.

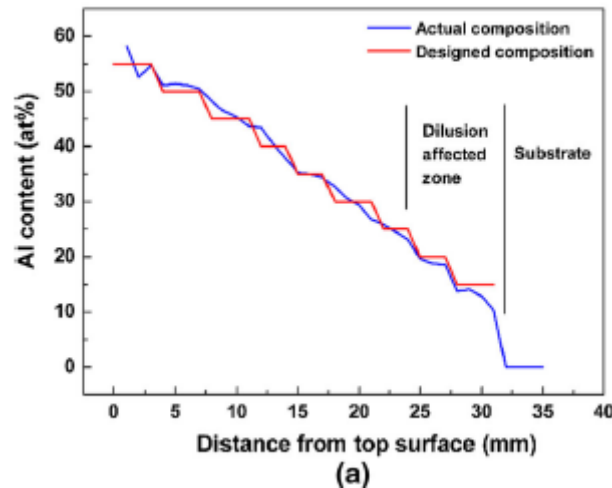


Figure 17: EDS results (blue) for the compositional gradient of mild steel and Al, plotted to the designed composition. A very smooth gradient was observed [27].

2.6.3. Production techniques of chemically graded materials

Depending on the requirements for dimensions, chemical composition, chemical path and mechanical requirements of the functionally graded material, various processes are used to fabricate bulk functionally graded materials. Additive manufacturing methods such as wire arc additive manufacturing were implemented [26], [27] and laser metal deposition (LD/LMD) were used frequently [2], [28], [1], [29],[30]. However, for graded structures with chemical gradients of around 1 mm and thin films, Chemical Vapour Deposition (CVD) and Physical Vapour Deposition (PVD) were used [22]. Another process for producing less dense, i.e.

porous, FGMs is sintering, such as pressure less powder sintering [24]. Although all techniques are very different in nature, their common nominator is the close control over added material, whether in powder, liquid or solid (wire) form.

2.6.4. Functionally graded stainless steels

As the present study investigates functionally graded stainless steels, it is worth noting the previous research studies performed for functionally graded stainless steels. In all papers referred hitherto, laser melting deposition is used to fabricate the FGMs. So called road-mapping, which is the planning of the composition path to avoid brittle phases, is generally applied.

Nam et al. [28] investigated the process parameters and deposition properties of a FGM graded from AISI 316 to mild steel. They compared the impact of using a transitional gradient as compared to welding AISI 316 stainless steel directly on mild steel in which the transition is more abrupt. They observed that when the AISI316 stainless steel was directly deposited on the mild steel many pores and cracks were created at the interface. However, when the FGM was produced by using Fe and AISI316 powder the defects occurring at the interface of the first layer could be avoided. Nam et al. reported that no intermetallic compounds were found in the structure.

Zhang et al. [2] fabricated and analysed a functionally graded stainless-steel using laser melting deposition (LDM), using a similar composition to AISI 316 stainless steel. The authors reported the microstructure to be composed of columnar dendrites, epitaxially growing from the substrate with some equiaxed dendrites in the top region of the part. The phases present within the part were analysed according to the $Cr(eq)/Ni(eq)$ ratio using XRD, see Figure 18. As the content of the strong ferrite forming and carbide forming element Cr was relatively high in the alloy powders, $(Cr, Fe)_7C_3$ carbide particles were formed. The increased hardness was attributed to the increase in the $(Cr, Fe)_7C_3$ carbide content with the increase of the $Cr(eq)/Ni(eq)$ ratio of the alloy powder.

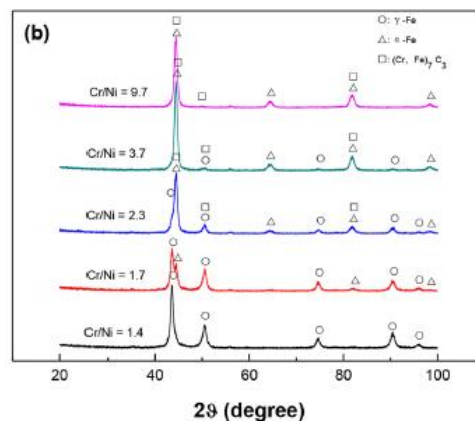


Figure 18: XRD spectra for the functionally graded stainless steel, it shows that carbides formed [2].

Hofmann *et al.* [1] graded Invar 36 to AISI 304L in a radial gradient. The authors used road mapping to avoid certain (brittle) phases. By Vickers hardness tests and XRD they showed that they successfully created gradients in composition without forming brittle phases. Similarly, W. Li *et al.* [29] fabricated a FGM from Ti-6Al-4V to AISI316. The authors used transition composition route via V, Cr and Fe to avoid the formation of intermetallic phases. They observed an elongated lathy microstructure using SEM, with small epitaxial grains. The microstructural features were explained by the high cooling rates during laser melting deposition processing. They report that the formation of any brittle phases was avoided based on XRD and Vickers hardness testing. The material remained relatively soft.

2.6.5. Formation of secondary phases in Functionally Graded Materials

Due to the change in chemical composition for a chemically graded metal, the formation of secondary phases has been identified as a hazard [8]. A first indication for the formation of brittle phases is an unexpected increased hardness value, that exceeds the hardness of the used bulk materials. In extreme cases, this may lead to sudden fracture during welding [8]. One way to avoid the formation of brittle phases, is path planning: road-mapping the graded structure, to avoid the formation of brittle phases. Eliseeva *et al.* [31] used a Machine Learning approach to map undesirable regions as 'obstacles'. They then validate their results by fabricating a graded bulk sample from AISI 316L stainless steel to pure Cr. To validate this data, they heat treated the sample at 900 °C for 8 h and found significant fractions of the phase in the not mapped sample. However, using road-mapping they reported a decrease in sigma phase, after the heat treatment. The reason for the lowering in sigma phase, was the decrease in nickel content for the road-mapped sample.

In this chapter additive manufacturing and the solidification behaviour of wire arc additive manufacturing has been discussed. Functionally graded materials were introduced, and the possible formation of brittle are identified as a possible hazard when grading stainless steel.

3. Materials and Methods

3.1. Introduction

This chapter provides an overview of the experimental equipment and the welding conditions applied to construct the walls. In this study three walls were constructed. The first wall is entirely built from an austenitic stainless steel wire, AISI 316L, Experiment A. For the second wall the same austenitic AISI 316L and a ferritic AISI 430L stainless steel wire were simultaneously fed with the same and constant wire feed rate, Experiment B. A graded composition is obtained in the third experiment by gradually changing the composition in the construct by changing the individual wire feed rates while maintaining the same total deposition rate, Experiment C.

3.2. Materials

In this project, stainless steel wires were used as building material. Their compositions obtained from X-Ray Fluorescence (XRF) can be found in Table 4. The welding wires used were commercially available AISI 316L and AISI 430L, both with a diameter of 1.0 mm. The letter L indicates low carbon content. The carbon content mentioned in the table is based on information from the consumable supplier. The substrate materials were austenitic stainless AISI 316 steel plates with thickness 10 mm. As is shown in Table 4, AISI 316L and AISI 430L stainless steel greatly differ in nickel content. AISI 316L stainless steel is composed of approximately 10 wt.% nickel, while AISI 430L stainless steel has less than 1 wt.% nickel. Based on the chemical composition measured and including the indicated carbon content, the chromium and nickel equivalents, discussed in the previous chapter, are here calculated from all materials, see Table 5. The calculation of the chromium and nickel equivalents according to Schaeffler and the welding research council Welding Research Council (WRC) mentioned in section 2.5.

Table 4: XRF results of used materials [in wt. %]; data indicated with denotation (1) is based on information from the consumable supplier

| Element | Fe | Cr | Ni | Mo | Si | Mn | Na | Zn | Cu | Cl | Ta | Al | Ti | V | Mg | Ca | P | K | Pb | S | Nb | C(1) | N(1) |
|----------------------|--------|--------|--------|-------|-------|-------|-------|-------|-------|-------|-------|-------|-------|-------|-------|-------|-------|-------|-------|-------|-------|-------|-------|
| AISI 316 L wire | 62.304 | 17.676 | 12.681 | 2.582 | 2.43 | 1.579 | 0 | 0 | 0.231 | 0 | 0.132 | 0.103 | 0.089 | 0.059 | 0 | 0.037 | 0.033 | 0.032 | 0 | 0.024 | 0.009 | 0.01 | 0 |
| AISI 430L wire | 77.96 | 15.892 | 0.132 | 0.041 | 0.829 | 0.775 | 0 | 2.336 | 0.582 | 0.057 | 0 | 0.245 | 0.117 | 0.111 | 0 | 0.396 | 0.009 | 0.185 | 0 | 0.035 | 0.298 | 0.009 | 0.018 |
| AISI 316 substrate | 67.227 | 15.911 | 10.43 | 1.953 | 0.475 | 1.408 | 0.806 | 0.583 | 0.416 | 0.241 | 0 | 0.184 | 0 | 0.084 | 0.054 | 0.044 | 0.041 | 0.068 | 0.038 | 0.028 | 0.009 | 0.08 | 0 |
| austenitic substrate | 70.38 | 17.376 | 9.039 | 0.33 | 0.595 | 1.815 | 0.048 | 0 | 0.193 | 0 | 0.076 | 0.009 | 0.016 | 0.056 | 0 | 0 | 0.021 | 0 | 0.016 | 0.023 | 0.006 | 0.08 | 0 |

3.3. Welding arrangements

In this project, wire arc additive manufactured products were produced via Gas Tungsten Arc Welding (GTAW) combined with a double wire feeding system. In GTAW an arc is established between a tungsten electrode and the substrate. This process allows feeding two different wires without affecting the arc stability significantly. In addition, the system allows to vary the wire feed rates independently, which is required to create graded structures. In Figure 19 and Figure 20 for a schematic sketch of the welding setup and a photograph of the welding setup with double wire feed holder is depicted.



Figure 20: Photograph of welding torch with two wire feed holders was moved over a clamped and stationary workpiece for simultaneous wire feed at the electrode

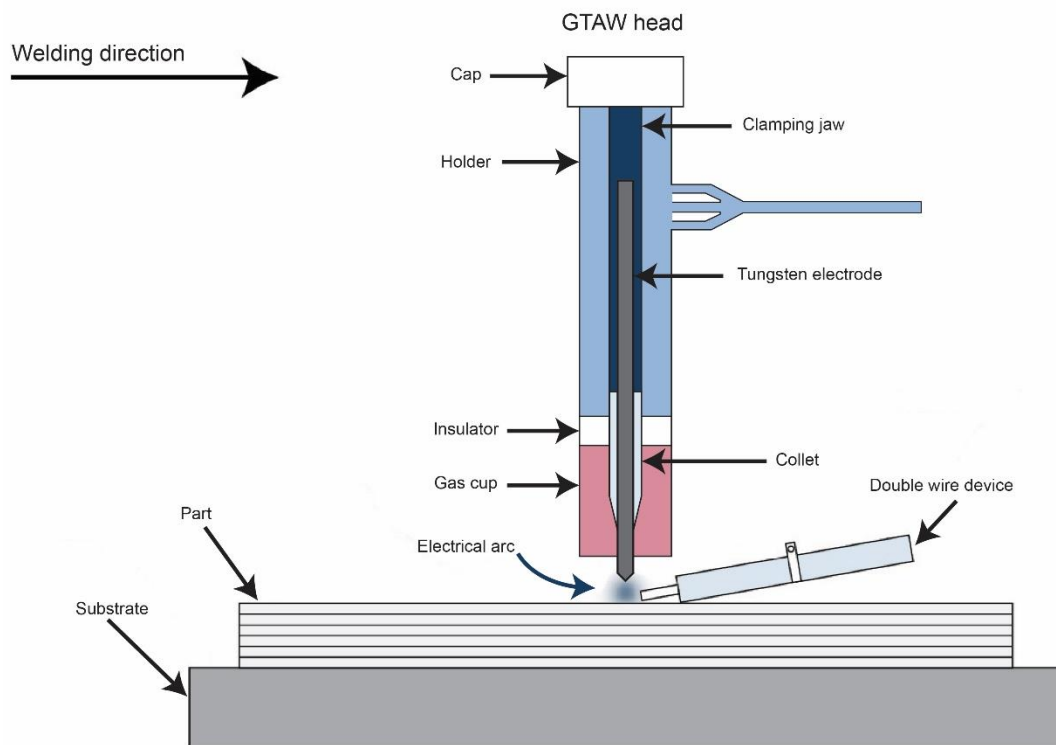


Figure 19: Sketch of the welding arrangements, showing the welding torch, part and double wire device from the front view

Table 5: Calculated nickel and chromium equivalent for all materials. By implementing these values in the Schaeffler and the WRC 1992 diagram an estimate for austenite and ferrite percentage was made

| Material | Schaeffler 1949 | | WRC 1992 | | Phase fractions | |
|----------------------|-----------------|----------------|----------------|----------------|-------------------------------|-----------------------------|
| | Ni(equivalent) | Cr(equivalent) | Ni(equivalent) | Cr(equivalent) | Phase percentage (Schaeffler) | Phase percentage (WRC 1992) |
| AISI 316 L wire | 13.7705 | 23.9075 | 13.08875 | 20.2643 | 20% Ferrite 80% Austenite | 6% Ferrite 94% Austenite |
| AISI 430 wire | 0.7895 | 17.3255 | 0.9525 | 16.1416 | 100% Ferrite | 100% Ferrite |
| AISI 316 substrate | 13.534 | 18.581 | 13.334 | 17.8703 | 100% Austenite | 100% Austenite |
| austenitic substrate | 12.3465 | 18.6015 | 11.88725 | 17.7102 | 5% Ferrite 95% Austenite | 4% Ferrite 96% Austenite |

3.4. Welding specifications

The welding was performed using a Migatronix TIG Commander AC/DC Welder. The electrode used was a WGLa Tungsten 15, with a diameter of 2.4 mm and a top angle of 90°, direct current electrode negative (DCEN). During welding an arc length of approximately 3 mm was used. It should be mentioned that as the height of the deposit is not entirely flat the arc length changes slightly during the deposition on top of the previously deposited layer. To shield the workpiece from the environment, a shielding gas mixture at a flow rate 12 l/min. was supplied, using a gas cup with a diameter of 12 mm. See Table 6 for a detailed overview per experiment. 50% Ar -50% He was used for all experiments, except for the preliminary experiments for which 100% Ar gas was used.

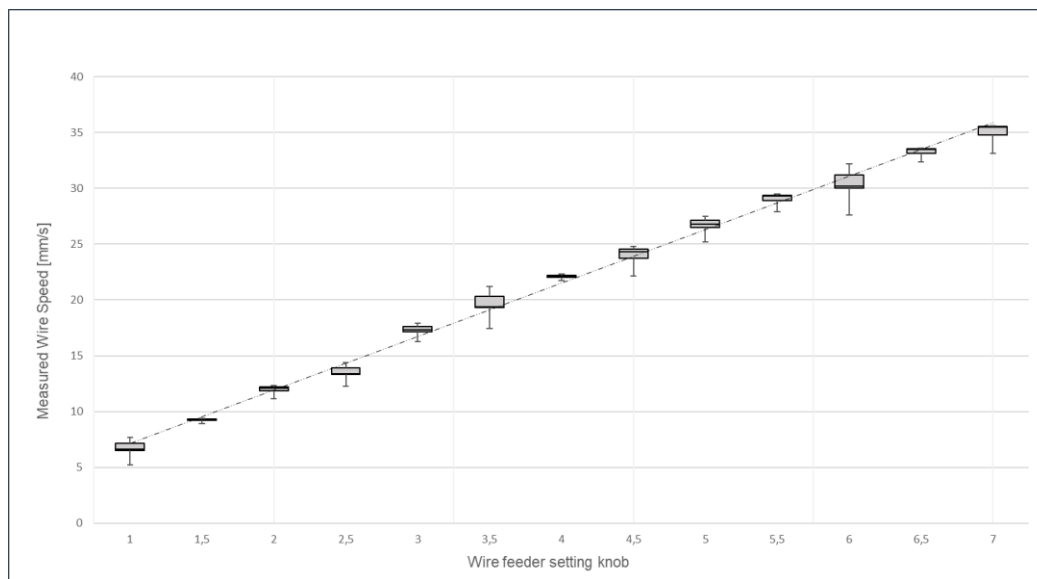


Figure 21: Wire Feed Calibration Curve. The Wire feed speed was measured for different settings, and the error calculated.

Two electronically controlled wire feeders of type Migatronix KT4 were used to feed the wires. The wire feeding system was calibrated to make sure that the required feed rates could be accurately selected. For experiment A, a single wire was supplied, for experiment B and C the double wire feeding system was used. See Figure 21 for a typical error estimate of the wire feed calibration, note that the feed setting numbers differ per wire feeder. The power source was combined with a CNC motion system (XYZ robot) programmed by DMC Smart Terminal Software. During welding the workpiece was clamped and maintained stationary, while the torch with the wire feed holder was moved at the requested speed, see Figure 20. The wires were fed at an angle of 22-25° and were positioned approximately 1 mm above the plate. An appropriate deposition speed was selected based on the

characteristics of the deposits (bead width, height, aspect ratio and uniformity) obtained from preliminary experiments, discussed in section 4.1.

The constructed walls were all single bead depositions. After each layer was completed, the torch was moved to its original 'X' position and the 'Z' position was adjusted with a few millimetres to maintain the selected arc length. The wall consisted of at least 10 layers, see Table 6 for the number of layers per experiment and average layer height.

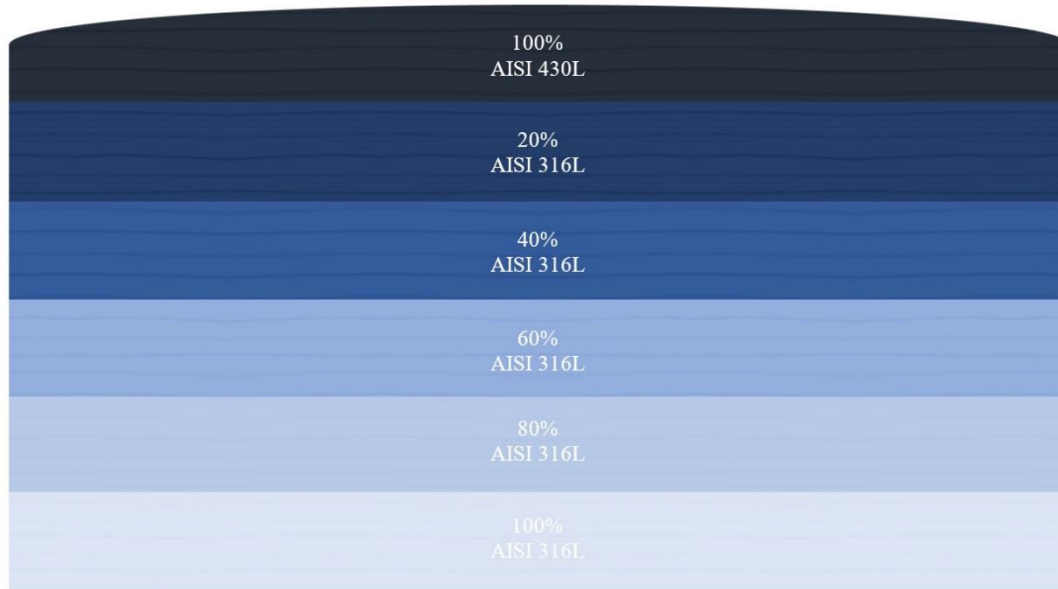


Figure 22: Experiment C: Schematic overall wire speed for deposits of several layers, gradient in steps from AISI 316L at the bottom to AISI 430L at the top

The general welding conditions are listed in Table 6 and the wire feed rates per experiment are provided in Table 8. During welding the arc voltage was measured between the tungsten electrode and the workpiece and the current was measured by a clamp on around the cable that went to the workpiece. The data was recorded by a weld monitor, the Triton AMV 4000 from which average values of current and voltage were obtained. The heat input was calculated according to equation 2.1. A process efficiency η of 0.7 for GTAW is assumed [6]. Using the available data, the average heat input can be calculated.

3.5. Temperature measurements

During welding the transient temperature is measured at specific locations of the print wall by means of a discharge welded K-type thermocouple with a wire diameter of 0.25 mm. The locations of the thermocouples are indicated in Figure 23 and have varying distances towards the deposition site. The thermocouples data was collected by the Yokogawa DL750. The sample rate used was 100 Hz. From the collected data the peak temperature, the cooling rate and the estimated interpass temperature were derived. The cooling rate can be approximated by using equation 5.1 and the temperature data collected from the temperature measurements.

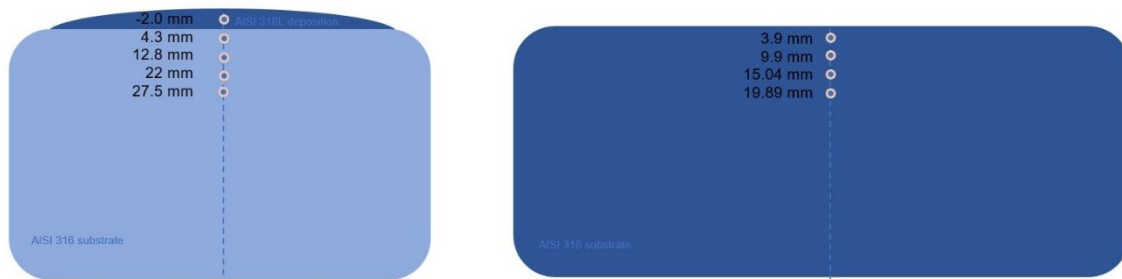


Figure 23: Distance [in mm] of the thermocouples from the substrates top edge. The K-type thermocouples were discharge welded on the substrate before the start of the experiments. Note that after the deposition of 11 layers, an additional thermocouple was welded

3.6. Preliminary welding experiments

Preliminary experiments were conducted to obtain the relationship between welding conditions and deposit characteristics. The welds were visually inspected, focussing on the shape, bead dimension and uniformity. To obtain a suitable set of weld parameters, substrate 2 was used to deposit a single pass of the AISI 316L consumable on the face plate. The wire feed rate was varied between 7.2-56.6 mm/s. The current varied between 100-160 A. The travel speed varied between 3-7 mm/s. The arc length was set to 3 mm for all deposits. For the welding with double wire feeding, a few iterations were required to obtain satisfactory results based on visual inspection. In addition, tests were conducted to optimise the process for multiple passes. 2 to 4 passes were deposited on top of each other. The torch to sample distance was maintained at 3 mm. Travel speed was 5 mm/s, wire reed rate was 31 mm/s, while the current was varied between 125 and 155 A. The total length of each weld was 65 mm to ensure that steady state conditions were reached. From the preliminary experiments welding conditions were obtained to produce the three walls indicated as Experiment A to C.

3.7. Parameter per experiment

Each parameter and used method per experiment is listed in the following sections and an overview is found in Table 6.

3.7.1. Experiment A: 316L stainless steel

Further iterations on the side of the plate led to a travel speed of 5.5 mm/s. arc length of 2.5-3 mm, 140 A current and wire speed was increased to 34 mm/s. These parameters were implemented to fabricate the AISI 316 substrate. 23 passes were deposited on the side of the 10 mm thick plate, 80 mm in height and 100 mm long. Four thermocouples were welded on the substrate, near to the weld surface, one thermocouple was added after the 11th layer was deposited, see Figure 23. Current and voltage measurements were taken.

3.7.2. Experiment B: 316L & AISI 430L in equal portion

For the fabrication of this structure, the same travel speed was used in both wire feeders. Welding current was at 140 A, arc length 3 mm, travel speed 5.5 mm/s and wire feed speed 20.5 mm/s. Temperature, current and voltage were not measured.

3.7.3. Experiment C: 316L & AISI 430L functionally graded

Using the step-size change in wire speed (Figure 22, Figure 23), a graded structure was built on a 200 m long, 10 mm thick and 80 mm high plate of steel. Welded was on the 200

mm side of the AISI 316 steel plate. Travel speed was 5.5 mm/s. Total wire feed rate was 43 mm/s. The structure was welded with two wires: AISI 430L and AISI 316L on the side of an AISI 316 plate. Thermocouples were placed in the centre of the plate. See Figure 23 for the positions of the thermocouples. The wire speed was changed every few layers to obtain the graded structure.

Table 6: Parameter overview per experiment

| Deposition parameters | Experiment A | Experiment B | Experiment C |
|------------------------------|---------------------------|--------------------------------|------------------------------------|
| Current (I) | 140 A | 140 A | 140 A |
| Voltage (U) | 12.1 V | NaN | 11.9 V |
| Wire feed speed | 2.1 m min^{-1} | 1.23 m min^{-1} each | $0\text{-}2.58 \text{ m min}^{-1}$ |
| Travel speed | 0.33 m min^{-1} | 0.33 m min^{-1} | 0.33 m min^{-1} |
| Electrode | WGLa Tungsten 15 | WGLa Tungsten 15 | WGLa Tungsten 15 |
| Electrode diameter | 0.002 m | 0.002 m | 0.002 m |
| Contact-tip-to-work distance | 0.003 m | 0.003 m | 0.003 m |
| Gas cup diameter | 0.012 m | 0.012 m | 0.012 m |
| Shielding gas | 50% Ar -50% He | 50% Ar -50% He | 50% Ar -50% He |
| Gas flow rate | 12 l min^{-1} | 12 l min^{-1} | 12 l min^{-1} |
| Wire feeder angle | 68° | 65° | 65° |
| Interpasse temperature | 343 K | - | 348 K |
| Pulse mode | No pulse | No pulse | No pulse |
| Polarity | Direct Current Electrode | Direct Current Electrode | Direct Current Electrode |
| Number of layers | 23 layers | 10 layers | 28 layers |
| Layer height | 0.8 mm | 1.1 mm | 1.1 mm |

3.7.4. Heat treatment

As part of the heat treatment experiments, sample sections from Experiment A, B and C were taken. They were cut and heated to 600°C for 90 hours, taken out, air-cooled, reheated to 850°C, held for 90 hours, taken out and air-cooled.

3.8. Characterisation of the microstructure

3.8.1. Sample preparation

From the welded structures, cross sections were cut for sample preparation by an abrasive cut-off wheel in the transverse direction, comparable to typical weld cross-sections as shown in Figure 24. The samples were hot mounted in conductive resin and according to common practice wet ground, up to 4000 grit, and polished up to 1-micron. The resin was then broken from the sample to receive a fully polished sample with a mirror-like finish. The samples were then etched to reveal their macro- and microstructure. As Kalling's n^o2 only reveals austenite and ferrite in this alloy, different etchants were tested to indicate other constituents. 40% NaOH and 10% Oxalic Acid both revealed the individual grains for austenitic and duplex structures, contrasting phases and revealed smaller phases with (possible) sigma phase carbides, however 40% NaOH had better results in etching sigma phase, which is the reason why all micrographs are etched with 40% NaOH. The only exception was made for the upper part of experiment C, which were etched by using a combination of Viella's solution immersion and 40% NaOH electro etching as Viella's reveals

the ferritic grain boundaries. Table 7 provides a detailed overview of the etchants used in this study.

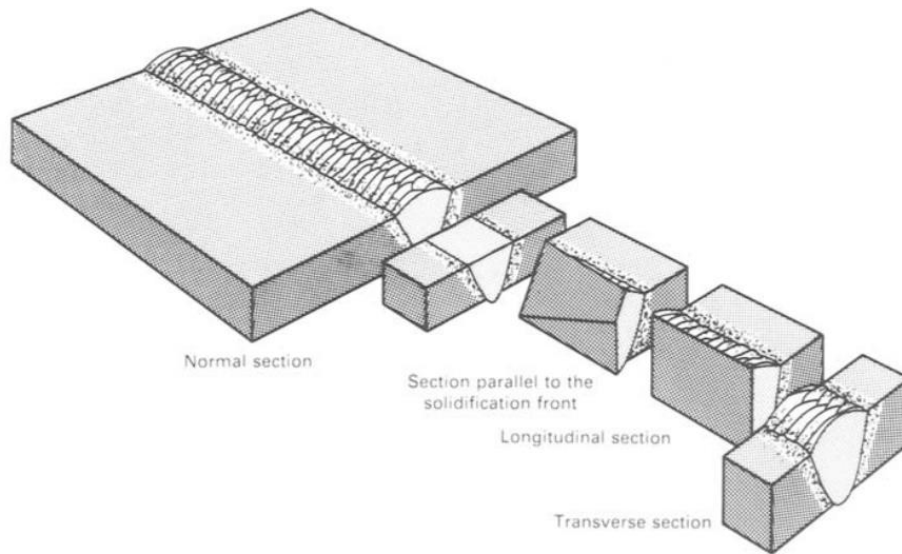


Figure 24: Typical cross sections in weld characterisation [41]

3.8.2. Optical Microscopy

Optical Microscopy (OM) was applied to obtain the macro- and microstructure of the deposited beads. A Keyence VHX-100 digital microscope was used to determine the overall bead/layer shape and to quantify the grain size and morphology, while a Leica DMLM was used to determine features at higher magnification such as the distribution of phases and precipitates.

Table 7: Overview of etching methods and phases they etch for stainless steels

| Etchant Name | Composition | Method | Notes |
|--------------------------|---|------------------------|--|
| Kalling's n2 | 5gr $CuCl_2$, 100 ml HCl. 100 ml Ethyl alcohol. diluted by 2/3 Ethyl alcohol | Immersion 7 s | Etches ferrite strongly; austenite is slightly etched; carbides are not attacked |
| 40% NaOH | 40 gr sodium hydroxide. 60 ml H_2O | Electrolytic 2V 30 s | Colour stains sigma - orange-brown and ferrite - light-brown |
| 10% Oxalic Acid | 10 gr oxalic acid. 100 ml H_2O | Electrolytic. 3V. 15 s | Etches carbides - strong; sigma - outline; austenite - moderate; ferrite is not attacked |
| Viella's solution | 5 ml HCl. 2 gr Pitric Acid. 100 ml Ethyl alcohol | Immersion | Reveals grain boundaries ferrite in 430 ferritic stainless steel |

3.8.3. Scanning electron microscopy

Scanning electron microscopy (SEM) was used in this project for microstructure evaluation at high magnifications. The JOEL JEM Plus equipped with an energy-dispersive (EDS) detector to identify the local elemental composition. Especially for the graded structure, EDS was used to quantify mixing of the double wire weld in the transverse direction and between the differently composed layers of the graded structure.

3.8.4. X-ray Fluorescence

X-Ray Fluorescence (XRF) reveals the bulk chemical composition of the material by the bombardment of the high-energy x-rays of gamma-rays and measurement of characteristic secondary (or fluorescent) x-rays of the material. The chemical compositions of the wires and substrates were measured by XRF and are indicated in Table 4.

In this project, specific emphasis was on the chemical composition at different 'heights' in the walls. In the third experiment (the graded structure) the wall was sliced in normal sections at different heights of the wall, which allowed for characterisation of the global chemical composition at different layers heights. The measured data is compared with the expected chemical composition based on the amount of the wires supplied by the feeding system. Furthermore, the chemical composition was used to find the local phase equilibrium, giving a starting point for phase identification.

3.8.5. X-ray diffraction

X-ray diffraction (XRD) is used to identify the crystal structure of the built. Using XRD, the different phases and phase fractions can be determined.

Table 8: Wire Feed Speed per layer for each wall

| Layer | Experiment A | | Experiment B | | Experiment C | |
|-------|---------------------------|---------------------------|---------------------------|---------------------------|---------------------------|---------------------------|
| | AISI 316 L Wire Feeder | AISI 430 L Wire Feeder | AISI 316 L Wire Feeder | AISI 430 L Wire Feeder | AISI 316 L Wire Feeder | AISI 430 L Wire Feeder |
| | $m \text{ min}^{-1}$ |
| 1 | 2.1 | 0 | 1.23 | 1.23 | 2.58 | 0 |
| 2 | 2.1 | 0 | 1.23 | 1.23 | 2.58 | 0 |
| 3 | 2.1 | 0 | 1.23 | 1.23 | 2.58 | 0 |
| 4 | 2.1 | 0 | 1.23 | 1.23 | 2.58 | 0 |
| 5 | 2.1 | 0 | 1.23 | 1.23 | 2.58 | 0 |
| 6 | 2.1 | 0 | 1.23 | 1.23 | 2.58 | 0 |
| 7 | 2.1 | 0 | 1.23 | 1.23 | 2.06 | 0.52 |
| 8 | 2.1 | 0 | 1.23 | 1.23 | 2.06 | 0.52 |
| 9 | 2.1 | 0 | 1.23 | 1.23 | 2.06 | 0.52 |
| 10 | 2.1 | 0 | 1.23 | 1.23 | 2.06 | 0.52 |
| 11 | 2.1 | 0 | | | 1.55 | 1.03 |
| 12 | 2.1 | 0 | | | 1.55 | 1.03 |
| 13 | 2.1 | 0 | | | 1.55 | 1.03 |
| 14 | 2.1 | 0 | | | 1.55 | 1.03 |
| 15 | 2.1 | 0 | | | 1.03 | 1.55 |
| 16 | 2.1 | 0 | | | 1.03 | 1.55 |
| 17 | 2.1 | 0 | | | 1.03 | 1.55 |
| 18 | 2.1 | 0 | | | 1.03 | 1.55 |
| 19 | 2.1 | 0 | | | 0.52 | 2.06 |
| 20 | 2.1 | 0 | | | 0.52 | 2.06 |
| 21 | 2.1 | 0 | | | 0.52 | 2.06 |
| 22 | 2.1 | 0 | | | 0.52 | 2.06 |
| 23 | 2.1 | 0 | | | 0 | 2.58 |
| 24 | | | | | 0 | 2.58 |

| | | |
|----|---|------|
| 25 | 0 | 2.58 |
| 26 | 0 | 2.58 |
| 27 | 0 | 2.58 |
| 28 | 0 | 2.58 |

3.8.6. COMSOL heat modelling for estimation of cooling rates

For the assessment of microstructural development, information on the thermal history and spatial thermal gradients is essential. In wire arc additive manufacturing, the thermal history is further complicated by the layer-by-layer deposition of material, which results in thermal cycles, where at any given point in the structure, the material is heated and reheated during the deposition of further layers. Therefore, as discussed in Section 3.5, thermal measurements were carried out in this work. This was done to measure the temperature development over time in the substrate and at considerable distance to the deposition of molten material, as shown in Figure 23. The information obtained at these points, however, is for the thermal cycles experienced further away from the heat source. This is due to the limitation that thermocouples can only be attached to substrate or fully solidified material and can't be placed in the deposition path on a top layer.

To obtain thermal information in the deposited structure a thermal model was created in COMSOL Multiphysics® [42], based on earlier work for heat modelling of TIG welding carried out by Van der Aa [32]. This model implements a Goldak volume heat source [33] to model the heat input of the welding arc. The addition of mass was accomplished by a time-dependent Heaviside function, which added the contribution of thermal parameters of a region based on the modelled position of the laser spot, where mass deposition takes place. The thermal parameters themselves were implemented as a temperature-dependent function. Model-estimated peak temperatures and cooling rates were compared to thermal measurements by placing model probes at comparable locations in the model domain corresponding to the substrate. Furthermore, two model probes were added to the model at locations where thermal measurement was not possible, to estimate peak temperature and cooling rate within the layers at time of deposition.

4. Results

4.1. Introduction

In this chapter, the results of the wire and arc additive manufacturing conditions and heat treatments on the deposition geometry and microstructural evolution are presented. As mentioned in chapter 3, three deposition experiments were designed. Before welding the multi-layered structures, preliminary single pass experiments were conducted to determine appropriate welding conditions and weld geometries. The results of these experiments will be discussed first to motivate the parameter selection of the final experiments. The first multilayer experiment, Experiment A, is a structure of 23 passes of AISI 316L stainless steel. In Experiment B a structure of 10 passes is produced, using AISI 316L and AISI 430L stainless steel in equal portion. Finally, in Experiment C, a graded structure of 28 passes using AISI 316L and AISI 430L stainless steel is made, in which the composition gradually changes from an austenitic to a ferritic phase.

4.2. Preliminary Results

4.2.1. Single Bead deposits

For the selection of deposition parameters for the multiple wall constructs, the effect of three welding **parameters** on the deposition geometry were investigated, i) the welding **current**, ii) the **travel speed** and iii) the **wire feed rate**. An overview of the welding arrangements used can be found in section 3.3. It should be noted that for the preliminary experiments Argon gas shielding was applied, whereas for the final experiments a 50%Ar-50% He gas shielding was used.

Single-pass AISI 316L stainless steel welds were deposited on the faces of three 150x80x10 mm³ AISI 316 stainless steel plates. For each set of preliminary experiments, two parameters were kept constant, while the third parameter was varied. After welding, the plates were cut in the transverse direction of the weld bead. The results were evaluated by judging each weld in terms of

- Homogeneity of deposition,
- Melting of the wire and
- Height/Width aspect ratio of the transverse section.

The objective of the preliminary tests is to find a set of parameters leading to homogeneous, straight lined bead, for which the wire is fully melted with a high aspect ratio of the cross-section. The high aspect ratio is needed to minimize the number of welds necessary to build a vertical structure. Deviations from a straight deposit line should be kept minimal as these may introduce defects in the subsequent beads due to arc fluctuations.

The first parameter investigated was the welding current, it was decreased in steps of 10 A, starting from 160 A, with a fixed wire feed speed of 31 mm/s and a constant travel speed 6 mm/s.

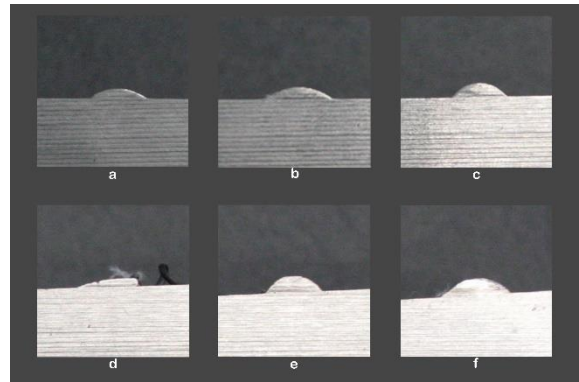


Figure 26: Influence of varying travel speed; left: top view; right: transverse cross section; a. 7 mm/s; b. 6 mm/s; c. 5 mm/s; d. 5 mm/s; e. 4 mm/s; f. 3 mm/s

Figure 25 depicts the beads in the order a. 160 A to g. 100 A. For welding currents between 160 and 120 A, the wire was entirely melted, while for the currents of 110 and 100 A the supplied energy was too low to fully melt the wire. For the cross sections of depositions a.-e. an increase of the aspect ratio can be seen for decreasing welding current. A higher aspect ratio is beneficial for the following experiments as this decreases the number of layers needed to build a vertical wall of a certain height. For this argument, deposition e. at with

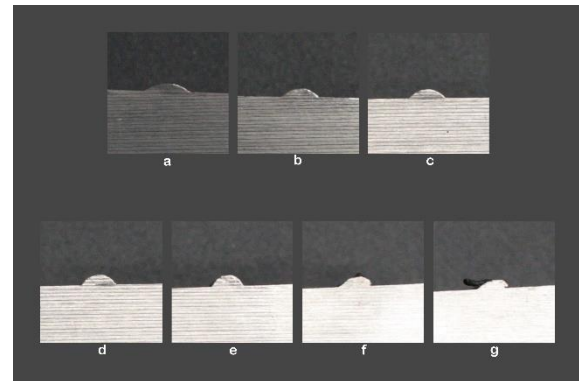
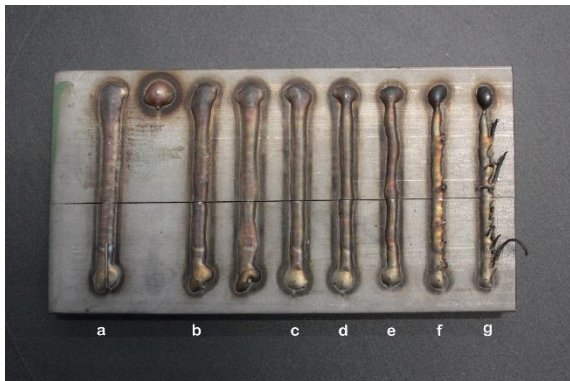


Figure 25: Influence of varying current, left: top view; right: transverse cross section a. 160 A; b. 150 A; c. 140 A; d. 130 A; e. 120 A; f. 110 A; g. 100 A

current of 120 A would be the most favourable setting, however, it can be observed that bead e. is slightly curved, which may lead to strong arc fluctuations and may lead to problems welding additional layers on top. Therefore, the best current setting is around 130-140. In conclusion: when the current is too low, the wire is not fully melted, when it is too high, the bead becomes to flat, which leads to an increase of overall building time.

The second parameter investigated was the travel speed of the welding torch over the plate. Travel speed changes were made by increments of 1 mm/s per bead, lowest was a. 7 mm/s and f. 3 mm/s. In these experiments the wire speed used was 6 mm/s and the welding current was 140 A. In Figure 26 the bead appearances are depicted. All weld beads appear as homogeneous lines and their mass is evenly distributed, except for bead d and f. For bead d, the wire holder at the torch was slightly dispositioned and therefore not properly feeding the wire into the arc, which leads to incomplete melting of the wire (overshooting to the right). Deposit f shows a slight curvature. A low travel speed results in a high heat input in the substrate and a larger deposition volume per unit time causing bead broadening. At starts and stops of the process the geometry of the deposit is different from the steady state condition and therefore are ignored in the evaluations. It appears that the aspect ratio increases with decreasing travel speed. The total welding time per bead increases with lower travel speed. The total mass of the wire that is deposited increases as well, which leads to a higher mass input. This in turn, increases the aspect ratio when the bead is

narrow. In conclusion: when travel speed is too low, the bead broadens. If the travel speed is too fast relative to the wire speed, the bead aspect ratio is low due to the low deposition rate per unit length, eventually a discontinuous bead will be formed.

The third parameter is the wire feed speed. The results of weld geometry changes with decreasing wire speeds are given in Figure 28 a to g. Bead a is slightly curved. In general a reduction in height can be observed except for weld b, which looks different from the previous and the next weld: thinner and a high aspect ratio, which is due to a short interpass time between the two welds. Deposits c and d have a low aspect ratio, while welds f and g are nearly flat. From the results, a higher wire speed seems all favourable regarding the aspect ratio. However, increasing wire speed too much will eventually lead to incomplete melting of the wire. In conclusion: increasing wire speed leads to a higher mass deposition per second, which leads to a high aspect ratio, however, increase it too far and melting becomes inhomogeneous and the bead is curved. A lower wire speed leads to a flatter bead, which is unfavourable for additive manufacturing. As the weld layers should have a high aspect ratio, 35 mm/s and even 38 mm/s and above seem to be acceptable wire speeds.

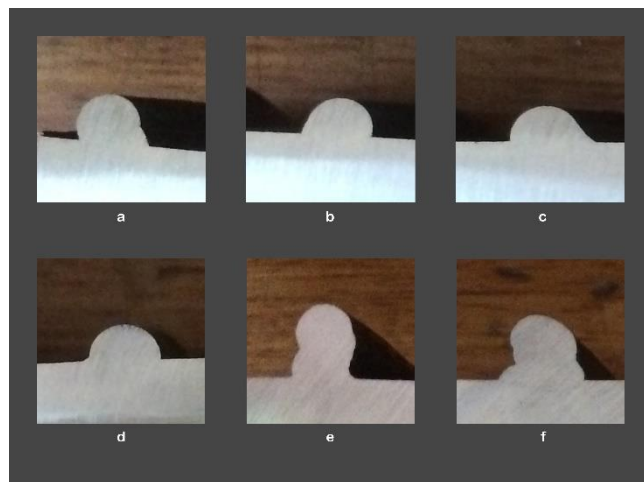


Figure 27: Multiple passes, single bead weld, transverse cross section a. 125 amps, 3 passes; b. 135 amps, 4 passes, c. 145 amps, 3 passes; d. 155 amps, 2 passes; e. 140 amps, 8 passes no direction change in welding; f. 140 amps; 8 passes zig-zag welding

4.2.2. Multi-pass welds

To validate and further develop the weld parameters for wire speed, travel speed and current and layer-to-layer pattern, multiple beads of AISI316L stainless steel were deposited.

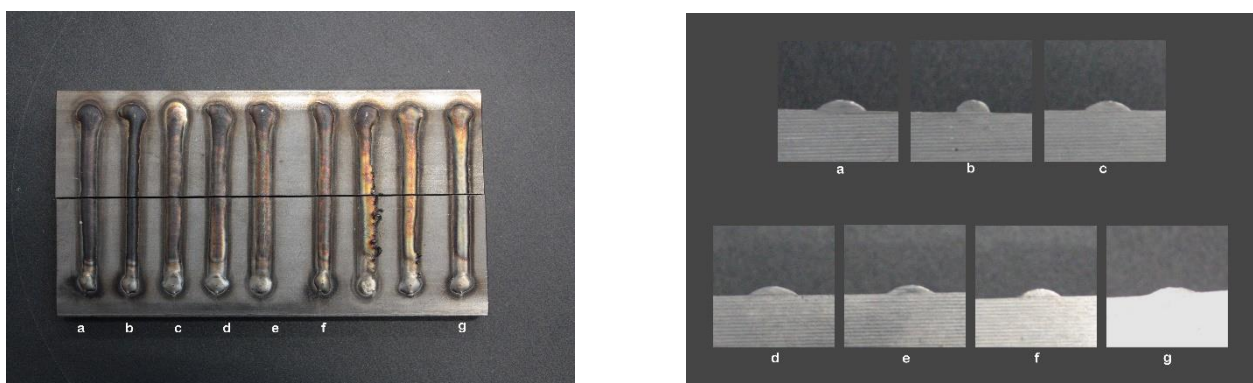


Figure 28: Influence of varying wire speed; left: top view; right: transverse cross section; a 41 mm/s; b. 38 mm/s; c. 35 mm/s; d. 33 mm/s; e. 31 mm/s; f. 28.5mm/s; 25.5mm/s.



Figure 29: Warping of the substrate due to welding on the face of the plate

Weld a-d consists of multiple passes, each changing the weld current 10 A between 125 and 155 A, all welds were deposited without changing the welding direction. Compare Figure 27, the structure was deposited in three passes. The second layer was unintentionally deposited next to the first and the third on top/in between both layers, on the left side, the weld seems to have an undercut, which may point to the fact that the heat input for this setting was too low. Weld b is 4 passes, however, the remelting of the layers beneath hides the visibility of the layer's underneath. Weld deposit c is welded in three passes and has an acceptable aspect ratio. Deposit d are only 2 passes and has also an acceptable aspect ratio. Welds e and f of Figure 27 are 8 passes each; Weld structure e was welded in one direction, while structure f was welded in a zig-zag pattern, changing welding direction 180° each layer. Structure f varied less in height throughout the weld, while structure a-e lost height from weld start to weld end. In conclusion: altering the welding direction will lead to a more homogeneous built. Welding current 140 A yields the best results in height/width ratio, also for multiple welds on top of each other.

4.2.3. Warping of the plates

For the preliminary experiments, the face of the plate was used for welding. Due to the high temperature gradients caused by the constant reheating and remelting of during welding, the plates were distorted, as can be seen in Figure 29. To avoid this distortion welding was carried out on the side face of the 10 mm thick steel plate for experiment A and C [34], as shown in Figure 6. In this welding arrangement the plate has a higher stiffness and mimics the heat flow conditions of an actual 3D printed wall more appropriately.

4.3. Experiment A

In this section the results of the AISI 316L single wire wall structure are given. First the dimension and overall appearance are provided. The temperature cycles are presented in section 4.5.2. This is followed by the results of the microstructure evaluations including the chemical analysis by X-ray fluorescence and phase characterisation by X-ray diffraction.

Based on the preliminary results the welding parameters applied are a welding current of 140 A, a travel speed of 5.5 mm/s and a wire speed 34.8 mm/s. Experiment A was built on the side face of a 100x80x10 mm³ AISI316 steel plate. The sample was turned 180 degrees after each deposition to avoid creating an uneven height of the construct (referred to as zig-zag welding). All welding conditions are listed in chapter 2, Table 6. It should be mention that for the construction of the

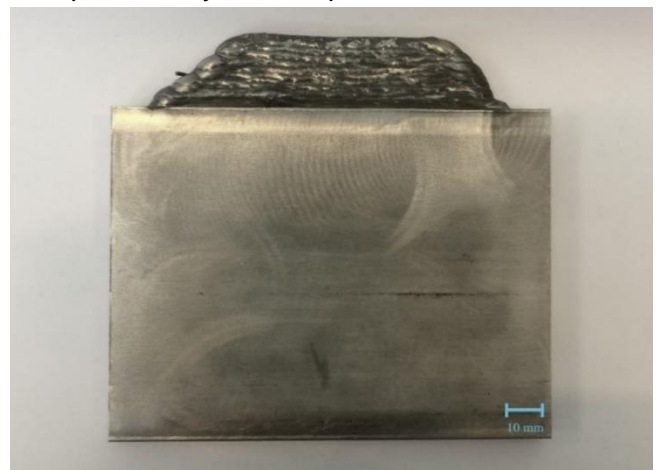


Figure 30 Welded structure using AISI316 wire

final multilayer walls an Argon-Helium mixture was used as shielding gas.

4.3.1. Appearance and dimension

A picture of the resulting wall from Experiment A is shown in Figure 30. The wall was welded in 23 passes. The final walls height was between 18.47 mm and 21.48 mm. The length at the bottom was 82.6 mm and 52.54 mm at the top. The thickness varied between 5.1 mm and 5.8 mm. The length of the deposit was gradually reduced to prevent the arc length from fluctuating to much during deposition. The layers are relatively uniform, however the built is slightly lower in the middle. Each deposited layer is a bit higher at its end points. The picture from Figure 30 was taken after the built was 'cleaned' using an angle grinder to remove the oxide layer partially.

4.3.2. Temperature

Interpass temperature was measured at the upper thermocouple, see section 3.5. The next deposition was only made when the temperature dropped below 75°C. For Experiment A, the welding of the first 12 layers, only the lower two thermocouples worked and from layer 13 additional thermocouples were welded, the upper thermocouple was situated in the second deposited layer of the structure, see Figure 23. During these experiments the

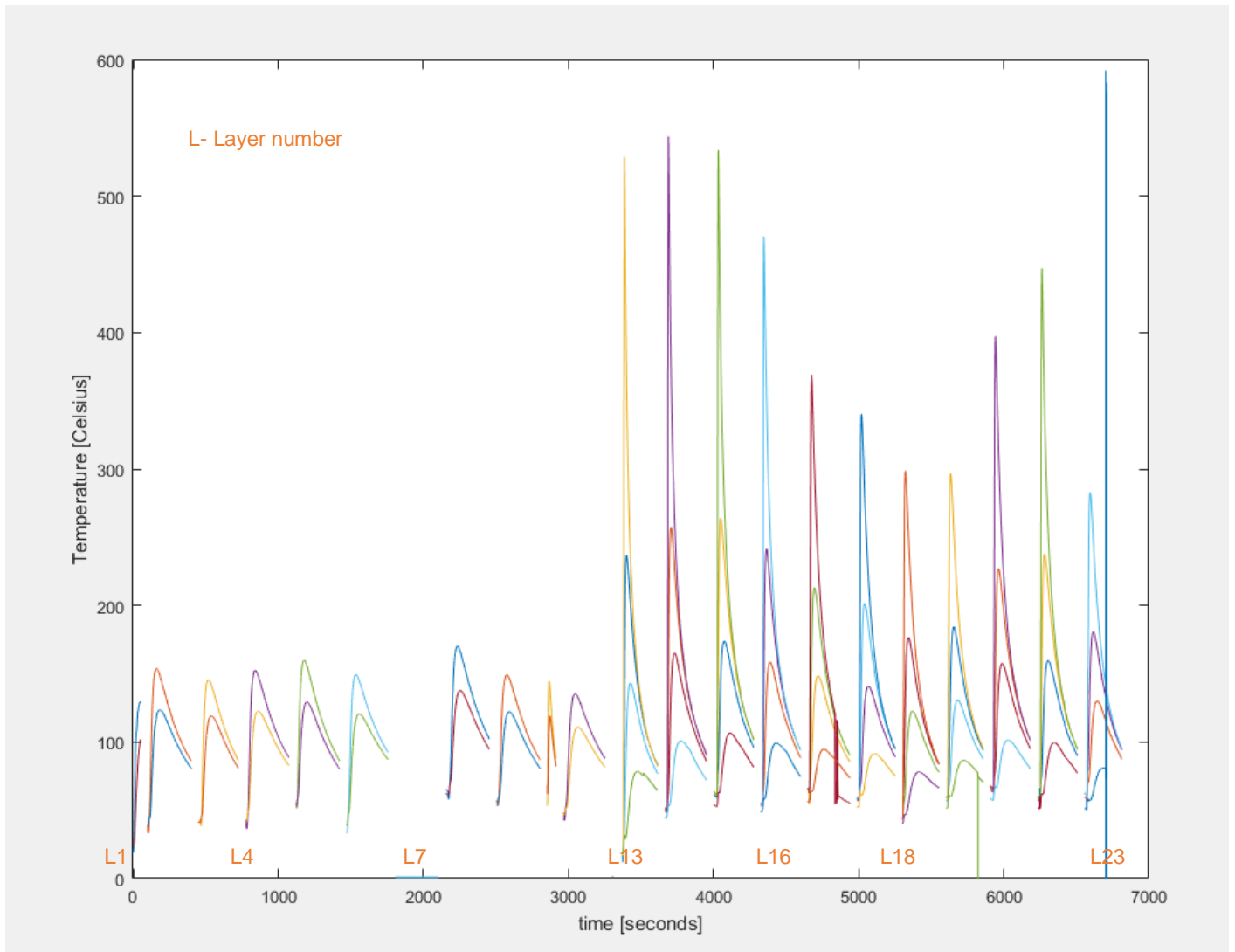


Figure 31: Thermocouple data per Layer of Experiment A. Note Layer 7 has no data. For layer 1-12 only the lower two thermocouples recorded data

interpass temperature was not noted per layer. The temperature cycles can be seen in Figure 31. Note that the time between each cycle in the figure does not correspond to the hold time between the cycles. Furthermore, some thermocouples failed during the deposition process: the first 12 passes were welded with thermocouples positioned at the side of the plate. After the 12th layer the wall was cooled to room temperature and additional thermocouples were placed on the deposited material. Between the deposition of layer 22 and 23 one of the thermocouples failed, which resulted in the faulty readings.

4.3.3. Chemical composition and Phases

The chemical composition of the built, measured by X-ray fluorescence can be found in

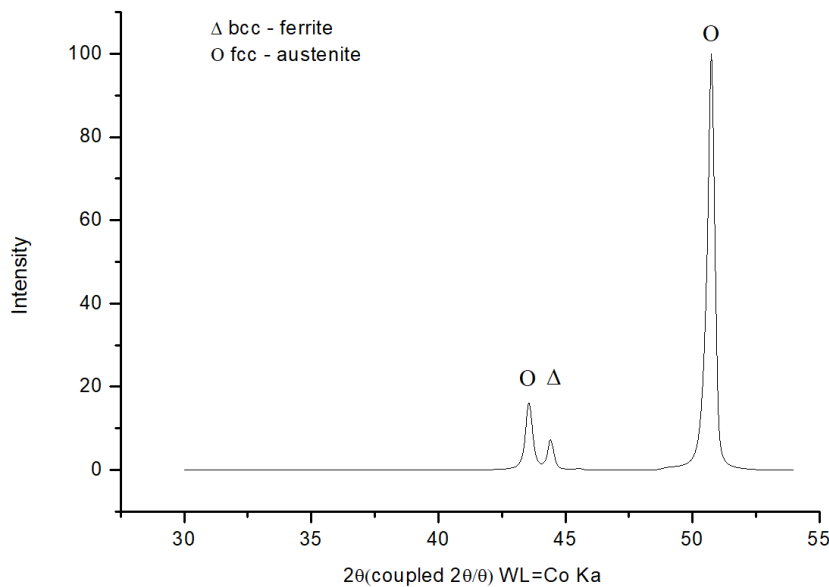


Figure 32: XRD results of a transverse cross section of the wall of Experiment A, normalized to 100 counts. Characteristic peaks for the austenite and ferrite phase are indicated.

Table 9 and the phases found by X-ray diffraction are indicated in Figure 32. The X-ray diffraction pattern shows the presence of strong austenite peaks and a ferrite peak. All XRD results are normalized to a maximum of 100 counts.

Table 9 Chemical composition in wt. % of XRF results

| | Fe | Cr | Ni | Mo | Si | Mn | Cu | Ta | Al | V | P | Pb |
|-------|--------|--------|--------|-------|-------|------|-------|-------|-------|-------|-------|-------|
| Exp A | 64.877 | 17.989 | 11.779 | 2.494 | 0.818 | 1.57 | 0.234 | 0.083 | 0.014 | 0.064 | 0.047 | 0.032 |

4.3.4. Macrostructure and Microstructure

Figure 33 (left) depicts the etched macrostructure of the transverse cross-section of Experiment A. The etch reveals the long columnar grains in the wall, which span through multiple deposited layers. Indications of the layer-by-layer building process are most pronounced at the sides of the cross-section by the white etched lines. Note that the centres of the passes are slightly shifted relative to each other, this is the case for the first deposited layers. Passes are next to each other/partly overlapping. Some of these welds are almost completely remelted by the deposition of a next layer.

In Figure 34 a dendritic structure with white stem and a brownish interdendritic region is depicted. Just above the fusion line delta ferrite is found, spanning throughout the cross-

section. However, the size and shape of the dendritic ferrite changes, depending on the location in the built. At the transition from HAZ to the fusion one, the morphology changes from no ferrite present to a cellular morphology, (indicating the high temperature gradient G_L and a lower interface growth rate R during solidification around the fusion line). Further up in the wall the morphology changes to a cellular dendritic morphology. Then the cellular dendrites change into columnar dendrites, which is the main morphology for the rest of the structure.

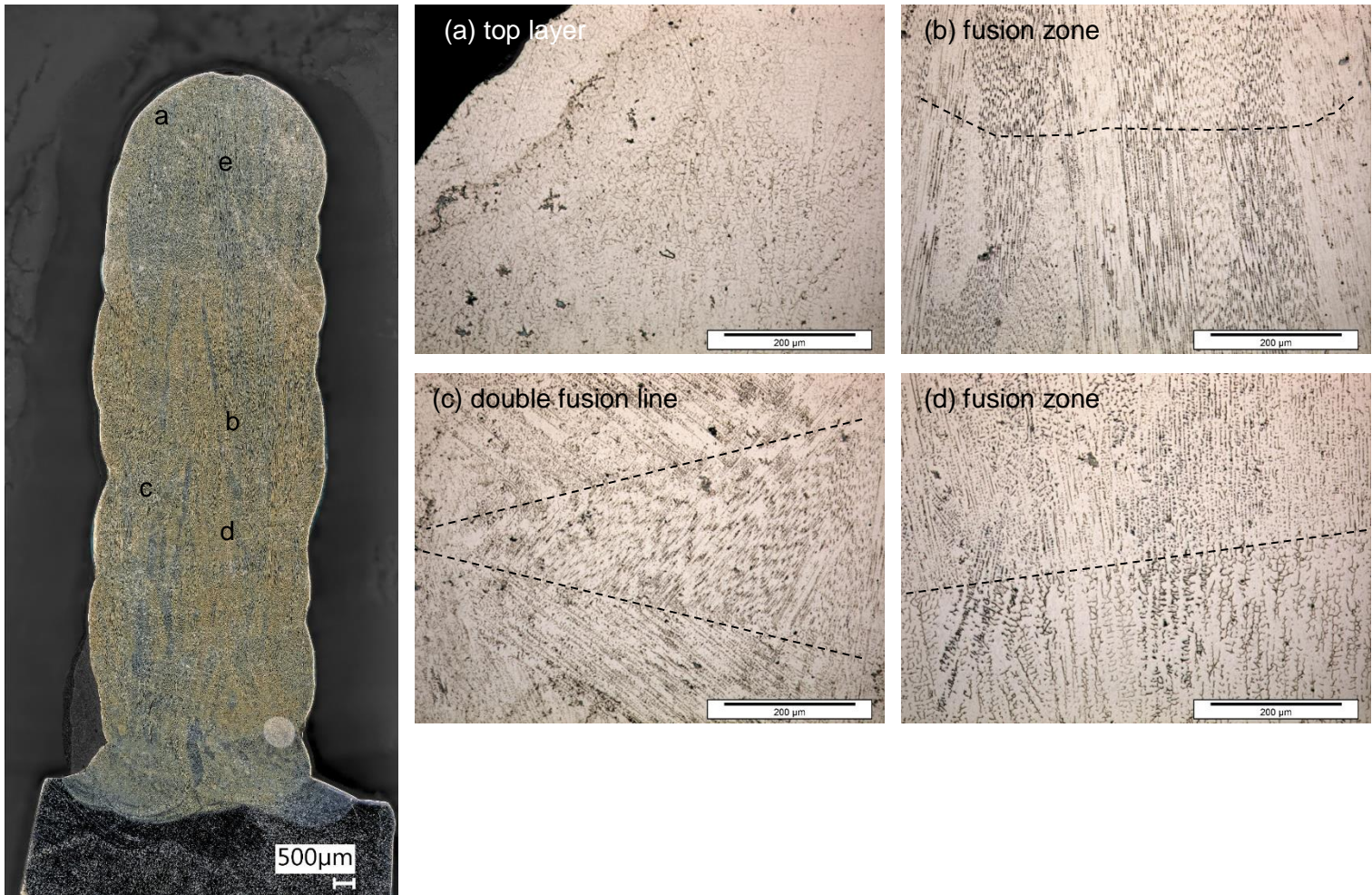


Figure 33: Transverse cross-section of Experiment A. Electro chemically etched using diluted NaOH. Columnar grain structure and layer structure is visible. (left) Macrostructure; (a) top layer - with equiaxed dendrites (b) fusion zone, dendrite direction continuous over fusion boundary (c) direction of dendrites change direction above fusion line (d) dendrite direction continuous over the fusion boundary

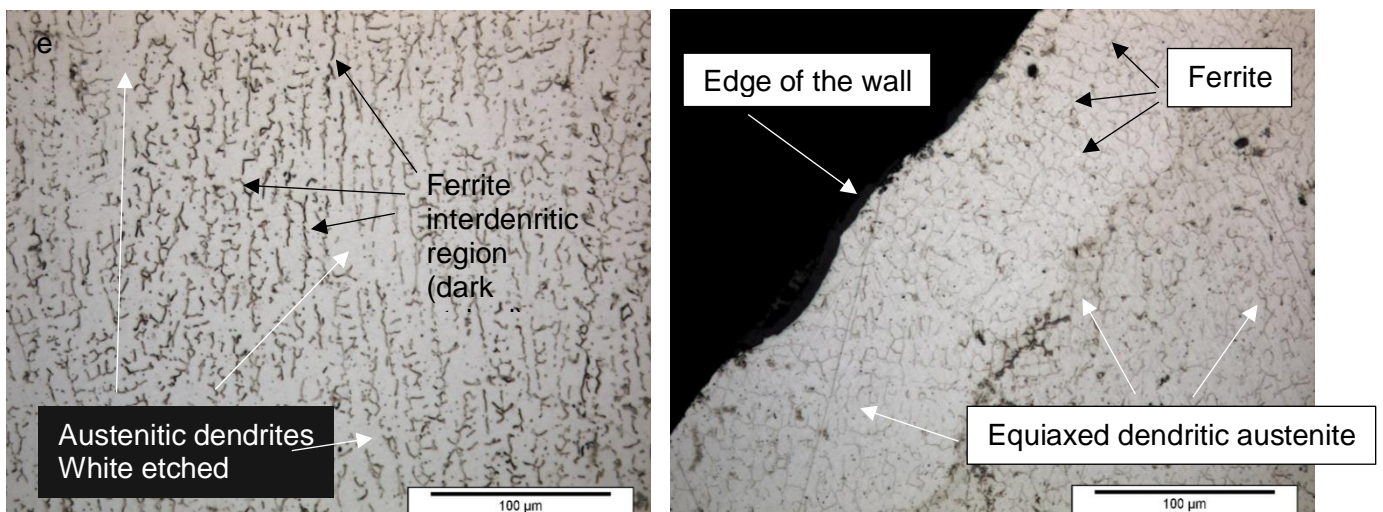


Figure 34: (left) Austenitic columnar dendrites and interdenritic ferrite (right) Micrograph (a) at a higher magnification: equiaxed dendrites are detected near the edge of the structure

4.4. Experiment B

In this section the results related to Experiment B are given. The welding conditions used are listed in Table 6. A double wire feeding system combining the feeding of an austenitic and a ferritic wire was applied. This experiment was intended as a preparation for Experiment C. Therefore, no temperature measurements were performed during the welding of this structure. The results of the chemical analysis by X-ray fluorescence and phase characterisation by X-ray diffraction are included.

4.4.1. Appearance and dimension

The 10-layer high structure, which was welded on the face of a 100 x 80 x 10 mm³ plate. The structure was welded, without changing the welding direction (no zig-zag pattern). The final walls height was between 8.9 mm and 10.9 mm. The length at the bottom was 84.9 mm and 79.6 mm at the top. The thickness varied between 5.9 mm and 7.9 mm. Figure 35 shows two pictures of the final built (the larger structure). The wall created was not entirely straight and it is higher at the starting side of welding. However, even though less attention was paid to appearance of the structure during welding, the overall built has an appropriate appearance.

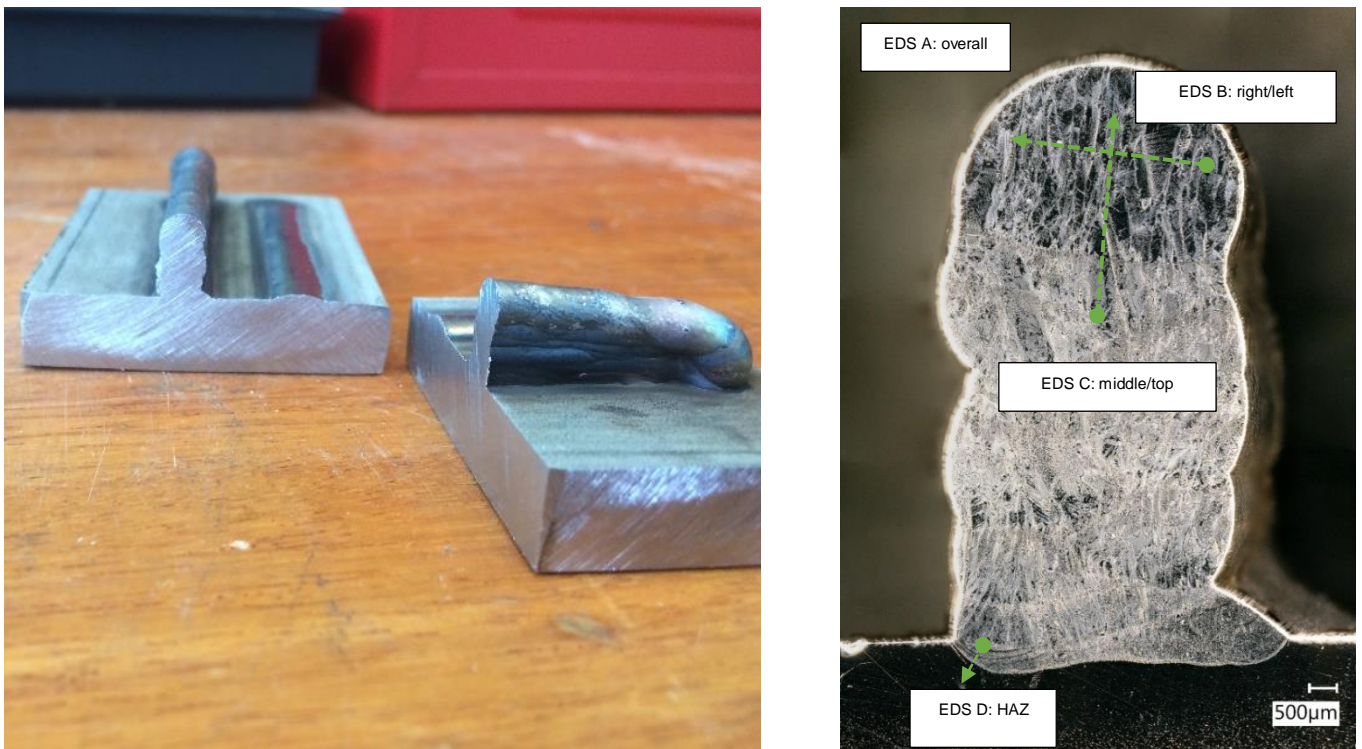


Figure 35: (left) Welded Structure AISI316L and AISI430L in same percentage, the built that is discussed is the larger structure on the photographs. As an indication of the scale, the plate thickness is 10 mm. (right) Macrograph of the etched transverse cross section and indication of the local EDS measurements

4.4.2. Chemical composition and Phases

The overall chemical composition of a transverse cross section of Experiment B obtained by using XRF and can be found in Table 10. The overall nickel content of 5.8 wt.% is lower than the average Ni values for both welding wires, *i.e.* (AISI316L + AISI430L)/2=6.4 wt. %Ni. The local chemical composition of the structure was measured by EDS. Figure 35 indicates the locations of the measurements and the tables presenting the results. Please note the distinct decrease in nickel content from the fully austenitic HAZ to the mixed fusion zone (FZ). X-ray

diffraction was applied for austenite and ferrite phase identification on the transverse section depicted in Figure 35 (b). The result of the measurement is found in Figure 32.

Table 10: Chemical Composition in wt. % for Experiment B. denotation A. overall composition. using XRF

| | Fe | Cr | Ni | Mo | Si | Mn | Cu | Al | V | P | Nb |
|-------------------|--------|--------|-------|-------|-------|-------|-------|-------|-------|-------|-------|
| Transverse | 73.557 | 17.121 | 5.835 | 1.197 | 0.599 | 1.276 | 0.161 | 0.014 | 0.092 | 0.032 | 0.116 |

Table 11: EDS scan across top. indicated by B [chemical composition in wt. %]

| | Fe | Si | S | Cr | Ni | Mo |
|------------------|-------|------|------|-------|------|------|
| 001 | 72.14 | 0.60 | | 20.93 | 6.33 | |
| --- | 72.88 | 0.69 | | 20.52 | 5.91 | |
| --- | 72.47 | 0.69 | 0.49 | 20.00 | 6.34 | |
| --- | 71.96 | 0.78 | | 19.42 | 6.28 | 1.56 |
| Average | 72.36 | 0.69 | 0.49 | 20.22 | 6.22 | 1.56 |
| Deviation | 0.40 | 0.07 | 0.00 | 0.65 | 0.21 | 0.00 |

Table 12 C: EDS scan from middle of the section to the top. indicated by letter C [chemical composition in wt. %]

| | Fe | Si | S | Cr | Ni |
|------------------|-------|------|------|-------|------|
| 001 | 71.70 | 0.73 | 0.39 | 19.98 | 7.20 |
| --- | 72.19 | 0.68 | | 20.08 | 7.05 |
| --- | 71.92 | 0.64 | 0.44 | 20.10 | 6.90 |
| --- | 72.49 | 0.70 | | 20.36 | 6.45 |
| --- | 71.70 | 0.65 | 0.48 | 19.91 | 7.25 |
| --- | 72.17 | 0.63 | 0.33 | 20.26 | 6.61 |
| Average | 72.03 | 0.67 | 0.41 | 20.12 | 6.91 |
| Deviation | 0.31 | 0.04 | 0.06 | 0.17 | 0.33 |

Table 13 EDS scan across the heat affected zone (HAZ). indicated by letter D [chemical composition in wt. %]

| | Fe | C | Si | S | Cr | Ni | Mo | |
|------------------|-------|---|------|------|------|-------|-------|------|
| 001 | 72.75 | | | 0.72 | | 19.9 | 6.64 | |
| --- | 72.14 | | | 0.52 | | 19.33 | 8.01 | |
| --- | 70.66 | | 2.42 | 0.63 | | 19.67 | 6.62 | |
| --- | 72.34 | | | 0.52 | 0.34 | 19.37 | 7.43 | |
| --- | 72.26 | | | 0.49 | | 19.54 | 7.72 | |
| --- | 69.5 | | | 0.43 | 0.63 | 20.54 | 8.9 | |
| --- | 68.89 | | | 0.49 | 0.34 | 19.17 | 9.43 | 1.69 |
| --- | 69.82 | | | 0.35 | 0.57 | 19.23 | 10.03 | |
| Average | 71.04 | | 2.42 | 0.52 | 0.47 | 19.59 | 8.1 | 1.69 |
| Deviation | 1.51 | | 0 | 0.11 | 0.15 | 0.45 | 1.26 | 0 |

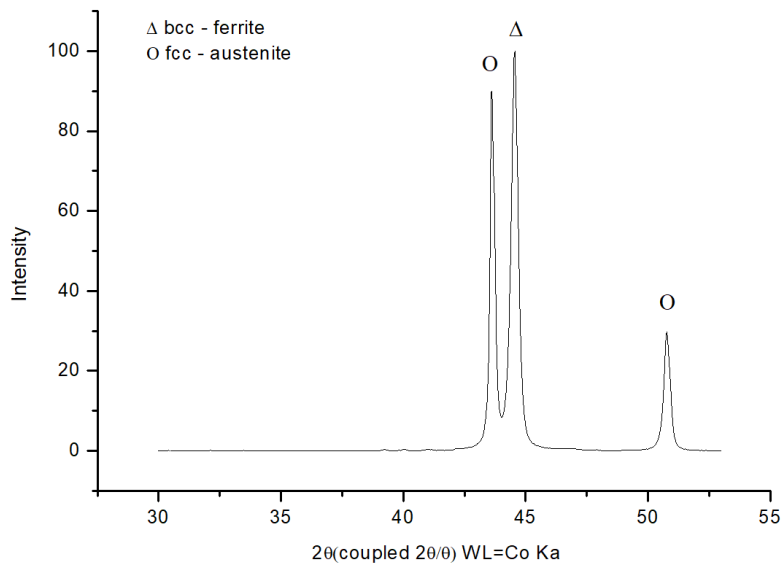


Figure 36: XRD results of the transverse cross-section of Experiment B

4.4.3. Macrostructure and Microstructure

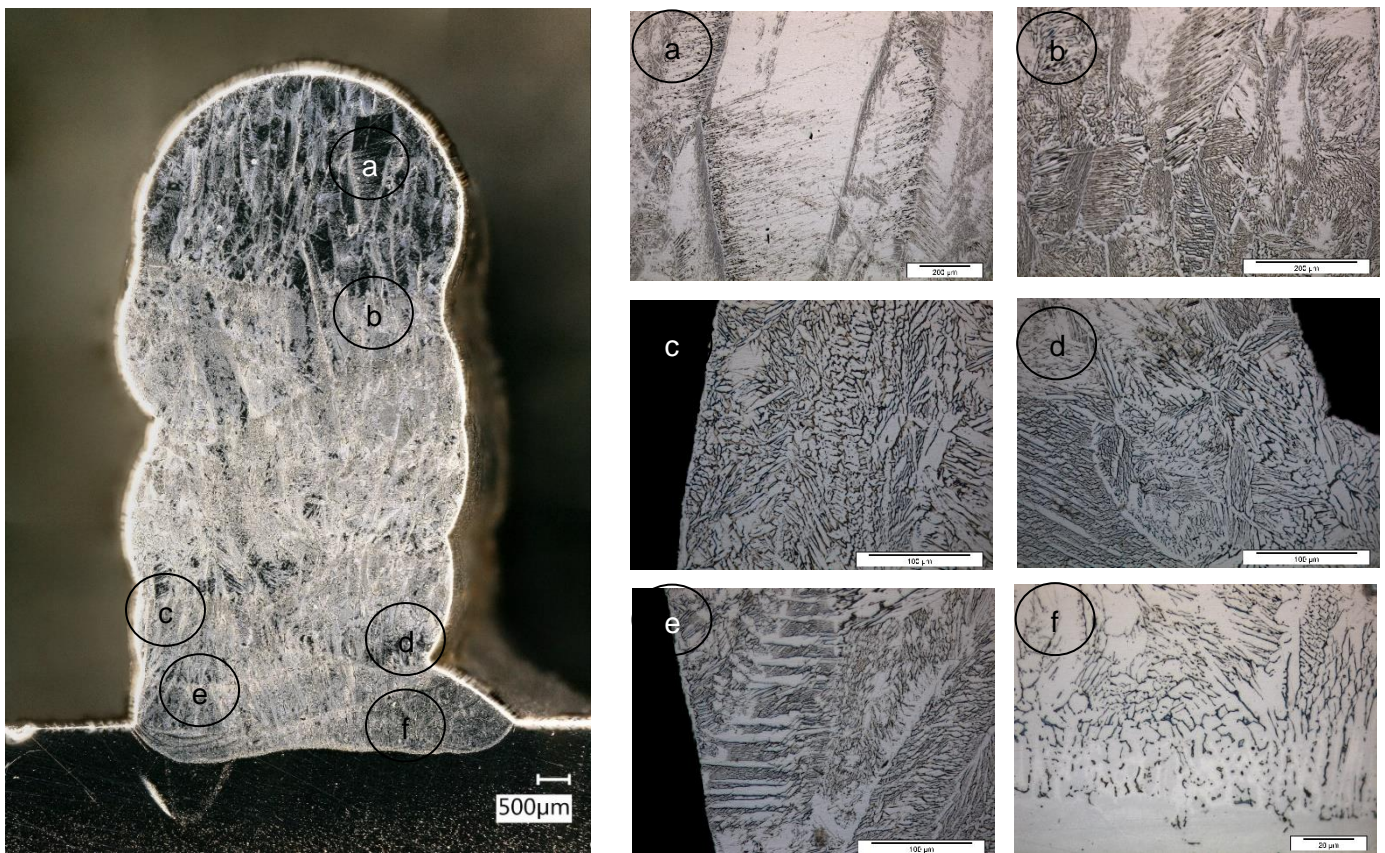


Figure 37: (left) Macrostructure and (right) Microstructure of structure B, location indicated on the macrograph

Figure 37 provides an overview of the macrostructure of the transverse cross-section of experiment B and several micrographs at indicated locations. The sample was electro-chemically etched using diluted NaOH and reveals the layered structure in the macrograph.

Note the darker etch of the last layer. Ferrite and austenite are found throughout the whole built, starting from the fusion zone, see Figure 37 a-f. Ferrite is dark etched, and austenite is white etched. The morphology of the ferrite and austenite changes throughout the structure. In the heat affected zone (HAZ, Figure 37 f), a cellular austenite structure is observed. In Figure 37 b-e and Figure 38 primary ferrite grains with Widmanstätten austenite is depicted. In the top layer, ferrite is situated at the grain boundaries and as acicular plates in the austenitized grain.

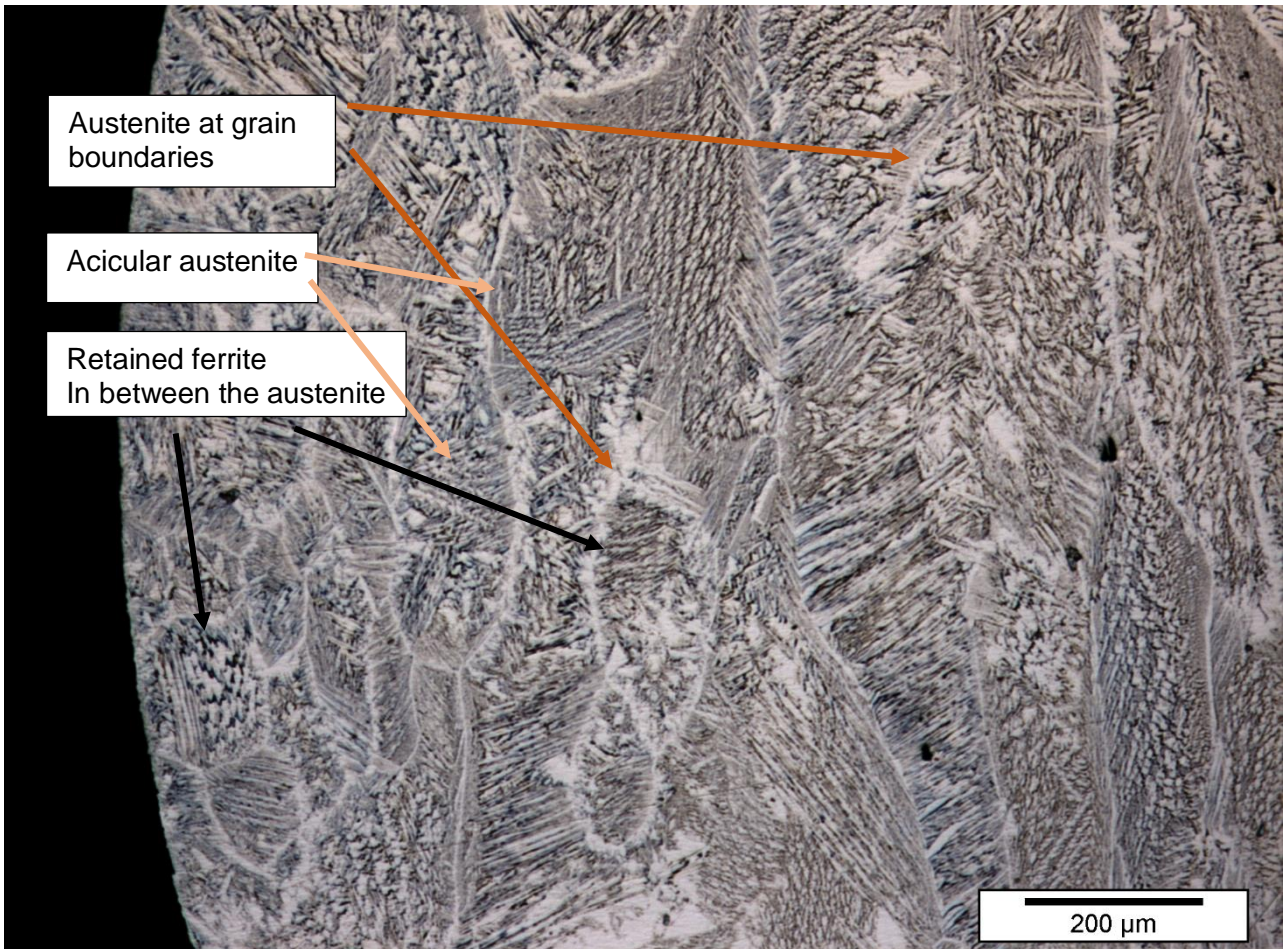


Figure 39: Experiment B morphology due to the $L \rightarrow L + F \rightarrow F \rightarrow A + F$ phase transformation.

4.5. Experiment C

In this section the results for the graded structure are presented. In this built the feeding rates of the austenitic and ferritic wire were gradually changed to realise a chemically graded wall. The overall deposition rate was kept constant. First, the as-welded structure is given. Subsequently temperature measurements data is provided. This is followed by the results on chemical composition, phases present and macro- and microstructure.



Figure 40: Welded AISI 316L/AISI 430L graded structure

4.5.1. Appearance and dimension

The as-welded structure is a solid stainless-steel wall of approximately $180 \times 23 \times 8 \text{ mm}^3$, which was welded on the side face of a $200 \times 80 \times 10 \text{ mm}^3$ AISI 316 stainless steel plate. The top of the structure is slightly curved, and the edges are irregular. The side surface of the wall consists of multiple distinct parallel layers, the layers thicknesses increase and decrease throughout the length of the wall and the layers are thicker and slightly higher towards the edge of the built. The final wall height was between 24.8 mm and 32.3 mm. The length at the bottom was 198.9 mm and 182.6 mm at the top. The thickness varied between 5.1 mm and 7.0 mm. There is no visual distortion of neither the wall nor the substrate. No cracks, pores or voids were found by visual inspection. The colour of the wall is a brown-grey, linked to oxide formation during welding. These colours are also found on the substrate's top edge.

4.5.2. Temperature

The temperature data measured during the building of the wall are plotted against time in Figure 41. Note that between layer number 6-7 and layer number 22-23 there is an overall temperature drop compared to the previous deposition. As the wall was built, the weld was deposited further away from the thermocouple, leading to inaccuracy of the interpass temperature reading. This can be seen when the thermocouple data is plotted next to each other. The maximum reading decreases each cycle.

See Table 14 for an overview of the maximum temperature, start temperature and estimated distance between deposition and thermocouple. The data is received for the upper welded thermocouple.

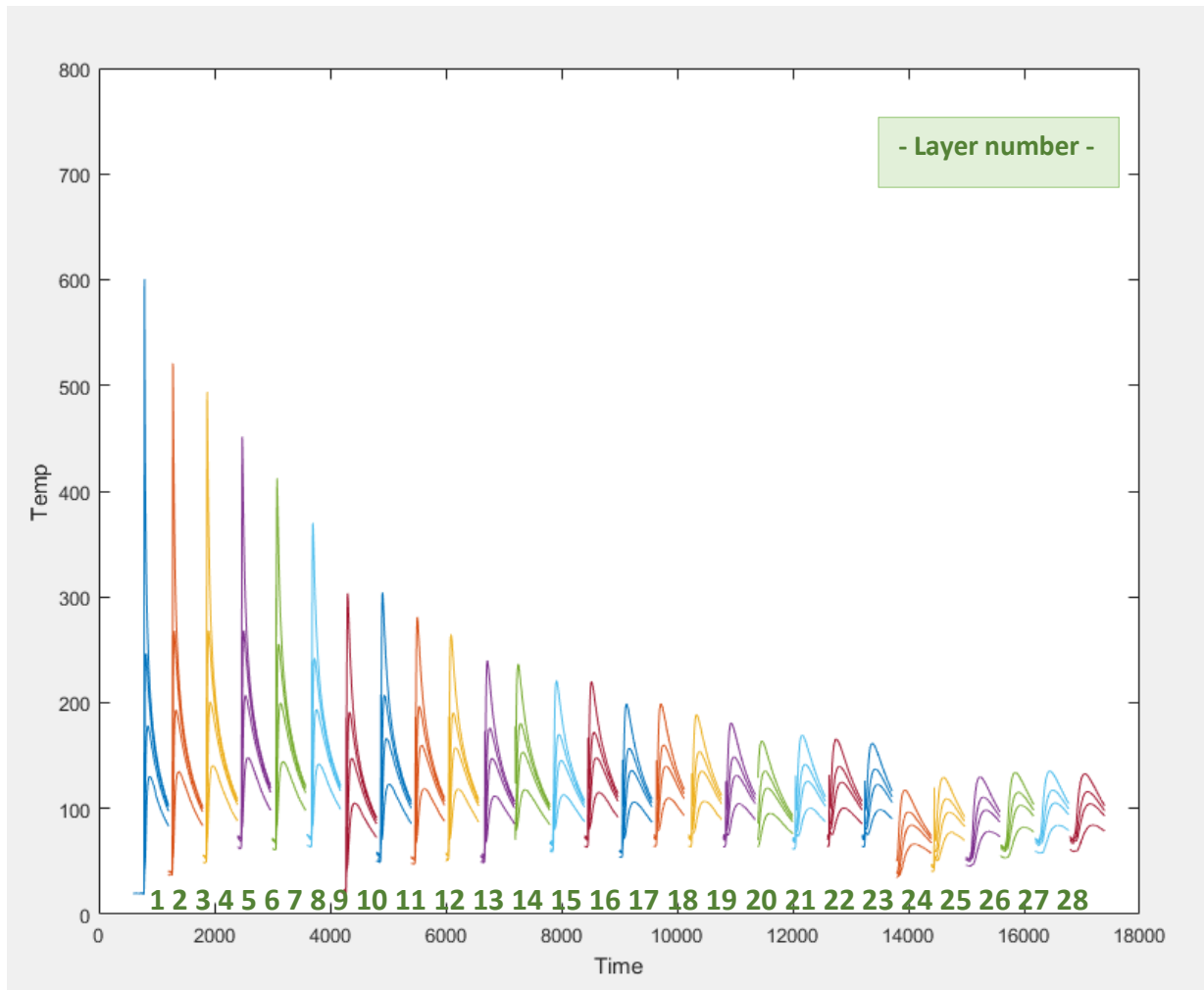


Figure 41: - Temperature measured by 4 thermocouples plotted per layer. The time between the layers is random and not corresponding to the actual time in between each the deposition of each layer.

Table 14: Overview maximum temperature

| Layer number | Approximate distance thermocouple to melt [mm] | Start Temperature [C] | Maximum Temperature [C] |
|--------------|--|-----------------------|-------------------------|
| 1 | 5 | 19 | 600 |
| 2 | 6 | 42 | 520 |
| 3 | 7 | 57 | 493 |
| 4 | 8 | 75 | 451 |
| 5 | 9 | 75 | 412 |
| 6 | 10 | 75 | 369 |
| 7 | 11 | 20 | 303 |
| 8 | 12 | 60 | 304 |
| 9 | 13 | 55 | 281 |
| 10 | 14 | 66 | 264 |
| 11 | 15 | 55 | 239 |
| 12 | 16 | 75 | 236 |
| 13 | 17 | 72 | 220 |
| 14 | 18 | 75 | 220 |
| 15 | 19 | 60 | 198 |
| 16 | 20 | 75 | 199 |
| 17 | 21 | 75 | 188 |

| | | | |
|----|----|----|-----|
| 18 | 22 | 75 | 180 |
| 19 | 23 | 60 | 163 |
| 20 | 24 | 73 | 169 |
| 21 | 25 | 75 | 165 |
| 22 | 26 | 75 | 161 |
| 23 | 27 | 20 | 117 |
| 24 | 28 | 50 | 129 |
| 25 | 29 | 55 | 129 |
| 26 | 30 | 65 | 134 |
| 27 | 31 | 72 | 135 |
| 28 | 32 | 75 | 133 |

4.5.3. Chemical composition and Phases

Shown in Table 15 are the average wt.% values of Cr, Ni and Mo taken from the normal cross sections of the structure. They were measured by X-ray fluorescence. These same cross sections were used to find the phases, which has been measured by X-ray diffraction are indicated in Figure 42. Note that there is no sigma-phase found in any of these patterns. In the cross-sections a and b there is no austenite found, referring to a very low percentage or non-austenite present. C-h are combinations of fcc and bcc peaks, indicating a mixture of both phases. From c to h the peak height of austenite increases, indicating a higher fraction austenite in lower taken normal section (nearer to substrate).

In contrast, in Figure 43 the chemical composition in wt. % for Cr, Ni, Mo and Mn is depicted measured by EDS on the transverse cross section of the wall. Note the difference in

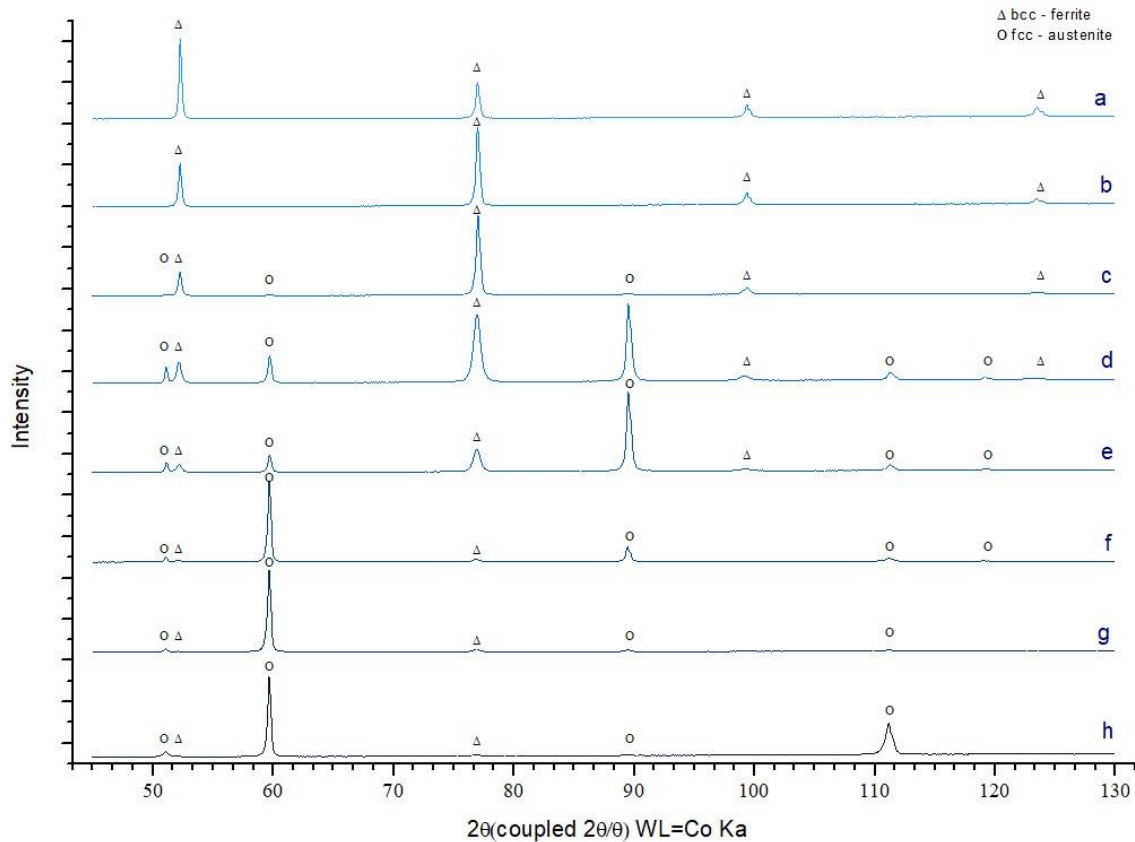


Figure 42: XRD results on different normal sections of the gradient. The letters indicate the location where the normal section was made (indicated in the macrostructure in section 4.5.4.)

Chromium content measured by EDS and XRF. Both methods show the decrease of nickel content towards the top of the structure.

Table 15: XRF data from normal cross sections. The letters indicate the location where the normal section was made (indicated in the macrostructure in section 4.5.4.)

| Sample | Cr [wt.%] | Ni [wt.%] | Mo [wt.%] |
|--------|-----------|-----------|-----------|
| a | 16.287 | 0.108 | 0.041 |
| b | 16.565 | 1.999 | 0.425 |
| c | 16.474 | 3.541 | 0.78 |
| d | 17.46 | 6.763 | 1.329 |
| e | 17.564 | 7.34 | 1.468 |
| f | 18.186 | 9.719 | 2.005 |
| g | 17.469 | 11.117 | 2.084 |
| h | 18.113 | 12.241 | 2.452 |

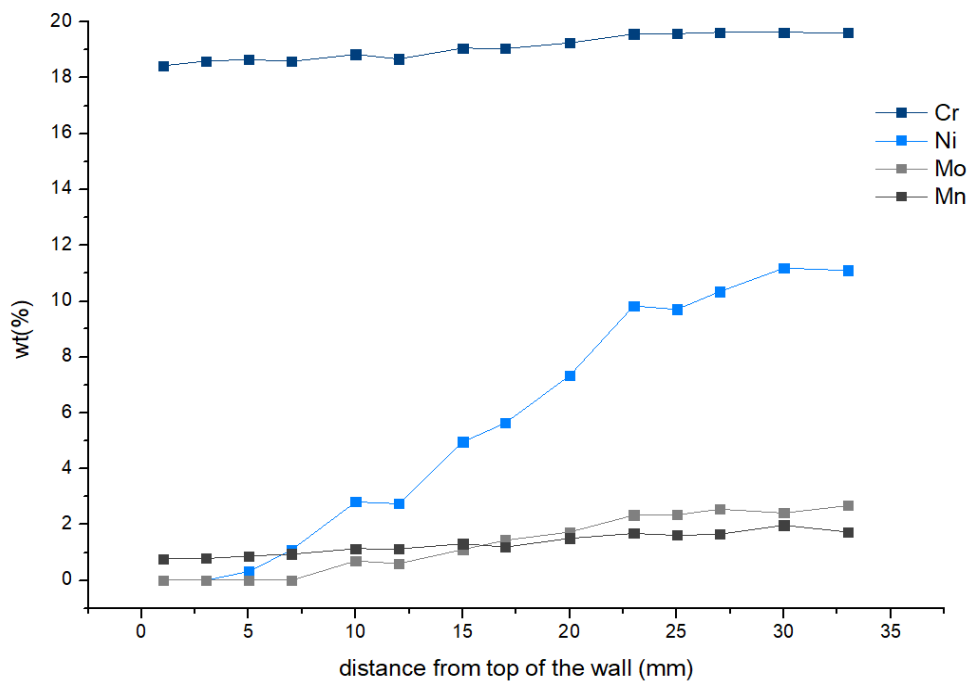


Figure 43: Composition due to EDS measurements. acceleration Voltage 20.00 kV, dead time around 14%, Count Rate: 6764.00

4.5.4. Macrostructure and Microstructure

See Figure 44 for the etched transverse cross sections of the built. Figure a is etched using diluted NaOH, however this revealed only the lower part of the built, as this region the austenite rich phase. Therefore, another transverse cross section of the built was etched by using Viella's solution, which revealed the layered structure of the ferrite-rich top part. The microstructure is briefly described under the figure and discussed in section 5.4.

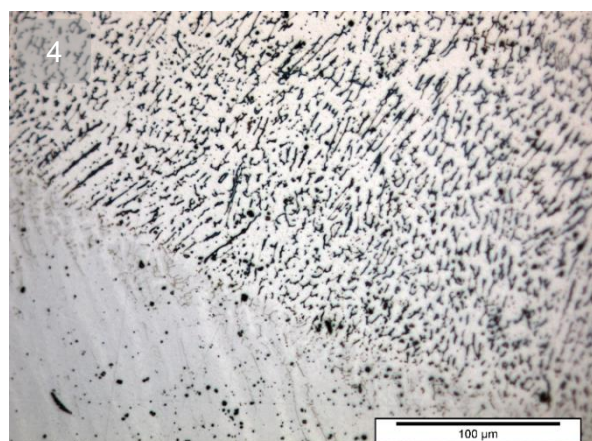
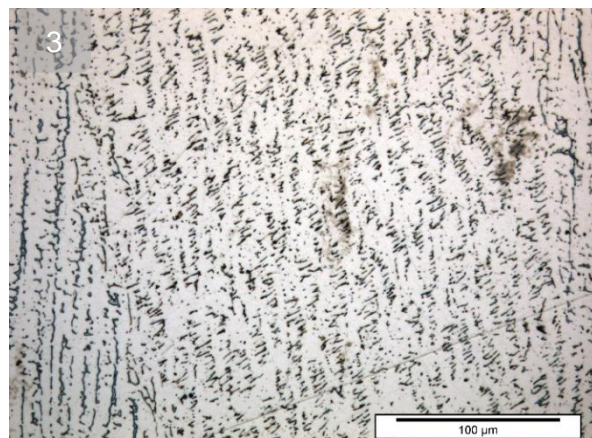
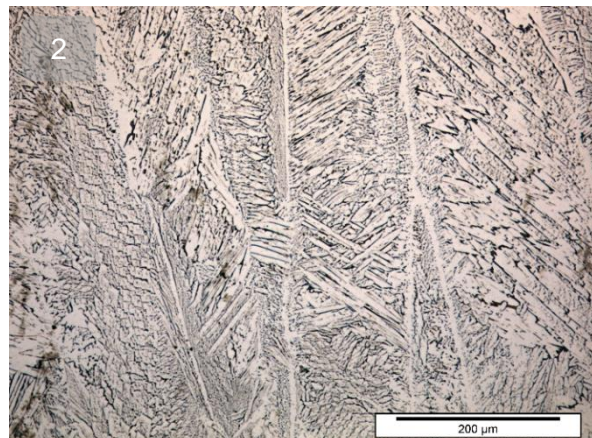
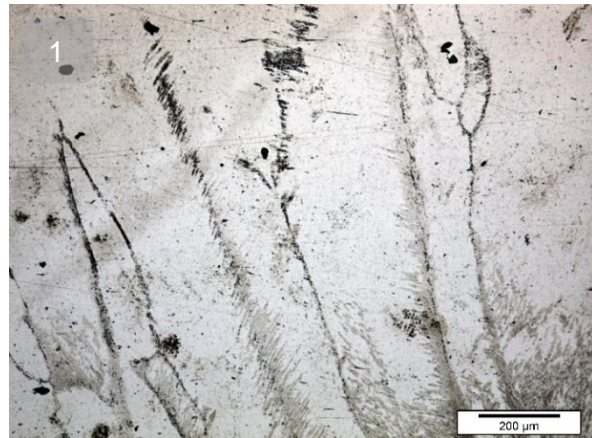
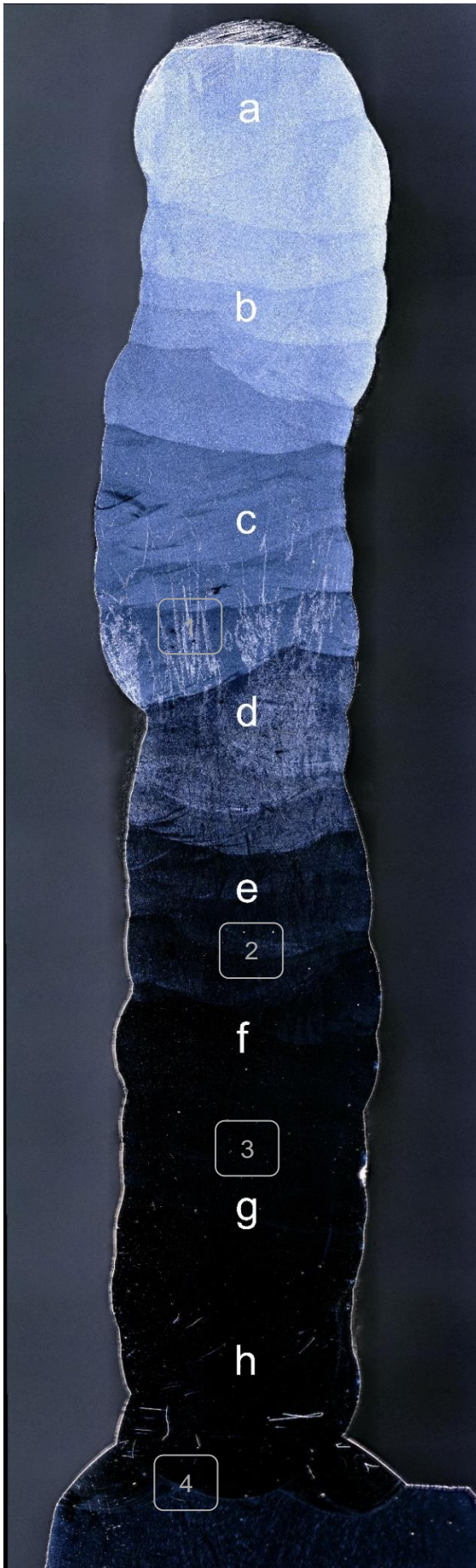


Figure 44: Cross section Experiment C: graded AISI316L and AISI430Lan AISI316 plate steel. (left) macro transverse cross section. Numbers refer to micrographs on the right, letters to XRD and XRF normal sections. (right) microstructures at different places of the transverse cross section (1-4). (1) Ferrite grains and grain boundary austenite (2) Widmanstätten austenite in ferrite grain (3) lathy ferrite in austenite matrix (4) austenite dendrites and intergranular ferrite

4.6. Heat treatments

In this section the results of the annealing/reheating of the welded structures are given. The details on the heat treatments can be found in section 3.7.4. The results of the microstructure evaluations including phase characterisation by X-ray diffraction are summarized in

Table 16, the peak-intensity curve for as-welded and heat treated structure is given in Figure 45, only the results for Wall A are depicted. In Figure 45 the microstructure after heat treatment is depicted. Note that in the graded sample, the amount of sigma phase formation

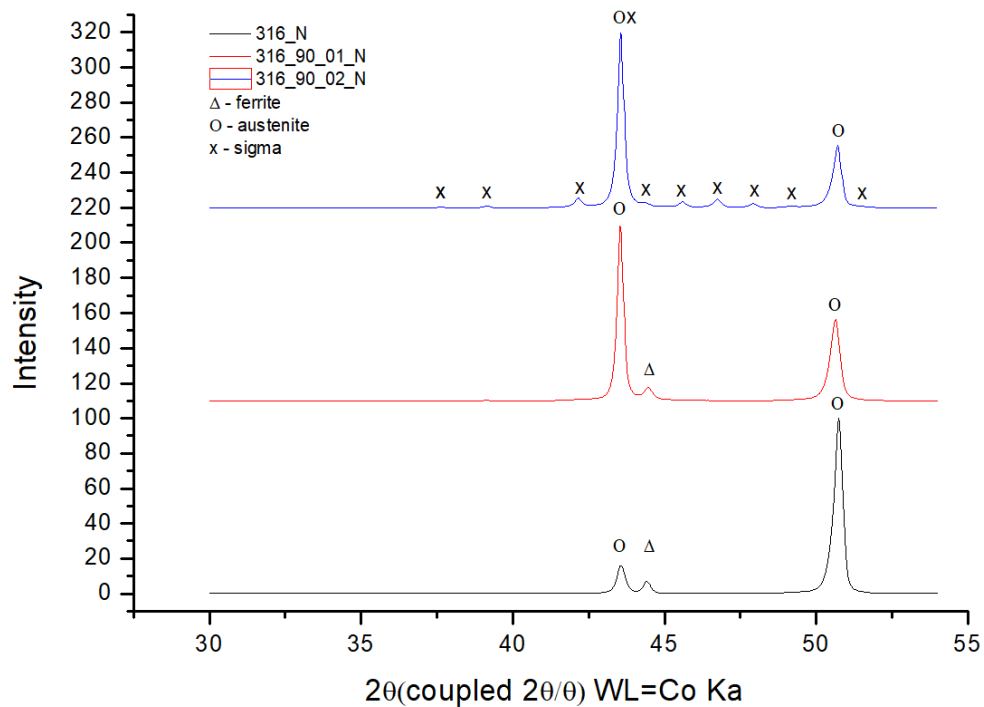


Figure 45: Experiment A: XRD results for the as-welded structure at the bottom, compared to heat treatment at 600°C above, change in peak intensity but no sigma phase detected and in blue the result for the heat treated sample, heat treated for 90 hours at 850°C, showing the distinct peaks identified as the sigma phase.

visibly decreased as a function of nickel content (less nickel, less sigma).

Table 16: Summary XRD results

| Sample | Phases | Note |
|---|---|---|
| Wall A as-welded | Austenite and Ferrite | No sigma phase detected |
| Wall A heat treated 90 hours at 600°C | Austenite and Ferrite | No sigma phase detected |
| Wall A heat treated 90 hours at 600°C + 90 hours at 850°C | Austenite and Sigma | Sigma phase consumed all ferrite |
| Wall B as-welded | Austenite and Ferrite | No sigma phase detected |
| Wall B heat treated 5 hours at 750 °C | Austenite and Ferrite | No sigma phase detected |
| Wall B heat treated 90 hours at 600 °C + 90 hours at 850°C | Austenite, Ferrite and sigma | Some ferrite was consumed by the sigma phase |
| Wall C as-welded | Austenite and Ferrite | No sigma phase detected |
| Wall C heat treated 90 hours at 600 °C + 90 hours at 850 °C | Austenite, Ferrite and sigma Only sigma phase in the first layers, then gradually less sigma phase | There was a decrease in sigma content from bottom to top on the transverse sample |

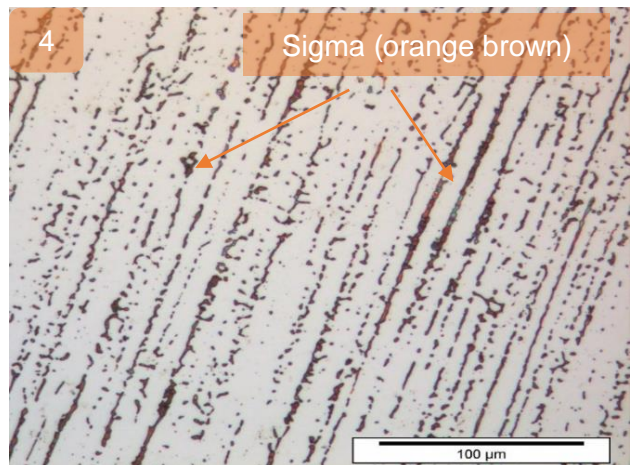
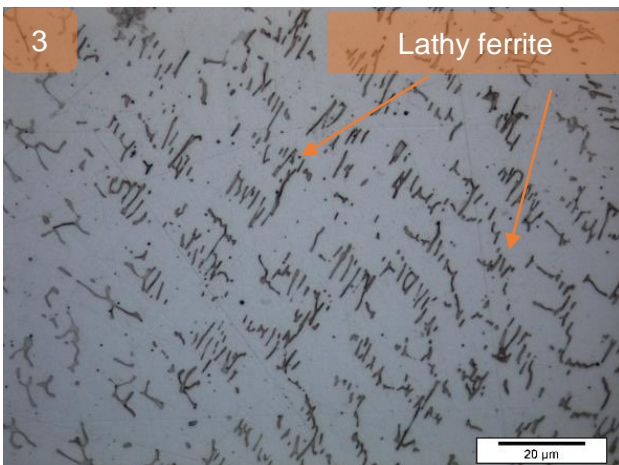
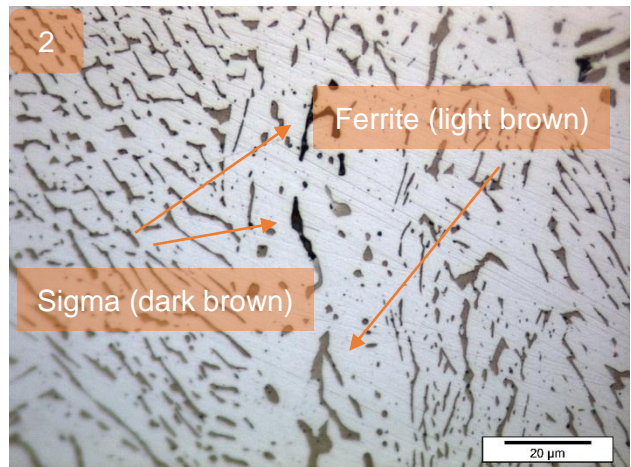
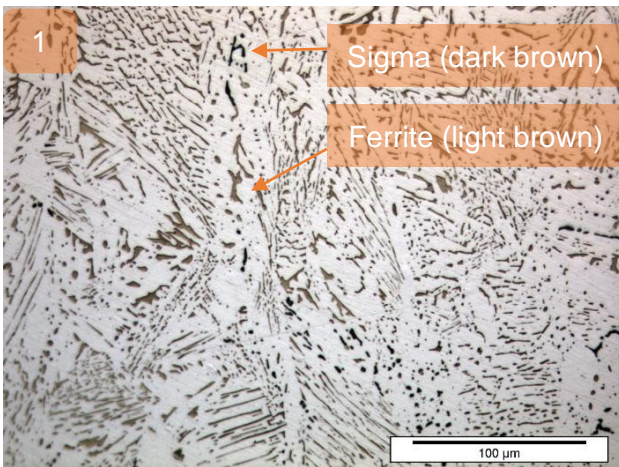


Figure 46: In all micrographs the austenite phase is white etched. (1) Wall B heat treated 90 hours at 600 °C + 90 hours at 850 °C – sigma formed from ferrite, ferrite not fully transformed. (2) Wall C heat treated 90 hours at 600 °C + 90 hours at 850 °C - sigma formed from ferrite, ferrite not fully transformed (3) Wall A as-welded – ferrite and austenite (4) Wall A heat treated 90 hours at 600 °C + 90 hours at 850 °C – sigma spheroids, full transformation from the ferrite.

5. Discussion

5.1. Introduction

This chapter reflects on the results of the recent study. As this study was of an experimental nature, a few critical remarks on the additive manufacturing setup are made as these have influenced the results of this study. The evolution of the microstructure is discussed for Additive Manufacturing based on the temperature measurements and the thermal cycles the material experienced during the building process. The observed morphology is linked to the solidification processes and solid state phase transformations the material described in chapter 2.

After analysing and discussing the as-welded microstructure, the discussion focusses on the formation of secondary phases in the material, both during welding and in use. In contrast to a single-weld deposition, the repetitive re-heating of the weld may lead to the formation of secondary phases. The temperature regime in which these phases may form are discussed in the subsequent section.

5.2. Experimental Setup and Welding Parameters

5.2.1. Effect of the wire feeder calibration error

In this study, two wire feeders were used. They separately controlled the rate at which the stainless steel wires were supplied during welding. Both wire feeders were manually controlled, using an on/off switch, at the start and end of the deposition of each layer. It was attempted to begin and end the wire supply simultaneously with the turning start and stop of the arc. Nevertheless, this manual operation lead to an uneven deposition at the start and end-points of each layer.

Additionally, for each experiment, the wire feed rate had to be manually regulated. The wire feed rate was measured using a stop watch and measuring tape. The setting was checked three times. As was seen in chapter 3.3, an error curve on the calibration of the wire feeder was made, to depict the error made by calibrating the wire feeder. Using these error estimate values, the standard deviation is calculated, to approximate the variation. The median error value is $l = 0.62 \text{ mm/s}$. The wire diameter is 1 mm and the density of the wire is 8031 kg/m^3 [32]. The error in mass deposition M_{error} can be calculated by

$$M_{error} = \pi r^2 l \rho_{wire} = 0.004 \text{ g/s} \quad (5.1)$$

The 4 milligrams per second for a layer length of 170 mm, and a welding speed of 5.5 mm/s, this amounts to 0.12 g material. In other words, mass input per layer may have 0.1 g per layer throughout the whole Experiment. This is a small amount, which, per layer will have a small effect on the total mass deposition and will also not significantly have influenced the AISI316L/AISI430L ratio in the graded structure.

5.2.2. Homogeneity of the layer height

In this study, one of the challenges during welding was the change in layer height, as briefly mentioned in section 4.1 and in the preliminary results (chapter 4). A solution to keep the layer height constant over the length of the wall, is to alternate the welding direction from layer to layer. In practise, this means that the vertical plate was turned 180 degrees after the deposition of each layer. Alternating welding direction was used for the building of wall A (Experiment A) with satisfactory results.

If the welding direction is not changed height differences occur. In Figure 47 an example of such a welded structure is given. The structure slopes down towards the end of the beads. To explain this behaviour, one must consider the heat transfer taking place during welding. Heat is transferred through conduction (through the wall and the plate), radiation and through convection (in the melt pool and atmosphere). From the geometry of the weld beads heat transfer through radiation and convection is higher at the edges of the wall while heat transfer through conduction is more dominant in the middle of the wall. During welding the wall and the plate heat up. At the start of welding, the wall is at its lowest temperature (approximately 75°C, see interpass temperature in the following section on heat cycles). At the end, the wall and the plate temperature has increased, and reduced cooling rate, heat accumulation at the end of the bead increases melt pool size. Due to the deposition of multiple layers in the same welding direction, this sloping effect increases. Therefore, an alternating welding direction is preferred to obtain an even deposition height.

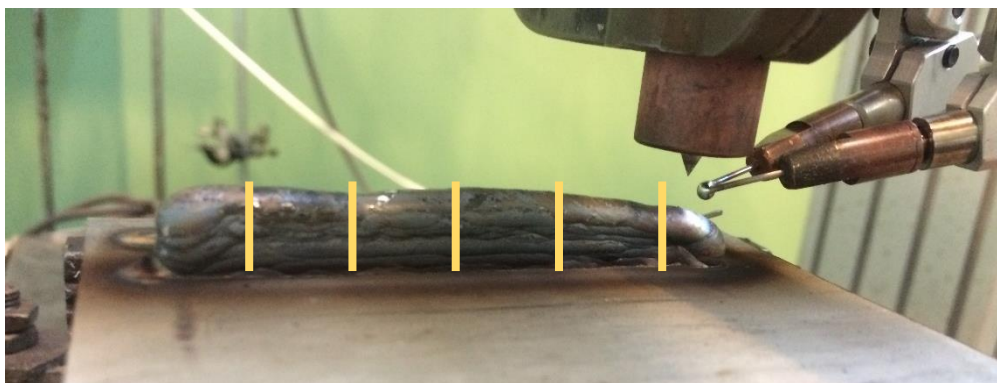


Figure 47: Sloping after deposition of a few weld beads

As mentioned above, alternating welding direction had a positive effect on the wall geometry. However during the execution of the experiments, the attached thermocouples malfunctioned repeatedly. The thermocouples were spot welded to the face of the plate, however this connection proved to be very fragile. The detachment of the thermocouples caused inaccurate readings and part of the data was not recorded for this Experiment. Due to this inconvenience, the turning of the vertical plate was omitted for Experiment B and C.

As expected, the walls started sloping after a few layers. This causes a problem for setting the arc length at the beginning of each layer. The welding torch was controlled by the CNC machine, and could not be readjusted during welding. To overcome this problem partial layers were deposited on lower sections of the wall, to decrease the inhomogeneity of the layers.

5.2.3. Inaccuracies of the wire feed holders

The wire feed holders used throughout all experiments consisted of many clamped parts that could be manipulated. This is very useful during calibration of the wire feed angle (horizontal angle and vertical angle), however, the smallest force on the holder would immediately turn the holders. For example: when the manually operated wire feeder was still on when the electric arc was switched off, the solid wire would bump into the solidified melt pool. This was enough force to turn the wire feeders, and therefore the holders had to be adjusted each cycle. If performed incorrectly, meaning the wire did not travel directly into the arc, the wire would 'overshoot', or be sticking out of the wall, thus not being molten by the heat source during welding. In general, this may have caused a few errors in composition,

especially for the graded structure, which showed multiple occasions of such overshooting of the wire.

5.2.4. Decreasing building time

In the fabrication of the walls, the interpass temperature was measured using the thermocouples welded to the structure. The interpass temperature was selected to be lower than 75°C. In other words, the next layer was not deposited before the highest measured temperature value dropped beneath 75°C. In practise, the cooling of the welded structure took around 10 minutes for each layer. As each layer is approximately 1 mm in height, the building rate is 1mm height per 10 minutes or 6 mm/hour. In view of the more fundamental approach of this study, the relatively large processing time is not an issue. For industrial applications the interpass time may be shortened.

5.2.5. Summary: Experimental Arrangements and Welding Parameters

- Errors in wire feed rate have only a small impact on the total mass deposition and likely not have impacted the actual AISI316I/AIS430L ratio on the graded structure.
- Due to the inhomogeneity of the deposition height, the actual arc length during deposition fluctuated.
- Inhomogeneity of the layer height can be minimised by either repairing the structure by depositing extra material or by alternating the welding direction.
- The building time of structures can be decreased by decreasing the interpass time.

5.3. Thermal cycling

During the building process the material underwent multiple thermal cycles, as a result of the layer by layer deposition. The heat cycles that the material went experienced, where measured by thermocouples as described in chapter 3 & 4. These are used to find the thermal history per layer. In this study, the thermal history for temperatures around 950-600°C are especially important, since this is the regime in which solid state transformations take place in the material. The temperature measurements for Experiment C are given in Figure 41. The graph depicts the thermal cycle per welded layer from left to right. With each deposited layer the distance from the weld pool/heat source to the location of the thermocouple increases, consequently the peak temperature decreases, which is shown in the graph: the peak temperature drops. Furthermore, the peak temperature decreases when the structure is cooled to room temperature, instead of maintaining an interpass temperature of 75°C (after layer 6 and 21). Thus, the peak temperature is influenced by the interpass temperature.

As mentioned above, the temperature regime of interest for solid state phase transformation is 950-600°C (Figure 8). However, as can be seen in the Figure 41, this temperature regime was not covered by the temperature measurements, the maximal temperature measured was 600°C. Therefore, a COMSOL heat model was created to simulate the temperature development in that range. The model was validated by the measurements. This heat model was then used to find

- the cooling rate between 950-600°C,
- peak temperature reached after each cycle and
- total time in the critical 950-600°C temperature regime per layer.

5.3.1. COMSOL heat model

A COMSOL finite element thermal model was created, as described in section 3.7.4. The material data for this model was extracted from *van der Aa* [32]. The input parameters were taken from Experiment C (welding over a length of 190 mm, travel speed 5.5 mm/s, 140 A

and 12 V). In total 7 layers of 1.1 mm were simulated. The temperature at fixed points, corresponding to the thermocouples location of Experiment C were extracted. The temperature data available from Experiment C, was used to validate the model. In Figure 48, the temperature development for the highest available measurement are given on the left and the corresponding heat response of the COMSOL model is given (right).

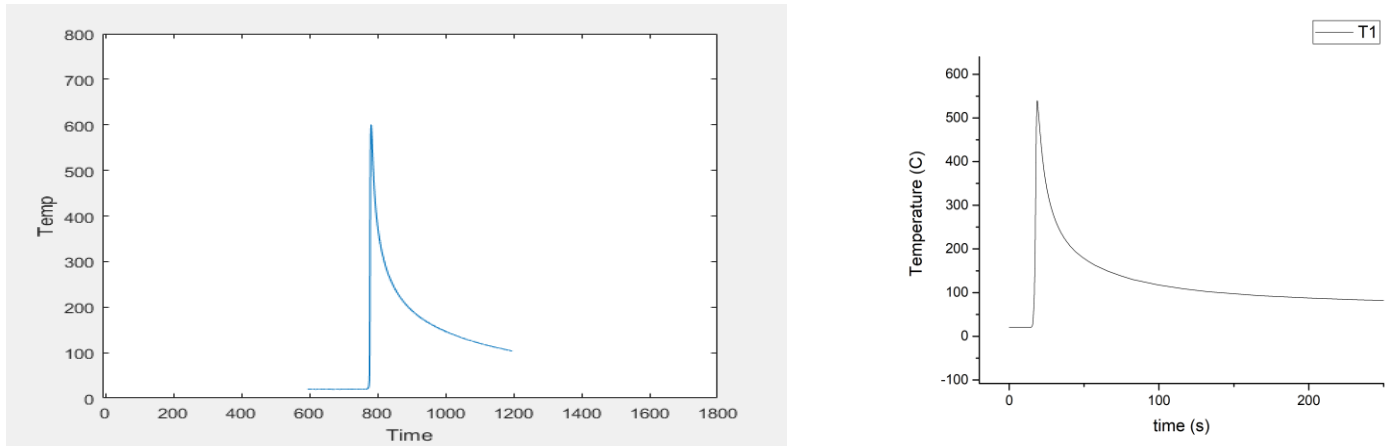


Figure 48: Heat and cooling cycle for the highest measured temperature. (left) as-measured (right) by the heat model

Immediately, the peak temperature of the model is approximately 60°C lower than the measured data and the modelled curve has a steeper temperature gradient than the experimentally obtained temperature data. This may be due the estimation of the thermal properties of the material, an error in the exact location of the thermocouples or by the assumption on heat transfer coefficient in the model. Small variation of the situation of the thermocouple placement greatly varies the recorded peak temperature.

Using the COMSOL model, the temperature development closer to the heat source was calculated, Figure 49. The reference point denoted as TA1 and TA2 are part of layer one and two. The figure depicts the temperature development for 7 layers, with an interpass time of 10 minutes. Figure 49 b (right) depicts the first and second thermal cycle.

5.3.2. Cooling rate

From this data the cooling rate can be calculated. Figure 50 depicts the time and temperature data for the newly calculated temperature development. From this the cooling rate can be calculated.

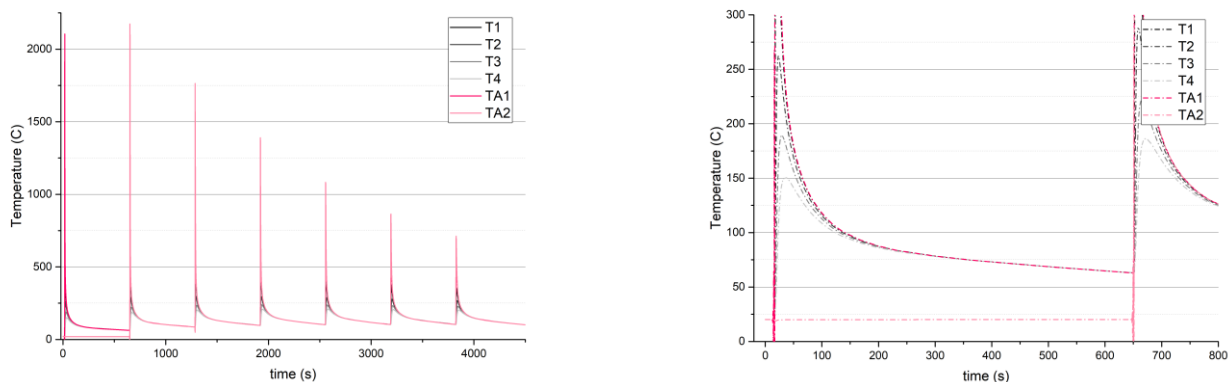


Figure 49: (left) T1-T4 corresponds to the thermocouples of Experiment C with distance equal to the Experimental setup. TA1 and TA2 are additional thermocouples 0.55 and 1.65 mm from the substrates, in the centre of the layer.

$$\text{Cooling Rate} \sim \frac{dT}{dt} = \frac{T_1 - T_2}{t_2 - t_1} \quad (5.1)$$

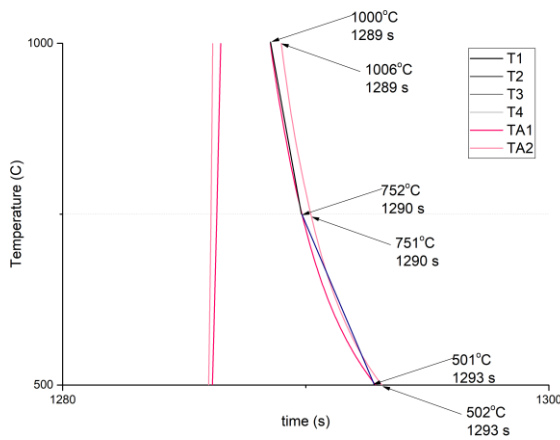


Figure 50: Second heat cycle for reference point 1 and 2 of the COMSOL heat model

Table 17 Cooling rate C1 and C2. Corresponding to TA1 and TA2 curves (second thermal cycle)

| | time 1 [s] | time 2 [s] | time 3 [s] | T 1 [°C] | T 2 [°C] | T 3 [°C] | C1 [°C/s] | C2 [°C/s] |
|-----|------------|------------|------------|----------|----------|----------|-----------|-----------|
| TA1 | 1288.5 | 1289.8 | 1292.9 | 1000.1 | 752.3 | 500.8 | 190.6 | 81.1 |
| TA2 | 1289 | 1290.3 | 1293.1 | 1005.791 | 751.2 | 501.6 | 195.8 | 89.1 |

The cooling rate for Figure 48a and b, between approximately 500-400°C, is:

$$a) \frac{dT}{dt} = \frac{499.9 - 400}{796.4 - 787} = 10.6 \text{ } ^\circ\text{C/s}$$

$$b) \frac{dT}{dt} = \frac{500.4 - 399.6}{22.5 - 19.82} = 37.6 \text{ } ^\circ\text{C/s}$$

As mentioned before, the cooling rate is completely dependent on the heat transfer coefficient applied in the model.

5.3.3. Summary: thermal cycling

From the temperature model and from the temperature measurements it can be taken that: The peak temperature per cycle decreases for a fixed reference point, due to the increase in distance to heat source. For a 1 mm layer height, the peak temperature per cycle gradually decreases. After 6 cycles (6 mm away from the melt pool), the reference point stays under 600°C.

- The simulated cooling rate was around 193 °C /s for the higher limit (1000-750°C), 85 °C /s for the temperature regime between 750-500°C.
- The measured cooling rate was 20°C/s lower than the simulated cooling rate at 500-400°C.
- Peak temperature is influenced by interpass temperature.

5.4. Phase morphology

In this section the macro- and microstructure of the printed walls will be discussed. These layers of the welded structure undergo multiple thermal cycles. The upper layer of the simplest structure is discussed first. The simplest structure is here the micro-structure of the first Experiment, Experiment A. For each of the designed experiments (A to C) the microstructure will be discussed. The observed morphology is linked to the known theories of solidification modes for stainless steels, mentioned in chapter 2. If possible, the solidification structures are linked and in the last section the mixing of the wires is discussed.

5.4.1. Experiment A

In Figure 51 the phase diagram of commercial AISI 316L stainless steel is depicted. The orange arrow in the figure notes the approximate nickel content of the structure. At 12.5 wt. % Ni the material will form austenite first than austenite and ferrite become both stable the phase development at high temperature for this alloy is thus $L \rightarrow L + A \rightarrow L + A + F \rightarrow A + F$.

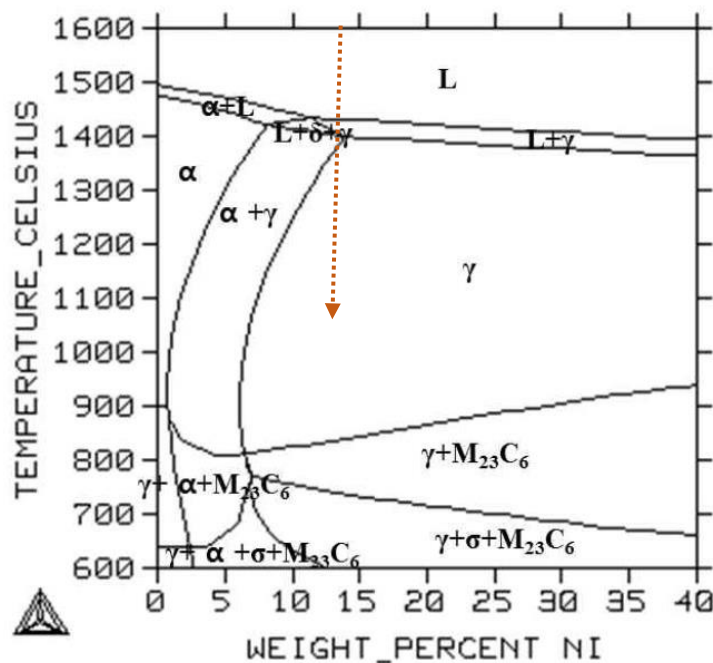


Figure 52: Phase diagram of commercial 316L stainless steel, plotted by using ThermoCalc; arrow indicates the approximate nickel content of the structure

Additionally, it was mentioned section 2.3.3. that in welding the often observed morphology is a dendritic structure which forms due to strong undercooling.

Depicted in Figure 34 (left) is the dendritic austenite morphology, with interdendritic dark-etched ferrite under the optical microscope. In Figure 34 (right) at the edge of the structure, the dendrites have no overall direction. They are labelled as equiaxed dendrites. These can be found along the edge of the top layer, except near the fusion boundary of the layer. The rest of the layer consists of directional dendrites: a combination of cellular and columnar dendrites is observed. They are framed by the ferritic phase, which formed between the austenitic dendrites.

Equiaxed dendrites form due at low thermal gradient and or large interface growth rate R . However, the interface velocity is directly proportional to the travel speed v and the cosinus of the angle they make.

$$R = v \cos(\theta) \quad (5.2)$$

The observed dendrites depicted in Figure 34 (right) must experience a low thermal gradient.

However, it must be considered that there was only one transverse cross section made. The possibility exists that these dendrites are directional, but in a different plane, then can be observed by this cross section.

In Figure 33 multiple fusion boundaries are depicted. It is shown, that the direction of the dendrites in some cases extent beyond the fusion boundary. It may be theorised that nucleate on the existing grains of the previously deposited layer occurred, leading to epitaxial growth. In Figure 33 (b) some of these grains stop growing due to competitive growth.

In section 2.4 it was mentioned that the product of interface growth rate and temperature gradient GR determines the size structure (large GR = fine structure, low GR = coarse structure). The temperature gradient between at the fusion zone is obviously very large, and slowly decreases during solidification. Depicted in Figure 33 (d) is the dendritic structure above and below the fusion zone. The dendrites just above the fusion line are fine structures. This is possibly due to the large temperature gradient.

The top layer of the welded structure did not undergo any further heat cycles. It is most like a single weld bead of AISI 316L stainless steel. As all previous layers are AISI 316L stainless steel, the composition of this layer is expected to be AISI 316L stainless steel. A comparison of the top layer and one of the layer fusion zones shows that the morphology of one of the middle layers shows larger dendrites compared to the top layer, indicating a possible heat effect on the heat affected layers.

In conclusion, the microstructure of the transverse section of the wall shows that: The overall structure consists of dendritic austenite with interdendritic ferrite.

- Columnar and cellular dendrites are observed in each layer.
- The dendrites just under the fusion zone are larger compared to the dendrites formed just above the fusion zone.
- Possibly equiaxed dendrites were observed in the last layer at the top, they were not detected in other layers.

5.4.2. Experiment B

In Experiment B equal volume fractions of the ferritic and austenitic stainless steel wires were deposited. Due to mixing the composition of the liquid melt changes affecting the solidifying microstructure. The average Ni content of the mixed metal decreases. In chapter 3.1, it was mentioned that the nickel content for the AISI 430L stainless steel wire was approximately 0.1 wt.% and approximately 12.5 wt.% for the AISI 316L stainless steel wire. According to the pseudo phase diagram an average content of approximately 6 wt. % Ni, results in a primary ferritic microstructure upon solidification. During cooling the ferrite transforms partially to austenite ($L \rightarrow L + F \rightarrow F \rightarrow A + F$), seen in Figure 53. Due to the change in solidification path, the morphology of the microstructure shows nearly no dendrites, instead Widmanstätten austenite and acicular ferrite was found throughout the structure. The structure completely solidifies in ferrite grains, and when the temperate drops below the solidus, the ferrite grain is transformed to Widmanstätten austenite or acicular ferrite.

The presence of phases was confirmed using XRD as was shown in Figure 36. The ferrite content is higher for Experiment B compared to the Experiment A, indicated by the strong ferrite peak in the spectrum. However, to calculate phase fractions from the XRD results, a larger measuring area would have to be considered.

In Figure 54 the weld microstructure for Experiment B is shown. At high temperature, just after solidification the structure is completely ferritic. When the temperature drops below the ferrite solvus (see phase diagram above), austenite first forms at the ferrite grain boundary. Due to the increase in undercooling of the ferrite still present, an increasing number of nuclei will form resulting in breaking down of the transformation front and parallel needles (Widmanstätten morphology) of austenite form within the ferrite. Due to the restriction of long-range diffusion at lower transformation temperature forces the transformation to occur over shorter distances, this produces the acicular structure, indicated in section 2.4.

At the fusion boundary between the last layer and the second-to-last layer, Figure 55, a larger fraction of the top layer is austenitic. The re-heating introduced enough heat to transform some of the formed austenite back to ferrite. As discussed in section 5.3, the cooling is slower for the second cycle. Which allowed the Widmanstätten austenite to form in the second cooling cycle.

5.4.3. Experiment C

In experiment C the chemical composition was gradually changed. Before evaluating the observed microstructure of this wall, the chemical composition and phase analysis of the structure are implemented in the Schaeffler diagram. Using the Schaeffler and the phase diagram from the previous section, the solidification processes may be estimated and then compared in the end of this section.

The XRF results were given in Figure 42. The locations are denoted from (a) to (h), where (a) corresponds to the top of the wall and (h) the bottom of the wall, see Figure 56. In the Schaeffler diagram, Figure 57, indicates the location of the measured areas according to the chemical composition, i.e. the Cr and Ni equivalents. From this plot the ferrite content is estimated.

Table 18: Nickel and Chromium equivalents and the ferrite number based on the XRF results at different locations of the built of experiment C

| | Ni equivalent | Cr equivalent | |
|---------------------------|---------------|---------------|-----------------------------|
| AISI 316 L wire | 13.7705 | 23.9075 | 12 % ferrite |
| AISI 316 substrate | 13.534 | 18.581 | austenite |
| h | 13.0435 | 21.87 | 10 % ferrite |
| g | 11.9115 | 20.758 | 10 % ferrite |
| f | 10.441 | 21.31 | 15 % ferrite |
| e | 7.942 | 20.098 | 39 % ferrite and martensite |
| d | 7.389 | 20.1635 | 50 % ferrite and martensite |
| c | 4.1015 | 19.758 | 85 % ferrite and martensite |
| b | 2.4475 | 17.915 | ferrite and martensite |
| a | 0.534 | 17.2795 | only ferrite |
| AISI 430L wire | 0.7895 | 17.3255 | ferrite |

At location (a) and (b), no austenite is expected. At (c), a very small amount of austenite is expected. The austenite content should gradually increase towards the base plate. This is confirmed by the XRD results for section a-h. Austenite diffraction peaks start to appear in section c, while the ferrite peaks disappear.

Because in the building of the wall of experiment C the amount of the ferritic AISI 430L is gradually increase, the amount of the austenite forming element nickel will decrease. This was also measured. In Figure 43 the measured nickel content using EDS is given as a function of the distance from the top wall (black curve). In addition, the estimated nickel content based on the wires feeding rates is shown. From this graph the actual nickel content gradually changes over the structure due to the remelting of the previous layer.

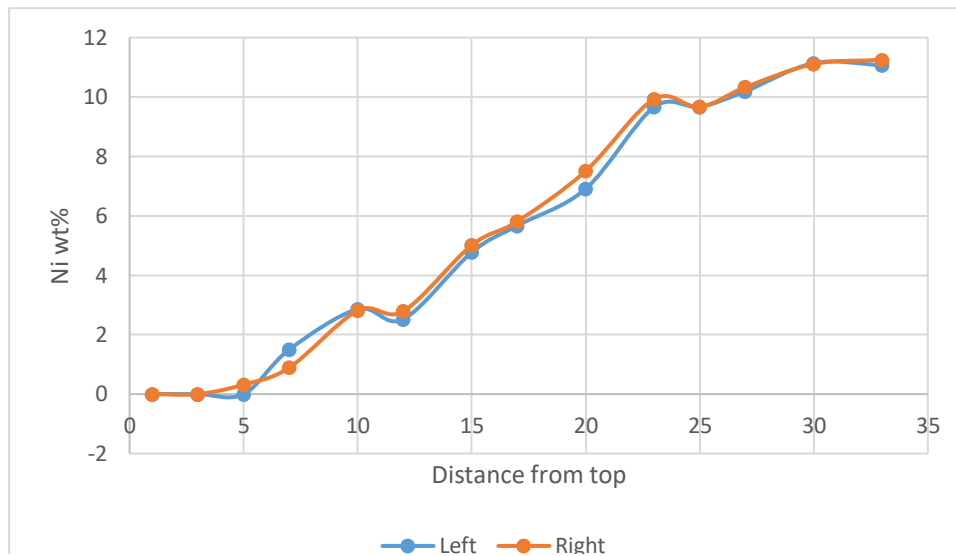


Figure 58: The gradual increase in nickel content and the differences in nickel content between the left side and the right side of the transverse cross section of the wall

In Figure 59 the gradual increase in nickel content and the differences in nickel content between the left side and the right side of the transverse cross section of the wall is depicted. From this graph it can be concluded that there no significant difference in nickel content at either side, indicating good mixing of the wires during welding took place.

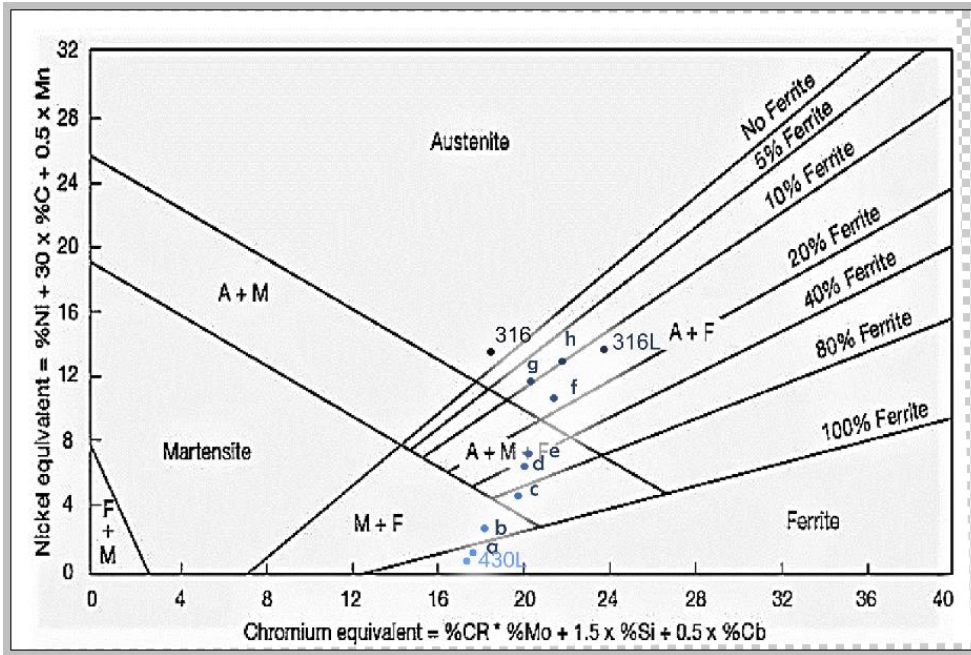


Figure 60: Schaeffler diagram indicating the location of several locations of experiment C based on XRF measurements I would make the added points in red, may be add an arrow indicating the direction from bottom to top

Microstructure

The microstructure observed in the graded structure is depicted in Figure 44. In the first layer (Figure 44 (a)), the microstructure is cellular/columnar dendritic. The chemical composition in the first layers is the same as in experiment A. As it was discussed in section 5.4.1 austenite formed as a dendritic structure during solidification. Ferrite was precipitated in the region between the austenite cells. In layers in which AISI430L is added, phase transformation from austenite to ferrite after solidification take place. For a larger fraction AISI 430L, the chemical composition is such, that ferrite becomes the primary phase at solidification (Figure 44 (b)) and is transformed to Widmanstätten austenite as discussed in section 5.4.2. In Figure 44 (d) only a small fraction of ferrite is transformed to austenite. The structure with an increased ratio in AISI 430L content, showed fully ferritic grains.

The microstructure changes per layer, can be linked to the phase diagram discussed and depicted in section 5.4.1. However, the phase diagram was calculated for AISI 316L stainless steel and shown in nickel content. However, both grades have differences in *i.e.* Molybdenum content, the phase diagram can only be taken as an indication.

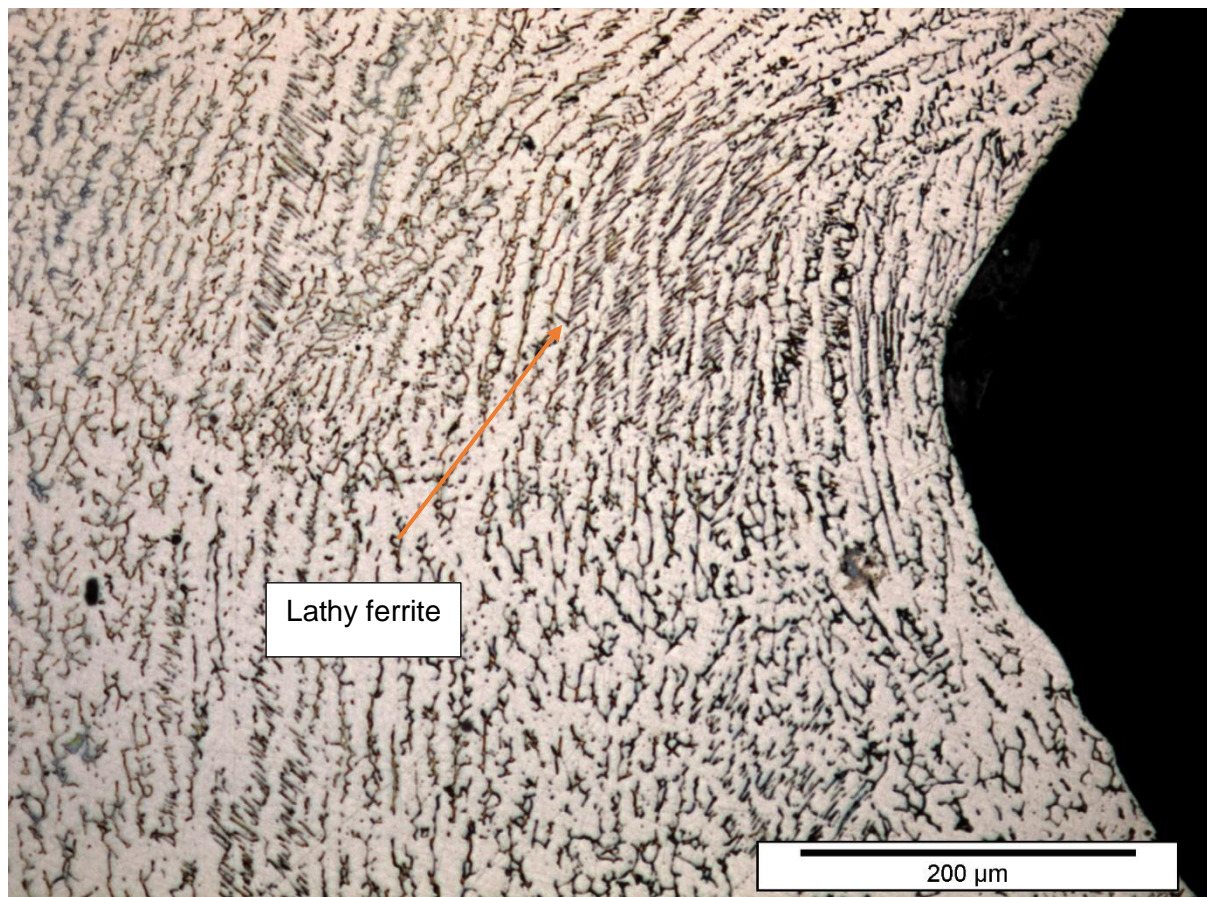


Figure 61: dendritic austenite structure and lathy structure

5.5.Reducing the interpass time – COMSOL simulation

The building time for the produced wall with a height of approximately 3 centimetre high was multiple hours. For industrial purposes, the total building time of the additive manufactured structure should be reduced. This can be achieved by shortening the interpass time. However, by reducing the interpass time, the interpass temperature will increase. During the building process with a fixed interpass time, the interpass temperature will gradually increase until an equilibrium in heat input and heat loss is achieved. Figure 63, depicts this effect in the temperature cycles for the welding of 7 layers, for a fixed location in the COMSOL thermal model. After the first cycle, the minimum temperature is around 180°C, while after the second cycle, the temperature is already raised to 230°C. From the 6th cycle onwards, the temperature stays around 500°C. Even though the maximum temperature slowly decreases each cycle (as the distance from the fusion line of the selected location increases), it can be extrapolated that the whole structure will eventually reach a steady state around 600-700°C.

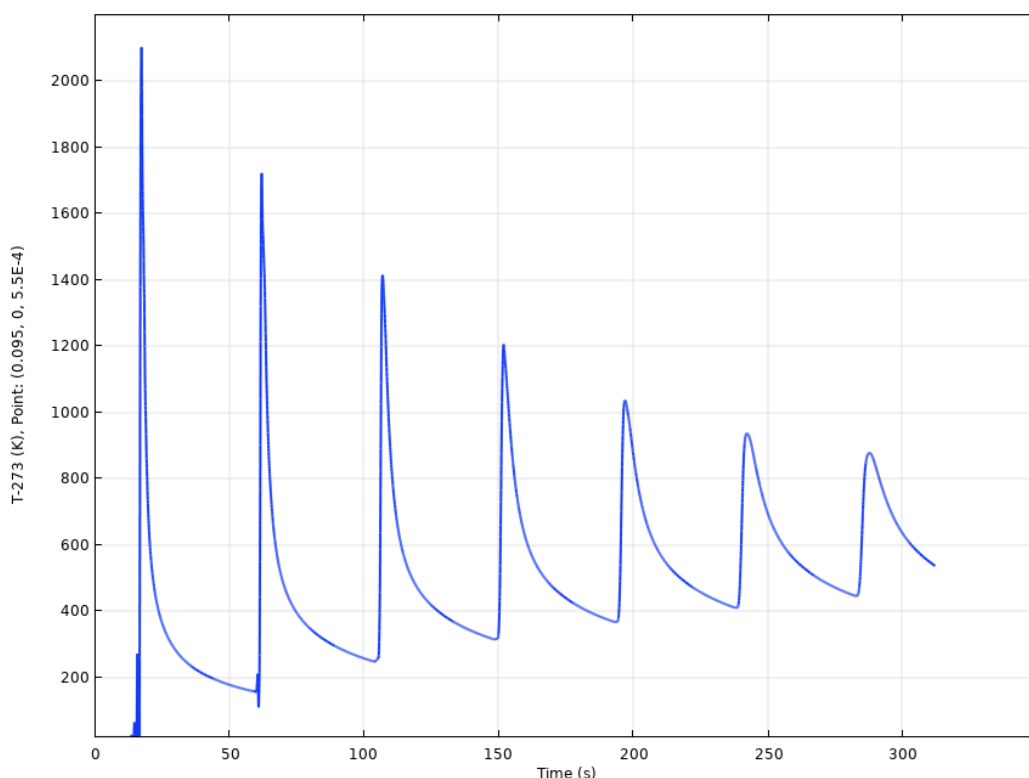


Figure 62: heat cycles fixed point COMSOL temperature model

As seen in the Figure 52, in this temperature range, sigma phase becomes stable. As mentioned in the section 2.7.5, sigma phase is a brittle intermetallic phase, which presence is detrimental for the mechanical properties of the material. The equilibrium phase diagram does not allow to evaluate the kinetics of the formation of this phase. It is mentioned in the literature that the sigma phase is encountered during welding of thick section steel plates where preheating is required [11]. Furthermore, the sigma phase forms more readily from a ferritic microstructure[11].

In this study, it was therefore investigated under what circumstances the sigma phase forms in the 3D printed structure. Due to the multiple depositions and thus heat cycles, the temperature remains relatively high, thereby increasing the time that diffusion may take place required to form the sigma phase. The formation of this phase is discussed in the following section.

5.6. Formation of brittle phases in the as-welded material

In this section it is discussed under which circumstances sigma phase forms, and whether the formation of sigma phase needs to be taken into consideration during the building of future Functionally Graded Materials like AISI316L&AISI430L produce in this project. In first instance the microstructure of the as-deposited material is investigated by XRD whether it contains the sigma phase. It appears that no sigma phase was found. Therefore, as mentioned (somewhere) post deposition heat treatments were conducted to explore the effect of post weld heat treatments or service temperature of a construct.

Table 17 provides an overview of XRD phase identification results for as-welded and heat-treated samples. Figure 45 for the XRD results of Experiments A, as-welded and heat treated.

5.6.1. Microstructure

In the microstructure of Experiment A, the original interdendritic ferrite in the austenite matrix changed to spherical particles when heat treated for 90 hours at 850 °C. Due to the heat input, the and long holding times, diffusion could take place. As the sigma phase is stable under equilibrium circumstances, this phase formed. During welding, cooling is too fast to form the sigma phase. And only long holding times in the critical regime will lead to the formation of sigma phase. The repetitive heating during welding, in the critical regime may lead to the formation of the phase as well. This may be due to short interpass time or building larger structures, with multiple beads.

In the graded structure, sigma phase was found mainly in the first 6 layer (fully AISI316L) and decreased with increasing the AISI430L stainless steel fraction (Figure 46).

5.7. Summary: Heat treatments

- Sigma phase was not detected in any of the welded structures
- Sigma phase was confirmed to form when held at 850 °C for 90 hours (in all walls)
- Sigma phase did not form at 600 °C after 90 hours in the Experiment A sample

6. Conclusion

In this study, a functionally graded structure was manufactured using Gas Tungsten Arc Welding equipped with a double wire feeder. By gradually changing the wire feed rate of each of the wires, a compositionally gradually graded structure was successfully fabricated using AISI 316L and AISI 430L stainless steel on an AISI 316 stainless steel substrate. The evolution of the microstructure was studied. From the results the following conclusion can be drawn.

1. A graded structure from AISI 316L to AISI 430L was successfully fabricated in which no defects or pores were found. Good mixing in the weld pool was achieved as no differences in chemical composition between left and right side of the construct was observed.
2. A smooth chemical composition gradient of nickel content and molybdenum content was achieved in the building direction.
3. A dendritic solidification microstructure is achieved.
4. No sigma phase or other brittle intermetallic phases were detected using X-Ray Diffraction and Optical Microscopy.
5. When the graded structure is heat treated for 90 hours at 600°C, no sigma nor other brittle phases are detected.
6. When AISI 316L-AISI 430L (in equal portion) stainless steel is heat treated for 5 hours at 750°C, no sigma nor other brittle phases are detected.
7. When the graded structure is heat treated for 90 hours at 850 °C, sigma phase is detected.

7. Recommendations

1. The deposited structure was a single bead structure with long cooling time (several minutes). The heat model shows that decreasing interpass time significantly influences the interpass temperature. It is worth investigating how interpass temperature changes with changing interpass time. In addition, it is worth studying how the cooling rate is influenced when the structure is not a single pass weld but a multi-pass weld with long and short interpass time.
2. This study focussed on phase formation and microstructure for the graded structure. However, microstructures are usually investigated in relation to the mechanical behaviour of the material. The mechanical behaviour of the graded structure, its hardness, strength and ductility may be worth investigating. Other properties such as ferromagnetism may be investigated.
3. Sigma phase may not only influence mechanical behaviour of the material (brittle fracture) but influence the corrosion behaviour of the build. The heat treated graded structure showed sigma phase especially in the first layers of the sample. However, for the later deposited layers the sigma phase was less often detected in the microstructure. Therefore, the sample after heat treatment was slowly graded from high in sigma to low in sigma to no sigma at all. In the last layers no sigma was detected. This may be an interesting direction for using this graded structure to be protected from corrosion behaviour.

Bibliography

- [1] D. C. Hofmann *et al.*, “Developing gradient metal alloys through radial deposition additive manufacturing,” *Sci. Rep.*, vol. 4, 2014.
- [2] C. H. Zhang, H. Zhang, C. L. Wu, S. Zhang, Z. L. Sun, and S. Y. Dong, “Multi-layer functional graded stainless steel fabricated by laser melting deposition,” *Vacuum*, vol. 141, pp. 181–187, 2017.
- [3] T. DebRoy *et al.*, “Additive manufacturing of metallic components – Process, structure and properties,” *Prog. Mater. Sci.*, vol. 92, pp. 112–224, 2017.
- [4] C. Shen, Z. Pan, Y. Ma, D. Cuiuri, and H. Li, “Fabrication of iron-rich Fe-Al intermetallics using the wire-arc additive manufacturing process,” *Addit. Manuf.*, vol. 7, pp. 20–26, 2015.
- [5] B. A. Szost *et al.*, “A comparative study of additive manufacturing techniques: Residual stress and microstructural analysis of CLAD and WAAM printed Ti-6Al-4V components,” *Mater. Des.*, vol. 89, pp. 559–567, 2016.
- [6] S. Kou, *Welding Metallurgy Second Edition*. Hoboken, New Jersey: John Wiley & Sons, 2003.
- [7] F. Yan, W. Xiong, and E. J. Faierson, “Grain structure control of additively manufactured metallic materials,” *Materials (Basel)*, vol. 10, no. 11, p. 1260, 2017.
- [8] L. D. Bobbio *et al.*, “Characterization of a functionally graded material of Ti-6Al-4V to 304L stainless steel with an intermediate V section,” *J. Alloys Compd.*, vol. 742, pp. 1031–1036, 2018.
- [9] A. A. Allahyari and H. Farhangi, “Investigation of aging heat treatment on microstructure and mechanical ... Paper Information Investigation of aging heat treatment on microstructure and mechanical properties of 316L austenitic stainless steel weld metal Login Your Cart Investigation of a,” vol. 51, no. December, pp. 14–15, 2005.
- [10] S. I. Cristini, B. Sacchi, E. Guerrini, S. Trasatti, and S. P. Trasatti, “Detection of sigma phase in 22% Cr duplex stainless steel by electrochemical methods,” *Russ. J. Electrochem.*, vol. 46, no. 10, pp. 1094–1100, 2010.
- [11] C.-C. Hsieh and W. Wu, “Overview of Intermetallic Sigma () Phase Precipitation in Stainless Steels,” *ISRN Metall.*, 2012.
- [12] J. C. Lippold and D. J. Kotecki, *Welding Metallurgy and Weldability of Stainless Steels*, no. 1. Wiley, 2005.
- [13] ASM Authors, “Metals Handbook,” *Met. Handb.*, p. 2571, 1998.
- [14] N. Suutala, T. Takalo, and T. Moiso, “The relationship between solidification and microstructure in austenitic and austenitic-ferritic stainless steel welds,” *Metall. Trans. A*, vol. 10, no. 4, pp. 512–514, 1979.
- [15] N. Suutala and T. Takalo, “Ferritic-Austenitic Solidification Mode in Austenitic Stainless Steel Welds,” *Metall. Trans. A*, vol. I, no. May, pp. 717–725, 1980.
- [16] W. D. Callister, “Materials science and engineering: An introduction (2nd edition),” *Mater. Des.*, 1991.
- [17] D. L. Olson, “Prediction of Austenitic Weld Metal Microstructure and Properties,” *AWS 65th Annu. Meet.*, pp. 280–295, 1984.
- [18] D. J. Kotecki and T. A. Siewert, “WRC-1992 Constitution Diagram for Stainless Steel Weld Metals: A Modification of the WRC-1988 Diagram Refined constitution diagram offers more accurate FN prediction for Cu-containing stainless steels and dissimilar metal joints,” pp. 171–178, 1992.
- [19] K. D. Ramkumar *et al.*, “Comparative studies on the weldability , microstructure and tensile properties of autogeneous TIG welded AISI 430 ferritic stainless steel with and without flux,” *J. Manuf. Process.*, vol. 20, pp. 54–69, 2015.
- [20] B. Weiss, R. Stickler, B. Weiss, and W. Re-, “Phase Instabilities During High

- Temperature Exposure of 316 Austenitic Stainless Steel,” vol. 3, no. April, 1972.
- [21] L. Wang, J. Xue, and Q. Wang, “Correlation between arc mode, microstructure, and mechanical properties during wire arc additive manufacturing of 316L stainless steel,” *Mater. Sci. Eng. A*, vol. 751, pp. 183–190, 2019.
- [22] E. T. Mahamood, Rasheedat Madupe; Akinlabi, *Functionally Graded Materials*. 2017.
- [23] A. Nazari and A. A. Milani, “Ductile to brittle transition temperature of functionally graded steels with crack arrester configuration,” *Mater. Sci. Eng. A*, vol. 528, no. 10–11, pp. 3854–3859, 2011.
- [24] Y. M. Shabana, H. A. Bruck, M. L. Pines, and J. G. Kruff, “Modeling the evolution of stress due to differential shrinkage in powder-processed functionally graded metal-ceramic composites during pressureless sintering,” *Int. J. Solids Struct.*, 2006.
- [25] S. Put, J. Vleugels, G. Anné, and O. Van Der Biest, “Functionally graded ceramic and ceramic-metal composites shaped by electrophoretic deposition,” *Colloids Surfaces A Physicochem. Eng. Asp.*, 2003.
- [26] T. Abe and H. Sasahara, “Dissimilar metal deposition with a stainless steel and nickel-based alloy using wire and arc-based additive manufacturing,” *Precis. Eng.*, 2016.
- [27] C. Shen, Z. Pan, D. Cuiuri, J. Roberts, and H. Li, “Fabrication of Fe-FeAl Functionally Graded Material Using the Wire-Arc Additive Manufacturing Process,” *Metall. Mater. Trans. B Process Metall. Mater. Process. Sci.*, vol. 47, no. 1, pp. 763–772, 2016.
- [28] S. Nam, H. Cho, C. Kim, and Y.-M. Kim, “Effect of Process Parameters on Deposition Properties of Functionally Graded STS 316/Fe Manufactured by Laser Direct Metal Deposition,” *Metals (Basel)*, vol. 8, no. 8, p. 607, 2018.
- [29] W. Li *et al.*, “Fabrication and characterization of a functionally graded material from Ti-6Al-4V to SS316 by laser metal deposition,” *Addit. Manuf.*, vol. 14, pp. 95–104, 2017.
- [30] J. S. Zuback, T. A. Palmer, and T. DebRoy, “Additive manufacturing of functionally graded transition joints between ferritic and austenitic alloys,” *J. Alloys Compd.*, vol. 770, pp. 995–1003, 2018.
- [31] O. V. Eliseeva *et al.*, “Functionally Graded Materials through robotics-inspired path planning,” *Mater. Des.*, vol. 182, p. 107975, 2019.
- [32] E. Van Der Aa, “Finite element modelling of temperature profiles,” 2002.
- [33] J. Goldak, A. Chakravarti, and M. Bibby, “A new finite element model for welding heat sources,” *Metall. Trans. B*, vol. 15, no. 2, pp. 299–305, 1984.
- [34] B. Wu *et al.*, “A review of the wire arc additive manufacturing of metals: properties, defects and quality improvement,” *J. Manuf. Process.*, vol. 35, no. February, pp. 127–139, 2018.
- [35] G. Agarwal, “Study of solidification cracking during laser welding in advanced high strength steels A combined experimental and numerical approach,” TU Delft, 2019.
- [36] D. A. Porter and K. E. Easterling, *Phase Transformations in Metals and Alloys*, Third Edit. Boca Raton: CRC Press Taylor & Francis Group, 2009.
- [37] J. H. Lee and Y. S. Kim, “Intergranular Corrosion of 316L Stainless Steel by Aging and UNSM (Ultrasonic Nano-crystal Surface Modification) treatment,” *Corros. Sci. Technol.*, vol. 14, no. 6, pp. 313–324, 2015.
- [38] W. Liu, X. G. Lu, P. Boulet, and M. C. Record, “Influencing factors of atomic order in the binary sigma phase,” *Intermetallics*, 2018.
- [39] O. A. Cortez, F. J. Moura, E. de Albuquerque Brocchi, R. N. C. de Siqueira, and R. F. M. de Souza, “Fe-Ni Alloy Synthesis Based on Nitrates Thermal Decomposition Followed by H₂ Reduction,” *Metall. Mater. Trans. B Process Metall. Mater. Process. Sci.*, vol. 45, no. 6, pp. 2033–2039, 2014.
- [40] B. Ennis, “A review of the effects of chemical and phase segregation on the mechanical behaviour of multi-phase steels,” *arXiv*, no. 1604.06485, Apr. 2016.
- [41] C. B. Dallam and B. K. Damkroger, “Characterization of Welds,” *Welding, Brazing Solder.*, vol. 6, pp. 97–106, 1993.
- [42] "COMSOL Multiphysics® v. 5.3a ", ed. Stockholm, Sweden: COMSOL AB.